THESIS FOR THE DEGREE OF LICENTIATE OF ENGINEERING

Synthesis and Characterisation of Phase Change Materials for Molecular Solar Thermal Systems

Monika Shamsabadi

CHALMERS

Department of Chemistry and Chemical Engineering

Division of Applied Chemistry

CHALMERS UNIVERSITY OF TECHNOLOGY

Göteborg, Sweden, 2024

Synthesis and Characterisation of Phase Change Materials for Molecular Solar Thermal Systems

Monika Shamsabadi

Department of Chemistry and Chemical Engineering
Division of Applied Chemistry
Chalmers University of Technology
SE-41296 Göteborg

Phone: +46 (0)31 772 1000

Cover:
An illustration of a molecular solar thermal systems that can coharvest solar energy and ambient heat and releases high-T heat using phase change molecules.

Synthesis and Characterisation of Phase Change Materials for Molecular Solar Thermal Systems

ABSTRACT

Demand for energy has steadily increased over the last decade and several technologies have been developed to combat the resulting global impact. Solar power systems are an attractive option for a cleaner and more sustainable source of energy owing to the magnitude of energy the sun provides as well as its availability and consistency. However, modern versions of these technologies still face challenges in effectively storing energy, particularly concerning storage capacity, lifespan, and disposal of the devices. The Molecular Solar Thermal Systems (MOST) are a class of organic materials which can undergo a reversible photochemical reaction allowing for storage of solar energy as chemical energy which ultimately can be released as heat. One such system is based on the norbornadiene (NBD) derivatives that can isomerise to form the metastable quadricyclane (QC). The QC to NBD conversion can be initiated with the use of a catalyst, light, or heat to release thermal energy. However, the best performing NBDs struggle to be integrated into devices due to properties such as poor solubility and short storage life. Phase change materials (PCMs) can also store energy *via* a phase transition from solid-to-liquid from latent heat, although the energy density stored is limited. Thus, a material that combines the function of MOST and PCM was synthesised to tackle the drawbacks of the single function materials.

In this thesis, a series of NBDs engineered with varying substituents in order to explore improvements to solubility of the systems. These compounds were synthesised *via* Diels-Alder reactions in a comparative study of thermal and microwave-assisted synthesis. Furthermore, evaluation of different purification methods (distillation, HPLC, flash chromatography) of the products were explored to determine which method yields pure products for photocharacterisation, solubility, and stability studies. It was revealed that the chosen substituents had a positive effect on the solubility of the molecules, though did not improve on the degradation observed in similar derivatives.

Another class of MOST compounds were studied to improve the phase change transition properties for future MOST-PCM applications. By varying the alkyl chain length on an azobenzene moiety, the effects on the phase-transition temperatures and energy storage were evaluated. This led to the observation that the azobenzene with six carbons in the alkoxy chain are the best performing material for MOST-PCM applications with the highest energy storage density, achieving the target suggested for solar thermal storage systems.

Keywords: *Norbornadiene, azobenzene, molecular solar thermal systems, photoswitch, phase change materials.*

NOMENCLATURE

A_{max}	Max Absorption
A_{onset}	Absorption Onset
Azo	Azobenzene
DFT	Density functional theory
DMF	*N,N*-dimethylformamide
E_a	Activation energy
ΔH_{Cryst}	Crystallisation enthalpy
ΔH_{IE}	Ionisation Energy
ΔH_{Tot}	Energy Storage Capacity
LED	Light-emitting diode
LUMO	Lowest unoccupied molecular orbital
MeCN	Acetonitrile
MOST	Molecular Solar Thermal System
MR	Microwave-assisted Synthesis
M_w	Molecular weight
NBD	Norbornadiene
NMR	Nuclear magnetic resonance
oDCB	*o*-dichlorobenzene
PCM	Phase Change Material
Py	Pyrene
QC	Quadricyclane
RT	Room temperature
$t_{1/2}$	half-life
T_c	Crystallisation temperature
T_g	Glass transition temperature
T_m	Melting temperature
TR	Thermal Synthesis
UV-vis	Ultraviolet visible
ε_{max}	Extinction coefficient
Φ	Quantum Yield

PUBLICATIONS

This thesis consists of an extended summary of the following appended papers:

Paper I   **Structure-property relationship in pyrene functionalised norbornadiene-quadricyclane fluorescent photoswitches: characterisation of their fluorescence properties and application in imaging of amyloid beta plaques**

Shima Ghasemi, Monika Shamsabadi, Axel Olesund, Andreas Erbs Hillers-Bendtsen, Francisco Najera, Fredrik Edhborg, Adil S. Aslam, Wera Larsson, Zhihang Wang, Francoise M. Amombo Noa, Rebecca Jane Salthouse, Lars Öhrström, Helen Hölzel, E. Perez-Inestrosa, Kurt V. Mikkelsen, Jörg Hanrieder, Bo Albinsson, Ambra Dreos and Kasper Moth-Poulsen

Chem. Eur. J, **2024,** Accepted

Paper II   **Synthesis and Structure-Property Relationship of Multiple Site Functionalised Norbornadiene-Quadricyclane as Molecular Solar Thermal Materials for Energy Storage**

Monika Shamsabadi, Joost Kimpel, Christian Müller and Kasper Moth-Poulsen

Manuscript in preparation, **2024**

Paper III   **Structure Properties Relationship of p-Alkoxy-Azobenzenes as Molecular Solar Thermal Phase Change Material for Energy Storage Systems**

Conrad Averdunk, Monika Shamsabadi, Kasper Moth-Poulsen and Hermann A. Wegner

Manuscript in preparation, **2024**

The author has published the following papers which are not included in the thesis:

Paper IV   **Chasing the rainbow: Exploiting photosensitizers to drive photoisomerization reactions**

Zhihang Wang, Lorette Fernandez, Adil S Aslam, Monika Shamsabadi, Lidiya M Muhammad and Kasper Moth-Poulsen

Responsive Materials, **2023**

CONTRIBUTION REPORT

Paper I   Second author. Carried out photocharacterisation: quantum yield, development of automated cycling experiment and half-life experiment and calculations. Irradiation and NMR studies and synthesis of precursors.

Paper II   Main author. Synthesised the materials studied in the paper. Performed solubility and photocharacterisation of the compounds: UV-vis and kinetics.

Paper III   Second author. Carried out DSC investigations for the thermal and crystallisation properties and determination of energy densities. Aided in the conceptualisation of the series.

TABLE OF CONTENT

Chapter 1

INTRODUCTION

In response to the increasing demand for sustainable power sources, the development of renewable energy sources has increased in priority. While hydroelectric power and wind turbines offer alternative options, their implementation raises concerns about their effects on wildlife and ecosystems. Another significant challenge with renewable energy sources is that they face geographically limitations. However, solar energy, despite its constraints, remains the most abundant and promising option as it surpasses the world's annual energy consumption in just one hour of sunlight[1].

The past decade has witnessed significant progress in solar energy harnessing, notably through the widespread adoption of solar photovoltaics, reaching a capacity of around 1,177 gigawatts by 2022[2]. However, the critical challenge lies in effective energy storage. This has led to a surge in innovative solutions, including Molecular Solar Thermal Energy Storage (MOST) systems[3].

MOST employs the photoinduced isomerisation of chemical bonds in small molecules to capture and store solar energy, allowing for the release of heat on demand[4]. Recent research has explored enhancing energy storage density by combining photoisomerisation with a solid-to-liquid phase transition[5]. This novel approach enables the storage of both photon energy through photoisomerisation and ambient temperature energy through a simultaneous melting process. This licentiate thesis delves into the synthesis and characterisation of molecular solar thermal energy storage systems with potential for solid-to-liquid phase transitions, aiming to contribute to the understanding of these systems and their potential applications.

Chapter 2

BACKGROUND

2.1 Molecular Solar Thermal Energy Storage

A Molecular Solar Thermal Energy Storage System (MOST) involves a compound capable of undergoing sunlight-induced conversion into a photoisomer, wherein the absorbed energy is stored as chemical energy. Upon triggering a back reaction with heat or a catalyst, the stored energy is released as heat energy and the photoisomer is reverted to the parent compound[3, 6]. This controllable closed system serves as an energy storage without emissions. For a MOST system to be considered efficient, it must adhere to several critical criteria (Figure 1): i) the parent compound should absorb sunlight within the solar spectrum, ensuring the sun can drive the reaction; ii) the photoisomer should avoid absorbing in the same range as the parent compound to prevent overlap in absorption spectra and restricting full conversion; iii) a significant enthalpy difference ($\Delta H_{storage}$) between the parent compound and the photoisomer is crucial for storing a substantial amount of energy in the system; iv) a high energy barrier for the uncatalysed back conversion (E_a) is necessary for long storage times; v) fast photoisomerisation with a high quantum yield so that it is effective; and vi) a robust system capable of enduring numerous cycles is important has a long shelf-life. In addition to these fundamental requirements, an ideal compound for MOST should be synthesised using non-toxic and abundant starting materials and overall possess a low molecular weight to achieve a high energy density[3, 4].
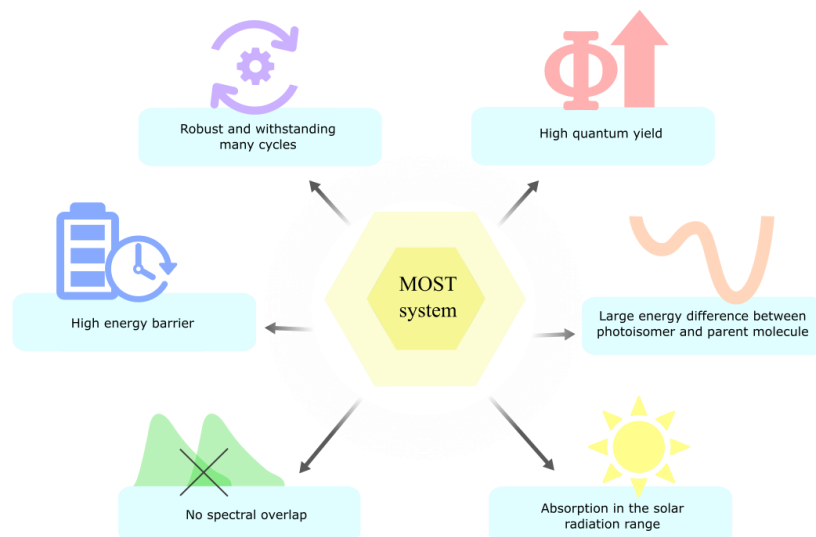
Figure 1. Schematic showing the criteria of a Molecular Solar Thermal System.

Numerous molecular systems (Figure 2) have been evaluated as MOST candidates: stilbene (a) and azobenzene (b) undergo *trans – cis* isomerisation upon irradiation[7, 8], while anthracene (c) forms a dimer[9], and the fulvalene diruthenium rearranges (d)[10]. Dihydroazulene converts to the photoisomer vinylheptafulvene (e), and norbornadiene converts to a quadricyclane (f)[11]. These systems exhibit different properties, each presenting unique advantages and disadvantages as MOST candidates. However, this focus is confined to the norbornadiene – quadricyclane as well as the azobenzene system.
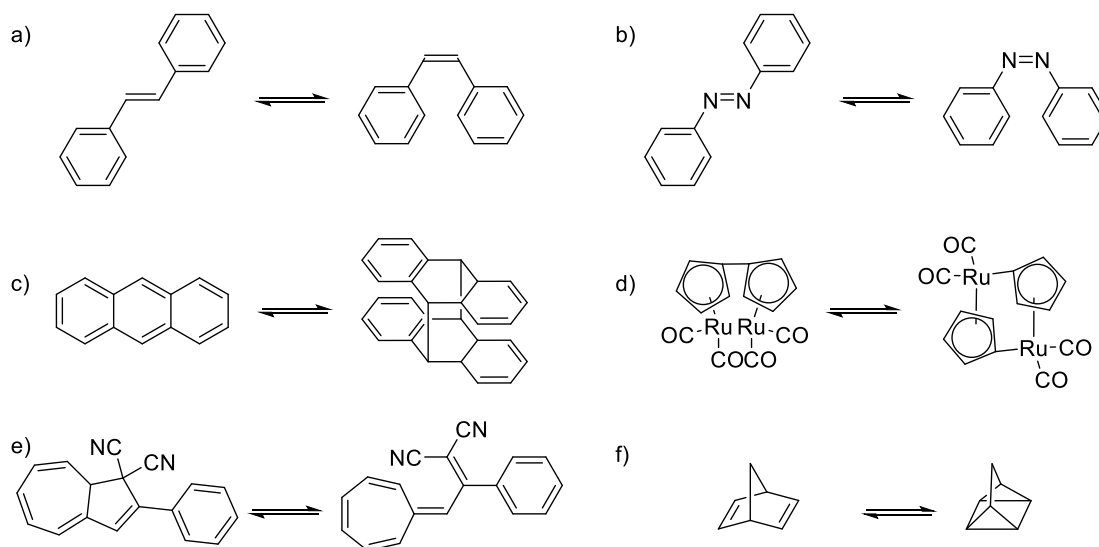

Figure 2. Examples of photoswitches commonly utilised across various applications and their corresponding photoisomerisation processes include a) stilbene; b) azobenzene; c)

4

anthracene; d) tetracarbonyl-fulvalene-diruthenium; e) dihydroazulene; f) norbornadiene to quadricyclane.

2.1.1 The Norbornadiene – Quadricyclane System

Norbornadiene (NBD), firstly reported in the 1950s, undergoes a [2+2] cycloaddition upon UV exposure to form the highly strained, metastable photoisomer quadricyclane (QC)[12]. NBDs were first synthesised for the utility in organic chemistry, particularly in the field of cycloaddition reactions and were used to facilitate the development of new materials and pharmaceuticals[13, 14]. The best performing variant of this system has an excellent energy storage capability, with a density of about 90 kJ/mol or 980 kJ/kg, with a half-life of 14 hours at 140°C[15]. For the optimum photoconversion and solar energy conversion efficiency, an absorption onset at 656 nm with 100% quantum yield is desired[16]. However, NBD's solar absorption onset below 300 nm hinders the photoconversion as it does not have a good overlap with the solar spectrum and would give a low quantum yield (~5%)[17].

Introducing substituents to the NBD/QC system allows for property adjustments, aiming for a solar spectrum match through absorption red shifting. Employing push-pull systems with electron-donating and electron-accepting groups around the double bonds proves effective, as demonstrated by research on donor/acceptor norbornadienes by Yoshida and Chernoivanov as well as examples within the Moth-Poulsen group[3, 17, 18]. Donor/acceptor norbornadienes emphasise the loss of conjugation between donor and acceptor groups upon photoconversion, resulting in distinct absorption profiles of the two isomers.

Despite these advantages, a noticeable trend emerges as the absorption of norbornadiene red shifts, the half-life of quadricyclane decreases, affecting the quantum yield. The Moth-Poulsen group reported this trend in diaryl-substituted donor/acceptor norbornadienes[19]. Addressing this challenge requires careful parameter optimisation, considering the intricate balance between various factors for an efficient MOST system. Exploring diverse norbornadiene variants, including functionalising across the entire NBD is essential to deepen the understanding of the correlation between substitution patterns and MOST properties.

2.1.2 The Azobenzene *trans/cis* System

Azobenzene, first synthesised nearly 200 years ago by Mitscherlich, has played a crucial role in the evolution of photochromic molecules[20]. Initially discovered in the pursuit of new synthetic dyes, azobenzene compounds were investigated for their application in the dye industry[21]. In 1937, Hartley discovered the photoisomerisation of azobenzenes allowing them to be utilised in a multitude of applications[22]. Azobenzenes have undergone continuous development, finding use in biomacromolecules, hybrid materials, polymers, inorganic materials, and metal–organic frameworks, showcasing their versatility in light-responsive applications[23-27]. Known for easy accessibility and high chemical stability, azobenzenes can switch from its thermodynamically stable *trans*-isomers to the metastable energetically excited *cis*-isomer during photon absorption[28, 29]. However, a notable trend has emerged as the absorption band of azobenzenes red shifts: the thermal stability of the *cis*-isomer decreases, impacting the overall efficiency of the MOST system. While facing challenges related to energy density, recent research has focused on enhancing storage density by increasing the energy difference between the respective photoisomers[30].

2.2 Phase Change Materials

Phase change materials (PCMs) are substances capable of transitioning between solid and liquid states while absorbing or releasing latent heat[31]. This property makes them particularly valuable when incorporated into MOST system as PCMs complement the established storage mechanism by providing an additional route that enhances the overall energy density. This dual-storage mechanism involves utilising photon energy for photoisomerisation within the MOST system and simultaneously capturing ambient temperature energy through the PCM's phase transition. When irradiation induces the photoisomerisation of the parent molecule to the photoisomer, and if the photoisomer possesses a lower melting point than the parent isomer, ambient temperature can result in melting. Subsequently, as in the standard MOST systems, an external influence induces back isomerisation, releasing the combine stored energy as heat.
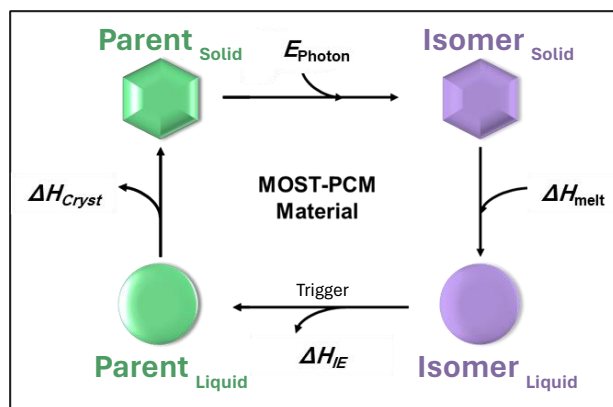
Figure 3. Schematic illustration of MOST-PCM material and the energy interactions. The parent molecule is irradiated into the photoisomer with a melting point temperature at room temperature resulting in a phase change. Then the photoisomer can be converted back to the parent releasing the stored energy as well as the energy released as the parent molecule crystallises.

Recent literature has explored the combination of MOST and PCMs[5, 32] (Figure 3). Particularly, phase change azobenzene derivatives have emerged as promising candidates for high-density energy storage, leveraging the combined capture of ambient heat and photothermal energy. The tuneable isomerisation enables precise control of heat release triggered by light and/or temperature. In comparison to the planar *trans*-isomer, the distorted structure of the *cis*-isomer promotes weaker intermolecular interactions and a lower phase change temperature, facilitating solid-liquid phase transitions. Notable examples include azobenzenes substituted with alkoxy or carboxy alkyl chains[33-35]. These investigations delve into the effects of position, substitution, and chain length on the melting points of *trans-* and *cis-* isomers, revealing structural considerations essential for optimising MOST-PCM systems[31, 36]. Optimisation of molecular structure and intermolecular interactions, such as π-stacking among aryl groups and van der Waals forces between alkyl substituents, are important for achieving enhanced energy storage densities[37]. These interactions influence the crystallisation, isomerisation, and the overall energy density of the resultant storage system, wherein stronger intermolecular interactions promote stacking and crystallisation while inhibiting isomerisation.

Chapter 3

AIM OF THE WORK

This investigation seeks to improve upon the current generation of MOST systems by introducing functional modifications to the norbornadiene-quadricyclane system, creating a donor/acceptor system across the entire molecule whilst introducing a solid-to-liquid phase change. This is with the aim of enhancing characteristics such as energy density, quadricyclane stability and solubility. The approach unfolds in two main stages: firstly, synthesising novel norbornadienes (NBDs) with selected substituents to introduce steric bulk and enhance solubility. Secondly, a detailed characterisation of the photophysical properties of the newly synthesised NBDs as well as azobenzene systems, including an exploration of any phase change behaviour, in order to discover materials that would function as successful MOST-PCM systems.

Chapter 4

EXPERIMENTAL METHODS

4.1 Synthesis of Norbornadienes

One approach to synthesising norbornadienes involves the Diels-Alder reaction, a pericyclic reaction which benefits from high atom economy[38]. This reaction creates cyclohexene derivatives from the reaction between conjugated dienes, and (un)substituted alkenes or alkynes[39]. To make unsubstituted norbornadiene, acetylene and cyclopentadiene are reacted in Diels-Alder fashion. Starting materials with varying substituents can be used to add desired functionality at various positions in the norbornadiene. One way to produce donor/acceptor norbornadienes is by reacting acetylenes with both an electron-accepting (R_1) and an electron-donating (R_2) group, using cyclopentadiene (Figure 4).
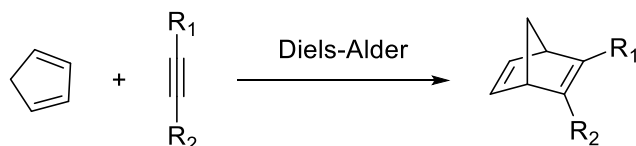
Figure 4. Synthesis of donor/acceptor norbornadienes *via* Diels-Alder reaction. R_1 and R_2 are acceptor and donor groups.

Alternatively, norbornadienes (NBDs) can be made using cross-coupling reactions with halogenated norbornadienes[40]. A norbornadiene featuring two different halogens, denoted as X and Y, is used as the substrate. In the primary cross-coupling reaction, the introduction of either an electron-donating or electron-accepting group occurs. Subsequently, in the secondary cross-coupling reaction, the substitution of the remaining group takes place. (Figure 5). This method provides a practical way to tailor the structure of NBDs for various applications.
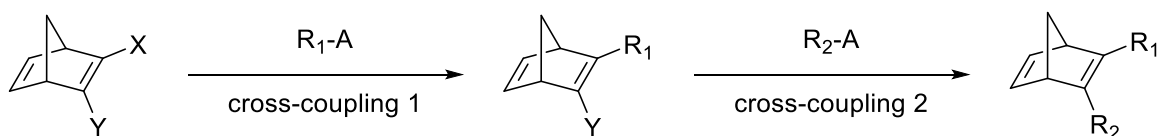
Figure 5. Synthesis of donor/acceptor norbornadienes *via* cross-coupling reaction using halogenated norbornadienes. R_1 and R_2 are acceptor and donor groups, X and Y are different halogens, and A is the second coupling partner.

Cross-coupling reactions connect two hydrocarbon fragments using a palladium catalyst through a general mechanism involving oxidative addition, transmetalation, and reductive elimination steps (Figure 6). One of the hydrocarbons is typically an aryl halide whilst the second hydrocarbon fragment's nature varies widely across different coupling reactions. For instance, in the Heck reaction, it is an alkene; in the Sonogashira coupling, an alkyne; and in the Suzuki coupling, a boronic acid[41-44]. Other well-known coupling reactions, such as the Stille coupling and the Negishi coupling, employ organotin and organozinc compounds as the coupling partner[44, 45]. Due to the structural diversity of coupling partners, cross-coupling reactions are highly valuable in organic synthesis, enabling the synthesis of diverse organic compounds.
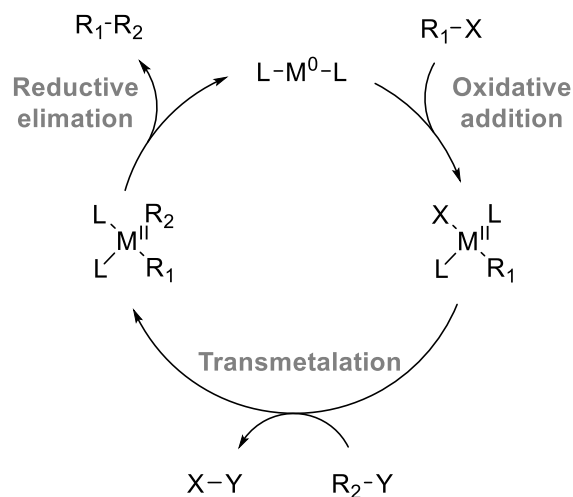
Figure 6. General catalytic mechanism for cross-coupling reactions. X is a leaving group and Y is an organometallic group.

4.2 Photophysical Characterisation

This section explores the theories, methods, and techniques involved in evaluating the capture, storage, and release of energy within MOST systems. Optical spectroscopy is

employed to characterise new photochromic compounds, with a specific focus on absorptivity and thermal back conversion half-life.

When a photoactive compound absorbs electromagnetic radiation, it undergoes an energy transition, reaching a higher energy level and become excited. Subsequently, various processes can take place (Figure 7), including relaxation to the ground state through fluorescence or phosphorescence, descending to the ground state *via* vibrational relaxation (generating heat), or triggering a chemical transformation, exemplified in the norbornadiene case.
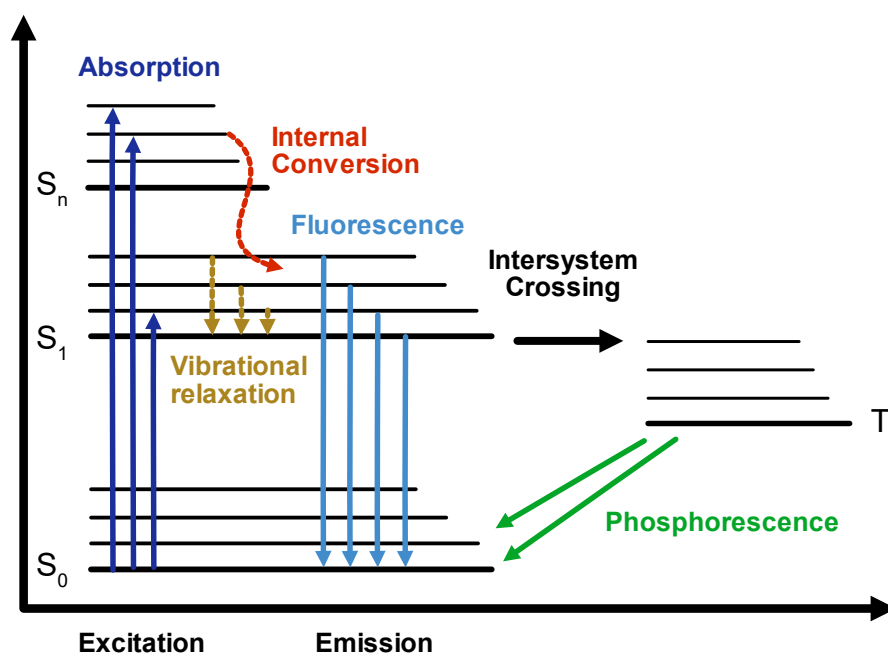
Figure 7. Jablonski diagram to visually represents how molecules move between different energy states, emphasising electronic changes.

4.2.1 Absorption

Absorbance, in the UV-vis spectroscopy is defined by comparing the intensity of incoming light (I_o) with the light transmitted through the sample. The quantification of compound absorption is accomplished through UV-vis spectroscopy. In a typical experiment, a solution of the compound is illuminated with light of varying wavelengths, and the ratio of incident to transmitted light intensity, termed transmittance, is measured. This transmittance is mathematically correlated with absorbance using Equation 1, where T denotes transmittance and A represents absorbance.

$$T = 10^{-A} \tag{1}$$

Expressed as a dimensionless factor, absorbance (A) is dependent on the sample's concentration (c), the pathlengths of light passing through the sample (l), and the molar absorption coefficient (ε), a qualitative measure describing a molecule's absorption. The quantitative relationship is established through Beer-Lambert law (Equation 2), as showcased below:

$$A = \varepsilon \cdot l \cdot c \tag{2}$$

Knowing the concentrations of a compound allows for the determination of the molar absorption coefficient by measuring absorbance, making UV-vis spectroscopy a useful technique for monitoring reactions. Typically, the molar absorption coefficient is then calculated from the mean value of three independently measured solutions with different concentrations.

4.2.1 Quantum Yield

The quantum yield for a photoisomerisation reaction describes the probability of a parent molecule converting to its corresponding photoisomer after absorbing a photon. To determine this factor, the theory and photochemical method have been established in literature[46]. For a system like the norbornadiene – quadricyclane system, there are three processes that can occur simultaneously: the photo induced conversion process, the photo induced back conversion process and the thermal back conversion process (Figure 7).
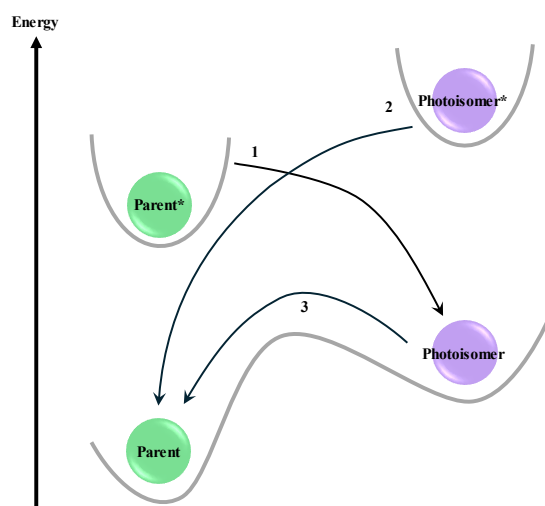
Figure 7. Three processes involved in photoswitching: Process 1 and 2 depict the conversion of the parent compound to the photoisomer or vice versa upon light excitation, while Process 3 demonstrates the thermal conversion of the photoisomer back to the parent compound.

Quantum yield is determined by stepwise irradiation of the parent compound, measuring the resulting concentration change *via* UV-vis spectroscopy. To account for the fluctuating photon flux of the irradiation source, chemical actinometry is employed using a known quantum yield reference, such as potassium ferrioxalate[47] (Figure 8). This involves stepwise irradiation of potassium ferrioxalate, and the subsequent measurement of Fe^{2+} iron using tris-phenanthroline, producing a detectable coloured compound in UV-vis spectroscopy.
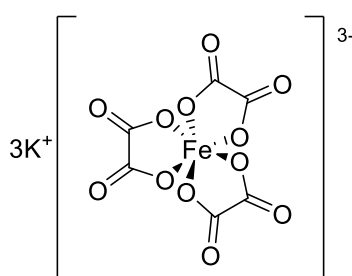
Figure 8. Complex of Fe^{2+} and phenanthroline.

The aforementioned three processes can be described by Equation 3 where A refer to unitless absorbance; Φ_{parent}, $\Phi_{photoisomer}$ represents quantum yield of photon induced conversion and back conversion, respectively; I corresponds to the photonflux; β_{parent} and $\beta_{photoisomer}$ refer to the fraction of photons absorbed by the parent compound and photoisomer; Avogadro's

number, N_A; V is the reaction volume of the solution and k_t corresponds to the rate constant from the photoisomer to the parent compound and [*photoisomer*] is the concentration of the photoisomer.

$$\frac{d[parent]}{dt} = \text{Parent}^* \rightarrow \text{Photoisomer} + \text{Photoisomer}^* \rightarrow \text{Parent} + \text{Photoisomer} \rightarrow \text{Parent}$$

$$\frac{d[parent]}{dt} = -\frac{\phi_{parent} \cdot I \cdot \beta_{parent}(t)}{N_A \cdot I} + \frac{\phi_{photoisomer} \cdot I \cdot \beta_{photoisomer}(t)}{N_A \cdot I} + k_t[photoisomer] \quad (3)$$

The photoisomerisation process of the parent compound to the photoisomer can be simplified by making certain assumptions. Performing the experiment at a low temperature ensures that the thermal back-conversion is slow, rendering process 3 negligible. Additionally, having a concentrated sample of the parent compound with high absorbance at the irradiation wavelength ensures that almost all photons are absorbed by the parent compound, making process 2 negligible and the $\beta_{photoisomer}(t)$ term and $k_t[photoisomer]$ can be equal to zero. Under these assumptions, applying the Lambert-Beers law to the rate expression yields a linear dependence (Equation 4), where [Parent] is the concentration of the parent compound, $[Parent]_0$ is the initial concentration, and t_{irr} is the irradiation time.

$$[Parent] = [Parent]_0 - \frac{\phi_{parent} \cdot I}{N_A \cdot V} \cdot t_{irr} \quad (4)$$

4.2.3 Cyclability Studies and Half-Life

The robustness of a photoswitchable system can be assessed through a cycling study. Initially, irradiating the parent compound leads to its conversion into the photoisomer, followed by regenerating the parent compound by heating the sample. Thus, the study involves alternating irradiation with heating. UV-vis spectroscopy is used to analyse the results, where an unchanged absorption spectrum of the parent compound before and after cycling indicates no degradation. Any variance in the spectra enables determination of the extent of degradation.

The rate of a chemical reaction is influenced by temperature, with two common equations used to describe this correlation: the Arrhenius equation and the Eyring equation. The Arrhenius equation is empirical, while the Eyring equation is derived from transition state theory. In these

equations, k represents the rate constant, A is a constant specific to each chemical reaction, E_a is the activation energy, R is the universal gas constant, T is the absolute temperature, κ is the transmission coefficient, k_B is Boltzmann's constant, h is Planck's constant, $\Delta S^{\ddagger}$ is the entropy of activation, and $\Delta H^{\ddagger}$ is the enthalpy of activation.

$$k = Ae^{-E_a/RT} \tag{5}$$

$$k = \frac{\kappa k_B T}{h} e^{(\Delta S^{\ddagger}/R)} e^{(-\Delta H^{\ddagger}/RT)} \tag{6}$$

UV-vis spectroscopy enables the measurement of rate constants by monitoring the concentration of formed species. In reactions following first-order kinetics, the formation of species (X) undergoes exponential decay, according to the integrated rate law (Equation 7), where [X] represents the concentration of the formed species, $[X]_0$ denotes the initial concentration, k is the rate constant, and t is the reaction time.

$$[X] = [X]_0 e^{-kt} \tag{7}$$

The thermal back-conversion kinetics of norbornadiene and azobenzenes photoswitches display first-order behaviour. Determining the rate constants at various temperatures provides insight into the stability of the corresponding photoisomers. With these rate constants across temperature ranges, an Eyring plot can be created using the linear form of Equation 8, allowing for the extraction of information about the enthalpy and entropy of activation from the slope and intercept, respectively.

$$\ln\left(\frac{kh}{\kappa k_B T}\right) = -\frac{\Delta H^{\ddagger}}{R} \cdot \frac{1}{T} + \frac{\Delta S^{\ddagger}}{R} \tag{8}$$

Following this, extrapolation from the Eyring plot facilitates the determination of the rate constant at any given temperature. The rate constant at 25°C acts as a reference point for comparing the stability of different photoisomers, (Equation 8), where $t_{1/2}$ represents the half-life and k denotes the rate constant.

$$t_{1/2} = \frac{\ln(2)}{k} \qquad (9)$$

4.2.4 Phase-Transition Temperatures and Energy Storage

Differential scanning calorimetry (DSC) serves as a thermal-analytical instrument capable of measuring various parameters, including melting and crystallisation points, heat capacity, and energy release or consumption in processes such as isomerisation and phase change. In MOST applications, DSC facilitates the measurement of the energy release ΔH_{IE} during thermally activated back isomerisation from the photoisomer to the parent molecule, providing a direct method for determining the energy storage capacity ΔH_{Tot}. Moreover, in cases where the system exhibits phase change behaviour, DSC can determine the value of ΔH_{Tot}, which encompasses both ΔH_{IE} and latent heat energy from recrystallisation after melting ΔH_{Cryst}.

$$\Delta H_{IE} + \Delta H_{Cryst} = \Delta H_{Tot} \qquad (10)$$

4.2.5 Solubility

Solubility testing involved weighing out a precise amount of the sample into a vial and then carefully adding specific low volumes of the solvent. The mixture was stirred, and if the sample had not dissolved within 12 hours, additional increments of the solvent were added. This iterative process continued until complete dissolution of the compound was achieved.

Chapter 5

RESULTS AND DISCUSSION

5.1 Synthesis and Purification of Norbornadienes

To investigate how functionalising other sites of the NBD affects the system's properties, we devised a one-step synthesis using readily available starting materials, with consideration of the push-pull conjugation across the entire molecule. Diels-Alder reactions between electron-donating dienes and electron-poor dienophiles are generally highly efficient and simplistic, where reactions have fast reaction rates, higher yields, and potential for tailored selectivity. However, when reacting with a cyclopentadiene in the unsubstituted case, the formation of a dimer needs to be considered which can result in lower yields. Typically, for minimally substituted NBDs the unsubstituted dicyclopentadiene is cracked in flow chemistry and reacted with the alkyne to yield the NBD (Figure 9). In this work, cracking to yield the cyclopentadiene was achieved by microwave-assisted synthesis. Unlike flow chemistry, this method requires longer reaction times, but it benefits from being easier to perform[48]. Fortunately, these challenges were avoided in the other NBD syntheses since the substituted cyclopentadienes used in this study were purchased as monomers and did not dimerise.
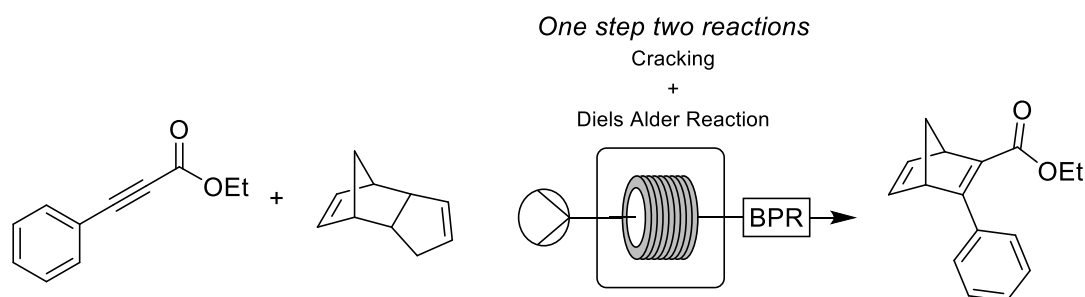
Figure 9. Overview of cracking dicyclopentadiene for the subsequent synthesis of donor/acceptor norbornadienes using a stainless-steel tubular coiled flow reactor and back-pressure regulator (BPR).

Previous syntheses of similar NBDs utilised different solvents – notably when cracking dicyclopentadiene using microwave-assisted synthesis, o-dichlorobenzene (oDCB) was employed to accommodate the higher temperatures required. However, oDCB is not only toxic but also time-consuming and difficult to remove due to its high boiling point of 179°C. Therefore, alternative conditions were explored, including running the reaction without a solvent. It was observed that once the cyclopentadiene variant was added to the (substituted) acetylene, the reaction mixture's temperature increased dramatically, indicating that the reaction proceeded in the absence of a solvent.

Table 1. Summary of comparison study between Thermal Synthesis (TR) at room temperature and Microwave-assisted Synthesis (MR) at 170°C. *Temperature of reaction was 60°C.

Molecule	Structure	Type	Solvent	Yield
NBD 1		MR	None	28%
		MR	oDCB	45%
NBD 2		TR	CDCl$_3$	73%
		MR	oDCB	10%
		TR	None	24%
NBD 3		TR	CDCl$_3$	50%
		MR	oDCB	76%
		TR	None	41%
NBD 4		TR	CDCl$_3$	83%
		MR	oDCB	23%
		TR	None	25%
NBD 5		TR*	oDCB	60%
		MR	oDCB	35%
		TR	None	20%
NBD 6		MR	oDCB	34%
NBD 7		TR	CDCl$_3$	85%
		MR	oDCB	26%

Despite the decrease in yields compared to reactions using a solvent, conducting the synthesis neat is more attractive for scale-up. Thus, to assess both yield and sustainability of the reaction, various temperatures, and solvents (and lack thereof) were compared. Moreover, a comparison between thermal synthesis, reactions conducted on a hotplate and microwave-assisted synthesis was also undertaken (Table 1).

As seen with NBD 1, the dimer could be cracked neat and in various solvents. Based on this observation, initial experiments were conducted using microwave-assisted synthesis at higher temperatures to crack any formed dicyclopentadiene. However, increased reaction yields were observed when attempting the reaction as a thermal synthesis at lower temperatures. This was speculated to be due to the absence of competing reactions such as polymerisation of acetylene or polymerisation of the cracked NBD with themselves or each other at high temperatures. These results varied depending on the chemical composition of the reagents, given differences in tendency to form the inactive cyclopentadiene dimer.
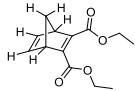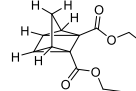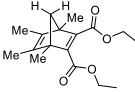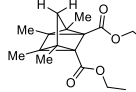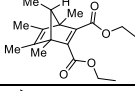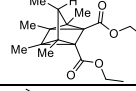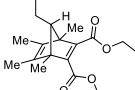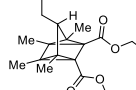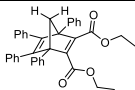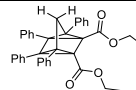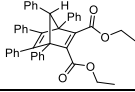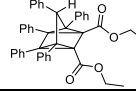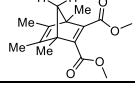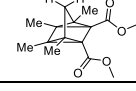
The crude product of the NBD was obtained as an oil after removing the solvent using a rotary evaporator. Analysis of the mixture using NMR revealed the presence of residual alkyne starting material, dimerised cyclopentadiene, the NBD product and the corresponding photoisomer. Once synthesised, NMR analyses were conducted on both the NBDs and its photoisomer (QC) counterparts after irradiation. Obtaining a clean NMR of the NBD product, free from traces of QC, proved challenging and indicated the molecule's ease of photoswitching, complicating structural analysis using techniques such as NMR (multiple peaks), mass spectrometer (no distinction between NBD and QC) and IR spectroscopy (multiple peaks).

To improve sample purity during measurements, extra care was taken throughout the entire synthesis, purification, and storage processes. One method employed to minimise impurities, was to conduct the reactions in amber vials to shield them from light. This was possible due to a small total volume of the reaction as it was carried out neat. After purification, the samples were stored once again in amber vials within a box covered in aluminium foil and placed in a freezer at -80°C. These precautions contributed to obtaining cleaner structural data for the samples, facilitating the characterisation of challenging molecules such as NBD 4, as they decreased the occurrence of photoisomerism and degradation, albeit at a cost of some water impurities, which were subsequently removed before photocharaterisation.

Due to the challenge of separating these chemicals, particularly the NBD and QC, hydrodynamic volumes were calculated using Density Functional Theory (DFT) by Joost

Kimpel and it was concluded that purification using High Pressure Liquid Chromatography (HPLC) was feasible; however, it may not be suitable for all molecules (Table 2).

Table 2. Volumes of different molecules determined by smallest enclosing sphere analysis of conformers.

Molecule	Structure	Volume (Å^3)	Molecule	Structure	Volume (Å^3)	ΔV (%)
NBD 1		534 ± 8	QC 1		656 ± 16	+ 23
NBD 2		804 ± 16	QC 2		768 ± 15	- 4.5
NBD 3		867 ± 14	QC 3		856 ± 9	- 1.3
NBD 4		1125 ± 7	QC 4		1107 ± 9	- 1.6
NBD 5		1651 ± 9	QC 5		1474 ± 11	- 12
NBD 6		1511 ± 27	QC 6		1462 ± 7	- 3.2
NBD 7		530	QC 7		491	- 7.4

The purification process began with NBD 2 using preparative recycling HPLC, where the product underwent approximately 40 cycles over 1110 minutes to obtain a pure sample of the NBD product (Figure 10). Monitoring was conducted at four different wavelengths (210, 240, 300 and 330 nm) chosen to distinguish between the NBD and QC and after the initial cycles, impurities that started to separate were discarded while the remainder was recycled. Around the 200 minutes mark, another impurity peak emerged, exhibiting similar wavelength peaks as the desired product. Subsequently, a smaller peak without peaks at 300 and 340 nm appeared, later identified as QC. Using recycling prep HPLC, the NBD product was successfully separated from the photoisomer whilst limiting exposure to light.
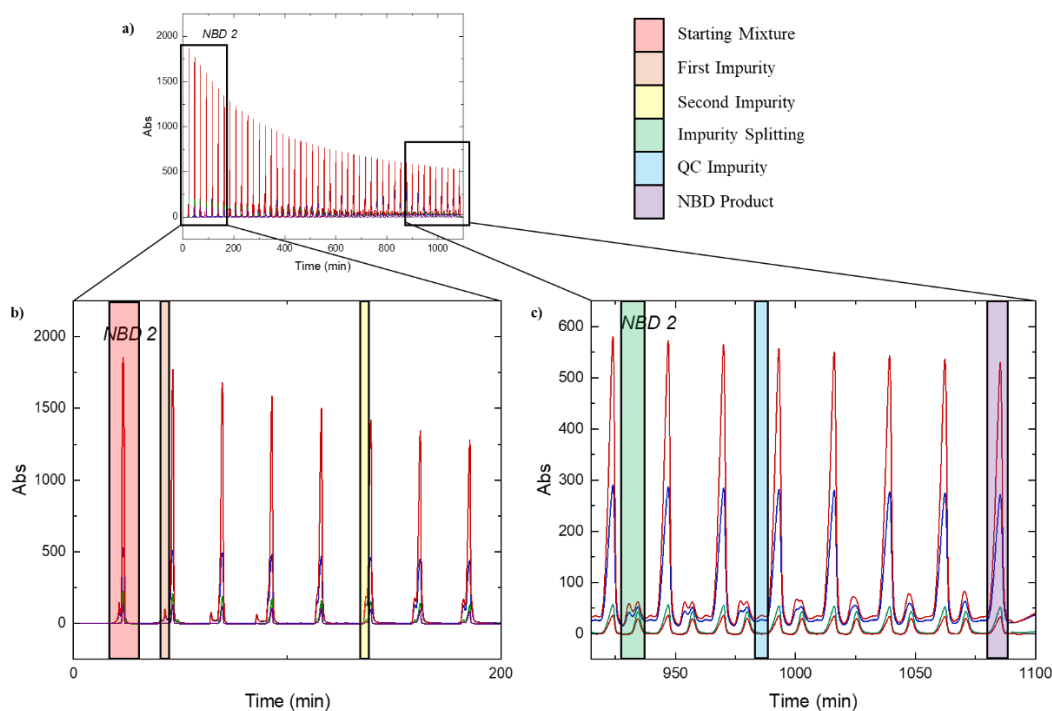
Figure 10. Separation using High Pressure Liquid Chromatography (HPLC) with (a) the full chromatogram, (b) the first 8 cycles, and (c) elution of the product. Different isolated fractions annotated by colour.

When working with samples NBD 3 and 4, larger batches were attempted, meaning HPLC was no longer the most viable option for purification due to the time increase required to cycle and purify batches. Maximum loading on a HPLC column is generally limited to 500 mg, meaning that the 5 g batches would take 180 hours to fully purify (as per 18 h of purification for 300 mg of NBD 1). Therefore, the crude product was purified by distillation in a Kugelrohr apparatus under a 5 mtorr dynamic vacuum. This method successfully removed the alkyne, given its lower boiling point, and also aided in cracking and removing the residual dicyclopentadiene. Although this method proved effective, it was difficult to protect the samples from light exposure. This was exemplified during NMR analysis, where a mixture of the parent and photoisomer was observed, making characterisation complex. Consequently, the samples were prepared once again and purified using automated flash chromatography with a gradient of 0-20% ethyl acetate in hexane. This chromatography method proved easier for light protection compared to the Kugelrohr apparatus, however, was unable to fully remove the acetylene. Accordingly, small fractions of NBD 3 and 4 were purified with HPLC which proved successful (Figure 11).
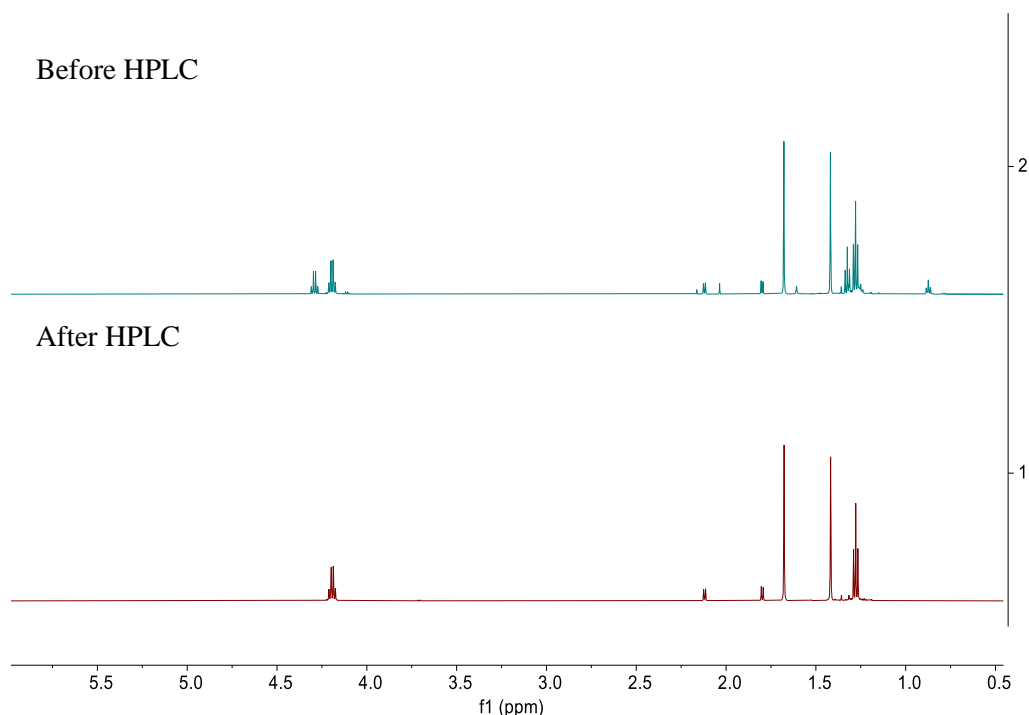
Figure 11. NMR spectrum of NBD 3 recorded in d-chloroform at 298K before (top) and after (bottom) purification by High Pressure Liquid Chromatography (HPLC).

NBD 5 and 6 when left to cool down, crashed out in their solvent mixtures and were vacuum filtrated to yield white solids for both. To obtain a purer sample, the solids were redissolved and columned to separate any unreacted starting material and then recrystallised. Similarly, after purifying NBD 7 using the automated column the sample also crystallised as a yellow solid.

5.2 Properties of Norbornadienes

5.2.1 Solubility
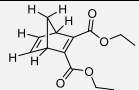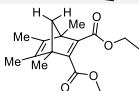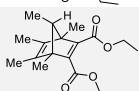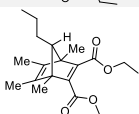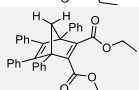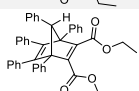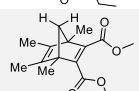
The solubility of the synthesised NBDs was tested given the limited solubility of NBDs in the current generation of MOST systems. This limited solubility adds complications when incorporating the material into a device. Through qualitative analysis of crude experimental data of the solubility of the NBD derivatives, it was observed that the placement, number, and identity of substituents were contributing factors to the compound's solubility. As the number of substitutions increased (NBD 1 – NBD 3), there was a corresponding increase in solubility which was also evident with longer chain lengths on the bridge (NBD 3 and NBD 4). When

compared to the NBD phenyl variants (NBD 5 and NBD 6), it was noted that the bulkier groups were significantly less soluble.

Whilst these findings highlight the improved solubility achieved through the addition of alkyl groups, which could be used to address the previously reported poor solubility in top-performing NBDs in the field, it is important to acknowledge the qualitative nature of the experiment. As NBD 1 – NBD 5 appear as palely coloured oils, discerning their complete dissolution by eye proves challenging, particularly due to the need for dim lighting during experiments. Consequently, the quantity of solvent required to fully dissolve a sample may vary. In future studies, this will be quantified using UV-vis to determine when the solute has fully dissolved alternatively, redoing the study at lower temperatures to encourage crystallisation in all samples to facilitate a quantifiable determination.

5.2.2 Excitation and Degradation

Table 3. Absorption maxima (A_{max}) Absorption onset (A_{onset}), and molar absorption coefficient at the absorption maximum (ε_{max}) for NBD 1 to NBD 7.

Entry	Structure	A_{max}	A_{onset}	M_w	ε_{max}
NBD 1		232	282	236.3	4304
NBD 2		239	293	292.4	3768
NBD 3		234	315	306.4	4738
NBD 4		242	286	334.5	4039
NBD 5		220	294	540.7	12198
NBD 6		-	-	616.8	-
NBD 7		240	276	264.3	4452

The UV-vis spectra of the new NBD series were recorded in both acetonitrile (MeCN) and toluene (Table 3). The NBD data was compared to one another to observe the effects altering the number of sites had on the absorption spectra (Figure 12). As the number of carbons around

the NBD structure (NBD 1 to NBD 4) increases, there is a slight redshift in spectra. However, this is not seen with the phenyl substituents, as these groups are weakly electron-withdrawing and most likely decease the HOMO – LUMO gap resulting in a more blue-shifted spectrum. Notably, when the ester groups were changed from ethyls to methyls, there was a significant redshift. This is likely because of the steric effects of having the less bulkier methyl groups.
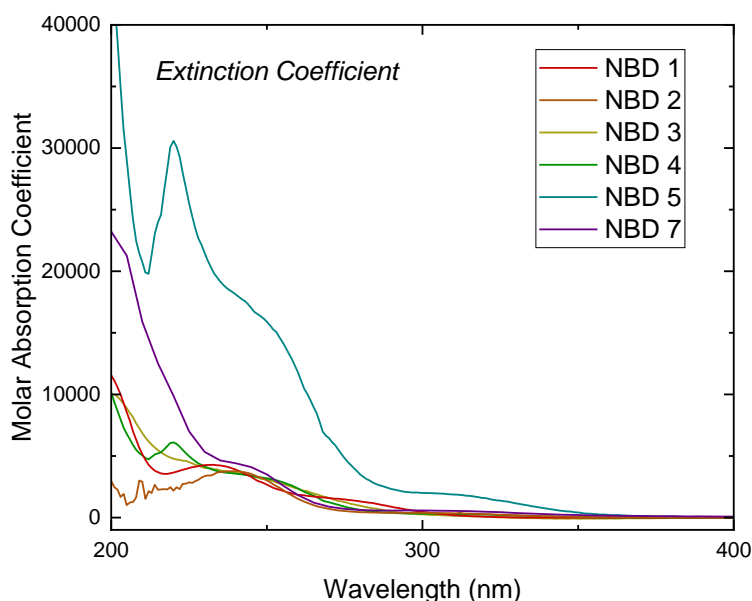

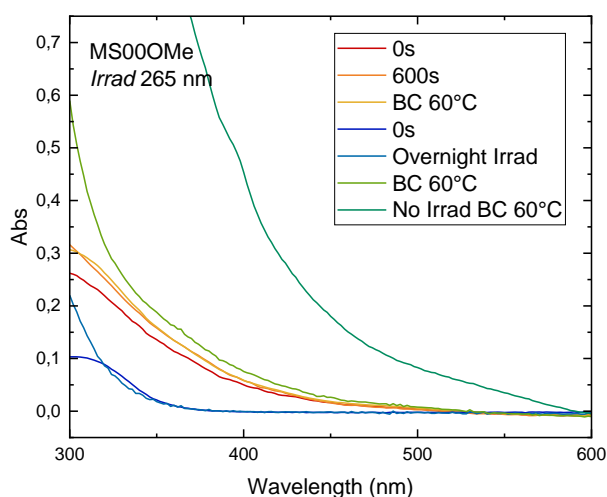**Figure 12. UV-vis absorption spectra of NBD 7 when irradiated for 0 mins, 10 mins and 10 hours and after back conversion at 60˚C. Data for NBD 6 not collected as it was poorly soluble.**

However, upon conversion of the NBDs to their corresponding QC derivatives through irradiation under short UV light (265 nm), it was observed that the molecules underwent degradation. Previous reports indicated that irradiating an ester at 258 nm resulted in a localised excited state, forming a bicyclo[4.1.0] derivative. Therefore, a 300 nm lamp was utilised in an attempt to avoid this mechanism. Additionally, the irradiation was conducted with a degassed solution to investigate for any mechanisms that occurred with ambient oxygen (Figure 13).
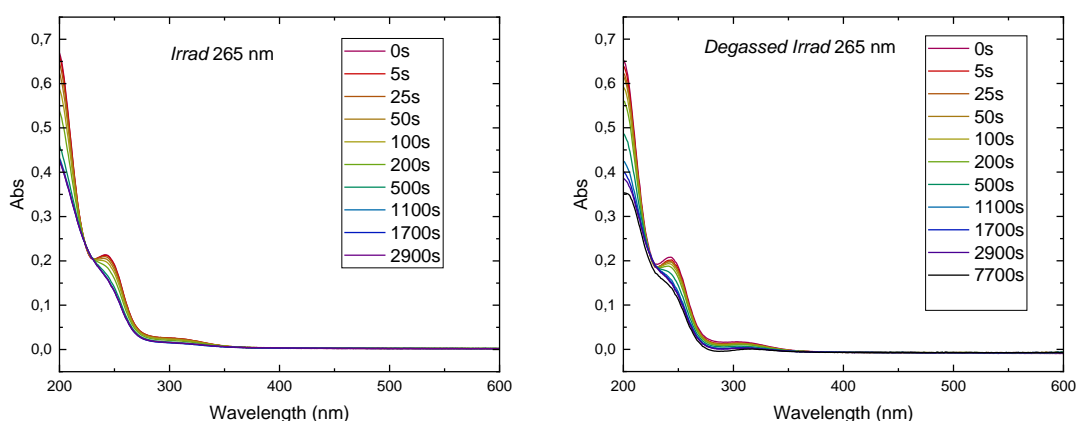
Figure 13. UV-vis absorption spectra of NBD 4 after step irradiation with a 265 nm LED.

Despite these efforts, the degradation persisted after back conversion. To address this issue, *N,N*-dimethylformamide (DMF) with a cutoff wavelength was employed as a solvent to remove input light below 270 nm to minimise photodegradation. However, even when the parent molecule was recovered, degradation was still present although to a lesser extent. Therefore, the degradation of the back conversion was also explored, and the molecule exhibited more degradation at higher temperatures which indicated a combination of mechanisms – possibly a retro Diels-Alder reaction (Figure 14). Consequently, the quantum yield and half-lives of the molecules could not be accurately measured due to the involvement of multiple mechanisms.

Figure 14. UV-vis absorption spectra of NBD 7 when irradiated for 0 mins, 10 mins and 10 hours and after back conversion at 60°C.

27

5.2.3 Quantum Yield

A model system, a pyrene NBD derivative (NBD-2Py) photoswitching behaviour was studied alongside NBD-1Py. The synthesis of these NBDs functionalised with two pyrene groups symmetrically linked *via* the 1 or 2 position of pyrene, has been reported. Owing to the demonstrated high stability of NBD-2Py, a study of its quantum yield and half-life was carried out. When exposed to a 405 nm LED lamp, NBD-2Py switched into the corresponding QC-isomer with almost complete conversion (Figure 15).
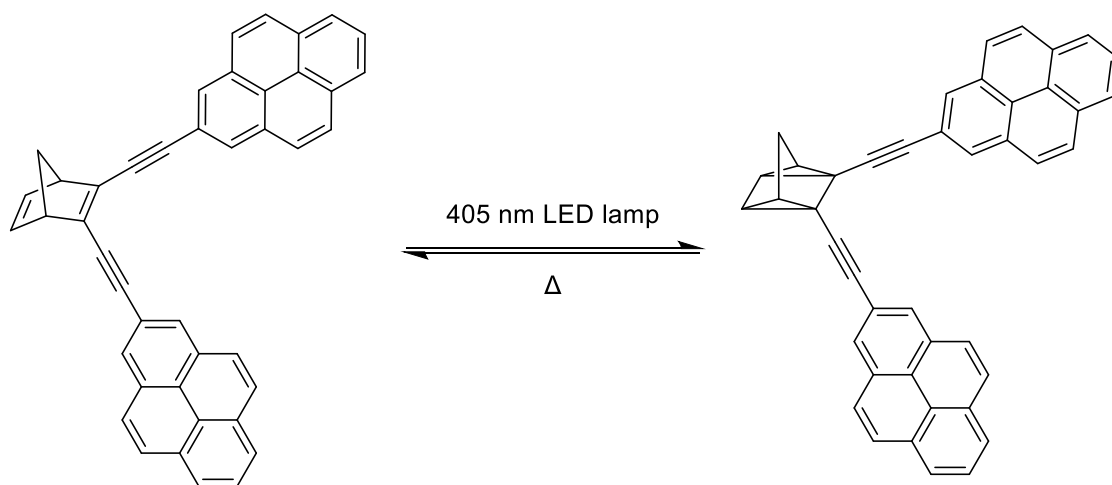
Figure 15. Light induced photoisomerisation of NBD-2Py into the photoisomer QC-2Py and the back conversion using heat.

In tandem to NBD-2Py, NBD-1Py (was also characterised and when exposed to light exhibited behaviour suggesting degradation or a photochemical reaction in the presence of oxygen. The photoisomerisation quantum yields (Φ NBD$\rightarrow$QC) of both NBD systems were measured using a ferrioxalate actinometer. As expected, NBD-1Py exhibited a very small quantum yield, given that the entire system undergoes changes during isomerisation. In contrast, the NBD-2Py system demonstrated a photoisomerisation quantum yield of 46% (Figure 16).
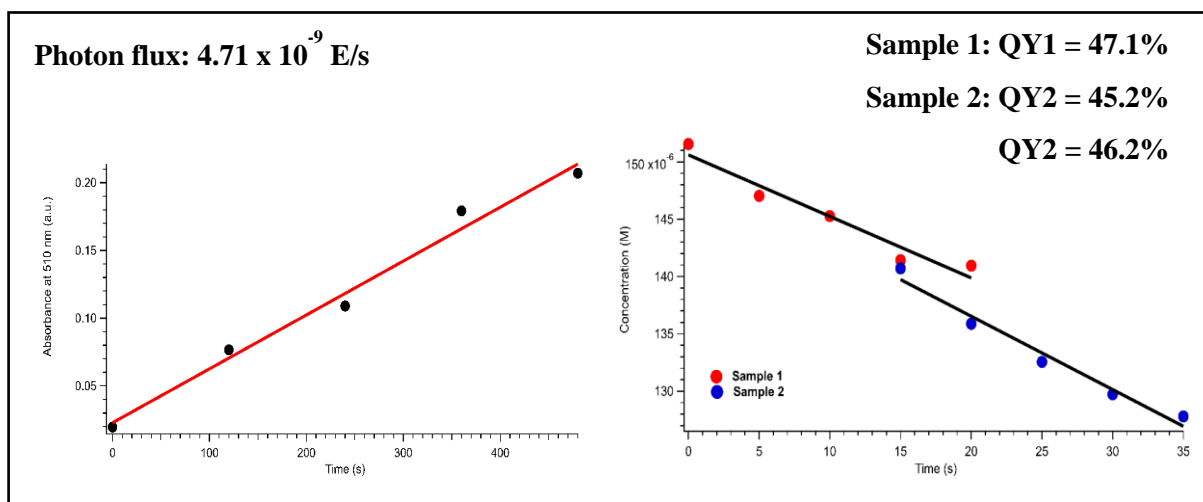
Figure 16. Measures of the photoisomerisation quantum yield for NBD-2Py to QC-2Py isomerisation.

5.2.4 Half-life and cyclability

Another characteristic that made NBD-2Py a model system for testing was that the back conversion induced by temperature revealed a half-life of approximately 15 minutes (Figure 17). For the application of a MOST system this is not ideal as the molecules ideally should have a long shelf-life. However, for running cyclability studies and stability overtime, it is more desirable.
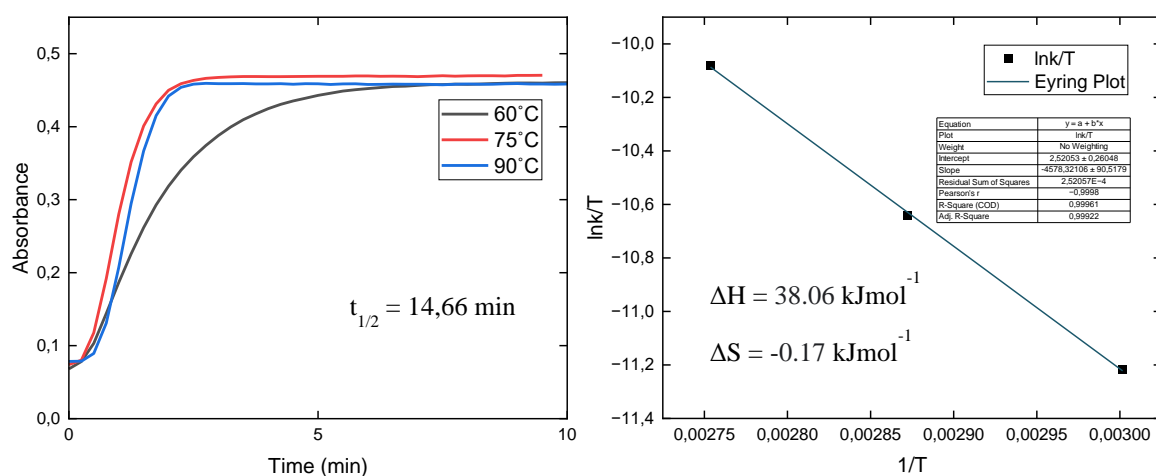
Figure 17. Measures of the half-life of thermal isomerisation of QC-2Py to NBD-2Py.

Consequently, using an automated setup that controlled the irradiation time with the 405 nm LED lamp, more than 100 cycles were completed within a span of 2 days. The degradation rate per cycle was exceptionally slow, and there was virtually no loss in absorption, even after completing 120 cycles. Following this, a larger-scale cycling experiment was conducted, exposing NBD-2Py to 3000 cycles (Figure 18). Despite encountering an inconsistent degradation rate in this experiment, over a third of the original compound was successfully recovered. With further improvements to the method where the system could be made fully automated a more consistent degradation could be recorded – with one major difference being
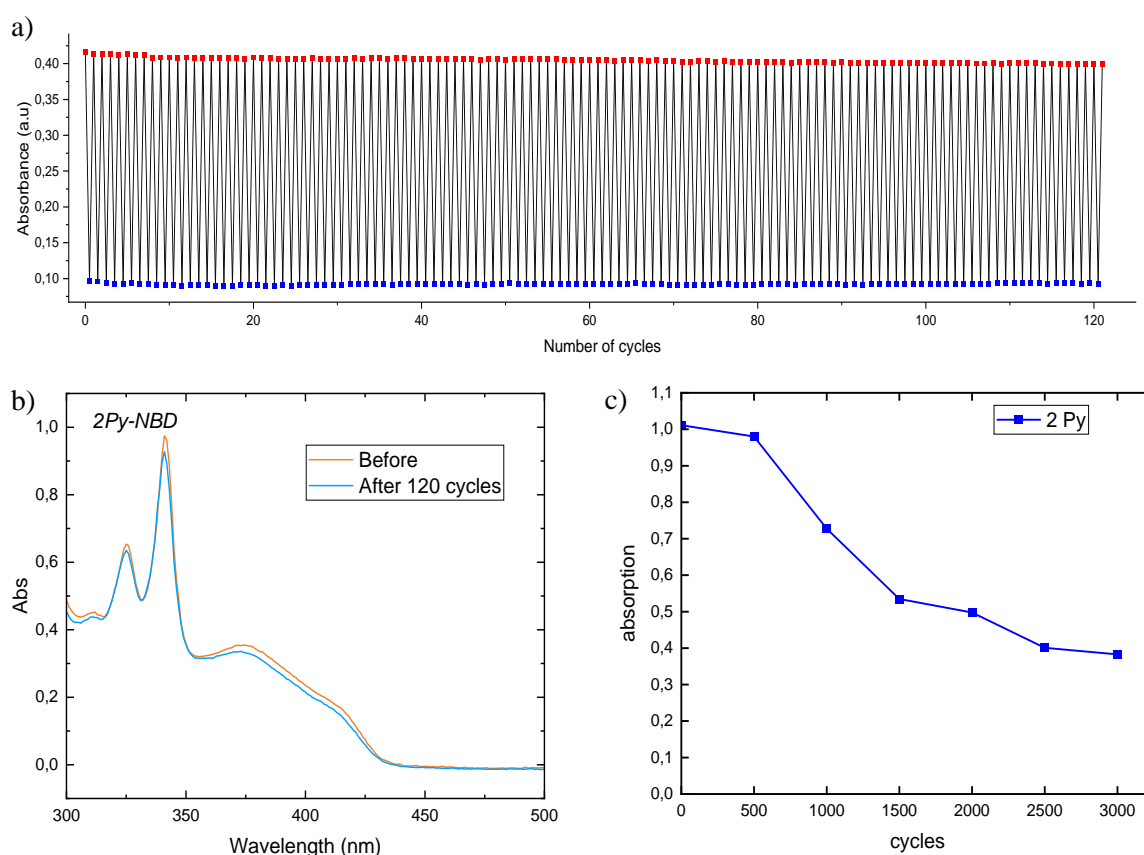
the 1000 cycles between 500 and 1500 not being constantly stirred.

Figure 18. a) Absorption of NBD-2Py and QC-2Py at 392 nm through 120 cycles of photo and thermal switching. b) The absorption profile before and after the 120 cycles. c) 3000 cycles of NBD to QC to NBD conversion of the NBD-2Py/QC-2Py system, measured every 500 cycles.

5.3 Properties of Azobenzenes

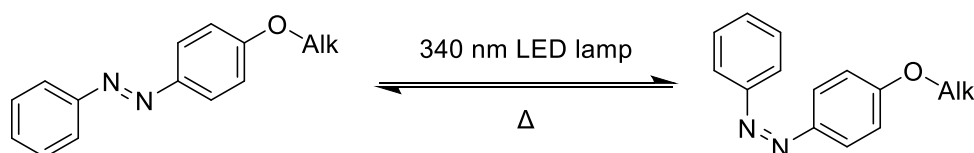### 5.3.1 Phase Change Behaviour

Figure 19. The photoisomerisation process where *trans*-azo is converted to *cis*-azo and the back conversion from the *trans*-isomer to the *cis*-isomer.

Azobenzene (azo) derivatives were studied owing to their photoisomerisation from *trans*-azo to *cis*-azo, demonstrating phase change behaviour (Figure 19). This indicates that the system would store more energy, combining the isomerisation energy and the latent heat energy, to be released as an increase in energy. DSC was used to determine the T_c and T_m of the *trans*-azo systems (Figure 20). The sharpness of these peaks indicates a high degree of crystallisation due to the stacking in the solid state whereas for the *cis*-azo photoisomer it is generally more amorphous. There is a general trend that as the carbon chain length increases the T_m increases which is important when comparing it to the solid-to-liquid transition of the *cis*-azo. By cooling the photoisomer first in the DSC, the glass transition T_g can be evaluated. Subsequently, by varying the length of the substituent group R, the temperature can be altered to be below RT inducing a phase change upon irradiation. The broad peak demonstrates that the crystallisation process is slower and sometimes not observed in comparison to the *trans*-azo which could mean the *cis*-azo no longer possesses a favourable stacking structure resulting in weaker van der Waals forces in the solid-state. Alternatively, the *cis*-azo possess a dipole whereas the *trans*-isomer does not which could lead to competing intermolecular forces and thus increased entropy. The *cis*-azos are oily liquids after irradiation and therefore do exhibit phase change behaviour at lower temperatures which is evident by the broad T_g peak and as the number of carbons in the alkoxy chain increases this results in an increase in T_g.
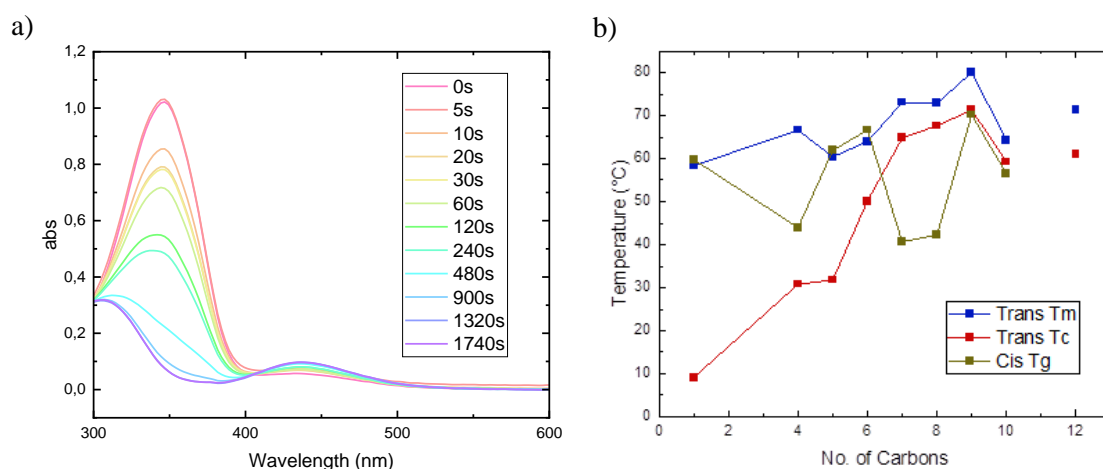
Figure 20. (a) UV-vis absorption spectra after step irradiation with a 340 nm LED. (b) T_m, T_c and T_g of azobenzene two isomeric forms as a function of chain length. All temperature points were determined by differential scanning calorimetry (DSC).
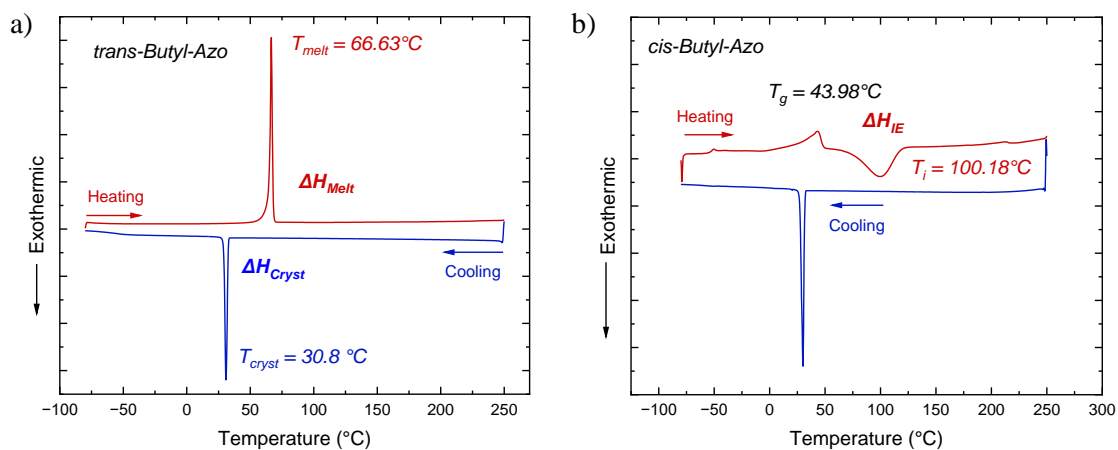
5.3.2 Energy Storage

Figure 21. DSC curves of (a) *trans*- and (b) *cis*-isomers of 4-butoxy-azobenzene.

The amount of energy, ΔH_{Tot} that can be stored in a MOST-PCM material such as the azobenzenes, can be evaluated by determining the isomerisation enthalpy ΔH_{IE} between the *cis*-liquid to *trans*-liquid and crystallisation enthalpy ΔH_{Cryst} of the *trans*-liquid to *trans*-crystal transition (Figure 21). From the DSC curves, the integrated area of the broad exothermic peak

32

in the heating of the thermally induced back isomerisation represents the ΔH_{IE}. No general trend in ΔH_{IE} was observed with increasing carbon chain length, mostly attributed to large fluctuation at the hexa-azo. The sharp exothermic peak in the cooling curves represents the ΔH_{Cryst} of the rapid phase change transition. However, with increasing carbon chain length the ΔH_{Cryst} increased up until six carbons, where it started to decrease (Figure 22).
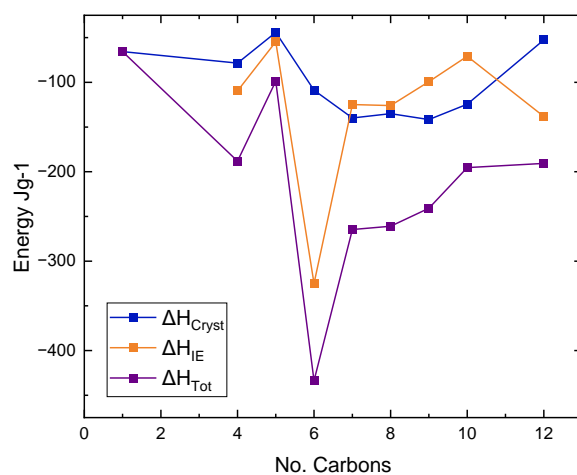

Figure 22. Graph depicting the ΔH_{Cryst}, ΔH_{IE} and ΔH_{Tot} in Jg⁻¹.

Chapter 6

CONCLUSION AND FUTURE WORK

6.1 Conclusion

In conclusion, this study contributes valuable insights by exploring an array of conditions to optimise the synthesis and purification of norbornadienes (NBDs) for application in molecular solar thermal systems (MOSTs). Through a one-step synthesis approach, we successfully generated a series of functionalised NBD derivatives, addressing challenges such as dimer formation and selecting suitable reaction conditions. Purification of the NBD products posed challenges, particularly regarding separation from the corresponding photoisomers. While HPLC purification was effective for smaller batches, distillation and flash chromatography were employed for larger-scale purification, albeit with varying degrees of success. UV-vis spectroscopy provided valuable information on absorption spectra shifts, while photodegradation during conversion to quadricyclane (QC) derivatives complicated quantum yield and half-life determinations.

Furthermore, the investigation of a pyrene-based NBD derivative, NBD-2Py, offered insights into its stability, photoisomerisation behaviour, and back conversion induced by temperature. Upon exposure to a 405 nm LED lamp, NBD-2Py exhibited nearly complete conversion to the corresponding quadricyclane (QC) isomer. As anticipated, NBD-1Py exhibited a small quantum yield, while NBD-2Py demonstrated a notably higher photoisomerisation quantum yield of 46%. Automated setups enabled cycling studies, revealing slow degradation rates and potential for large-scale cycling experiments. These findings contribute to the understanding of the stability and energy storage potential of pyrene-based NBD derivatives by showcasing the robustness and resilience of the NBD system against photodegradation.

The study of azobenzene derivatives uncovered their phase change behaviour and energy storage potential. Differential scanning calorimetry (DSC) elucidated transition temperatures and energy storage capabilities, with observations of increasing T_m with carbon chain length

and fluctuations in ΔH_{IE}., advancing the development of efficient and sustainable energy storage solutions for MOST-PCM systems.

6.2 Future Work

Continuing from the NBDs presented in this thesis, with further functionalisation, an improved series can be synthesised. This may be actualised by tailoring the substituents to better achieve the push-pull system and therefore increasing energy density storage. For example, by selecting groups that optimise the conjugation across the double bond with both substituents on either side or by creating a combination of both electronic and inductive withdrawing groups to maximise the withdrawing effects.

Moreover, further considerations to these substituents can be taken in order to improve stability as well as introduce the desired phase change behaviour and red-shifted spectra within NBD systems. With bulkier groups the backwards energy barrier can be raised as the free rotation available in the QC can lead to disfavourable alignments for the back conversion. Additionally, substituents with increased electron donating power can by implemented to further amplify the system.

ACKNOWLEDGMENT

Finally, I want to thank those closest to me, my family. I love you all so very much and I could not be more grateful for everything you have done for me.

Obrigado, Mãe.

.مرسی بابا

Thank you, André.

Teşekkür ederim, Ceren.

Och till min underbara partner, Martin. Tack för förståelsen, stödet och kärleken genom allt. Jag älskar dig så mycket.

BIBLIOGRAPHY

1. N. S. Lewis and D. G. Nocera, *PNAS*, 2006, **103**, 15729-15735.
2. L. Fernández, Cumulative installed solar PV capacity worldwide from 2000 to 2022, https://www.statista.com/statistics/280220/global-cumulative-installed-solar-pv-capacity/, (accessed 2024-04-10).
3. K. Moth-Poulsen, D. Ćoso, K. Börjesson, N. Vinokurov, S. K. Meier, A. Majumdar, K. P. C. Vollhardt and R. A. Segalman, *Energy Environ. Sci.*, 2012, **5**, 8534-8537.
4. A. Lennartson, A. Roffey and K. Moth-Poulsen, *Tetrahedron Lett.*, 2015, **56**, 1457-1465.
5. G. G. D. Han, H. Li and J. C. Grossman, *Nat Commun*, 2017, **8**, 1446.
6. C. L. Sun, C. Wang and R. Boulatov, *ChemPhotoChem*, 2019, **3**, 268-283.
7. V. Caia, G. Cum, R. Gallo, V. Mancini and E. Pitoni, *Tetrahedron Lett.*, 1983, **24**, 3903-3904.
8. H. Taoda, K. Hayakawa, K. Kawase and H. Yamakita, *J. Chem. Eng. Jpn*, 1987, **20**, 265-270.
9. V. I. Minkin, V. A. Bren' and A. É. Lyubarskaya, in *Organic Photochromes*, Springer US, Boston, MA, 1990, pp. 229-244.
10. R. Boese, J. K. Cammack, A. J. Matzger, K. Pflug, W. B. Tolman, K. P. C. Vollhardt and T. W. Weidman, *J. Am. Chem. Soc.*, 1997, **119**, 6757-6773.
11. Z. Wang, J. Udmark, K. Borjesson, R. Rodrigues, A. Roffey, M. Abrahamsson, M. B. Nielsen and K. Moth-Poulsen, *ChemSusChem*, 2017, **10**, 3049-3055.
12. *Belgium Pat.,* BE 498176, 1951.
13. A. T. Blomquist and Y. C. Meinwald, *J. Am. Chem. Soc.*, 1959, **81**, 667-672.
14. J. J. Mrowca and T. J. Katz, *J. Am. Chem. Soc.*, 1966, **88**, 4012-4015.
15. Y. Harel, A. W. Adamson, C. Kutal, P. A. Grutsch and K. Yasufuku, *J. Phys. Chem.*, 1987, **91**, 751-1000.
16. K. Börjesson, A. Lennartson and K. Moth-Poulsen, *ACS Sustain. Chem Eng*, 2013, **1**, 585-590.
17. S. Miki, Y. Asako and Z. Yoshida, *Chem. Lett.*, 1987, **16**, 195-198.
18. V. A. Bren, A. D. Dubonosov, V. I. Minkin and V. A. Chernoivanov, *Russ. Chem. Rev.*, 1991, **60**, 913-948.
19. V. Gray, A. Lennartson, P. Ratanalert, K. Borjesson and K. Moth-Poulsen, *Chem. Commun.*, 2014, **50**, 5330-5332.
20. E. Mitscherlich, *Annalen der Physik*, 1834, **108**, 225-240.
21. D. R. Waring, in *Comprehensive Heterocyclic Chemistry*, eds. A. R. Katritzky and C. W. Rees, Pergamon, Oxford, 1984, vol. 1, pp. 317-346.
22. G. S. Hartley, *Nature*, 1937, **140**, 281-281.
23. A. A. Beharry and G. A. Woolley, *Chem. Soc. Rev.*, 2011, **40**, 4422-4437.
24. E. Besson, A. Mehdi, D. A. Lerner, C. Reyé and R. J. P. Corriu, *J. Mater. Chem.*, 2005, **15**, 803-809.
25. J. Van Hoorick, H. Ottevaere, H. Thienpont, P. Dubruel and S. Van Vlierberghe, *Polymer and Photonic Materials Towards Biomedical Breakthroughs*, 2018.
26. A. Khayyami and M. Karppinen, *Chem. Mater.*, 2018, **30**, 5904-5911.
27. K. Griffiths, J. L. Greenfield, N. R. Halcovitch, M. J. Fuchter and J. M. Griffin, *Cryst Growth Des*, 2023, **23**, 7044-7052.
28. E. Merino, *Chem. Soc. Rev.*, 2011, **40**, 3835-3853.
29. Z. Mahimwalla, K. G. Yager, J.-i. Mamiya, A. Shishido, A. Priimagi and C. J. Barrett, *Polym. Bull.*, 2012, **69**, 967-1006.

30. A. K. Saydjari, P. Weis and S. Wu, *Adv. Energy Mater.*, 2016, **7**.
31. J. Gao, Y. Feng, W. Fang, H. Wang, J. Ge, X. Yang, H. Yu, M. Qin and W. Feng, *Energy. Environ. Mater.*, 2023.
32. Z. Y. Zhang, Y. He, Z. Wang, J. Xu, M. Xie, P. Tao, D. Ji, K. Moth-Poulsen and T. Li, *J. Am. Chem. Soc.*, 2020, **142**, 12256-12264.
33. Z. Shangguan, W. Sun, Z. Y. Zhang, D. Fang, Z. Wang, S. Wu, C. Deng, X. Huang, Y. He, R. Wang, T. Li, K. Moth-Poulsen and T. Li, *Chem. Sci.*, 2022, **13**, 6950-6958.
34. X. Li, S. Cho and G. G. D. Han, *ACS Mater. Au*, 2023, **3**, 37-42.
35. H. Liu, Y. Feng and W. Feng, *CompComm*, 2020, **21**.
36. Q. Yang, J. Ge, M. Qin, H. Wang, X. Yang, X. Zhou, B. Zhang, Y. Feng and W. Feng, *Sci. China. Mater.*, 2023, **66**, 3609-3620.
37. H.-Y. Zhong, L. Chen, X.-M. Ding, R. Yang and Y.-Z. Wang, *Sci. China. Mater.*, 2018, **61**, 1225-1236.
38. O. Diels and K. Alder, *Justus Liebig's Ann. Chem*, 1928, **460**, 98-122.
39. K. C. Nicolaou, S. A. Snyder, T. Montagnon and G. Vassilikogiannakis, *Angew. Chem. Int. Ed. Engl.*, 2002, **41**, 1668-1698.
40. W.-J. Yoo, G. C. Tsui and W. Tam, *EurJOC*, 2005, **2005**, 1044-1051.
41. K. Sonogashira, Y. Tohda and N. Hagihara, *Tetrahedron Lett.*, 1975, **16**, 4467-4470.
42. R. F. Heck, in *Org. React.*, 1982, vol. 27, pp. 345-390.
43. N. Miyaura and A. Suzuki, *Chem Rev.*, 1995, **95**, 2457-2483.
44. D. Milstein and J. K. Stille, *J. Am. Chem. Soc.*, 1978, **100**, 3636-3638.
45. S. Baba and E. Negishi, *J. Am. Chem. Soc.*, 1976, **98**, 6729-6731.
46. K. Stranius and K. Borjesson, *Sci Rep*, 2017, **7**, 41145.
47. C. G. Hatchard and C. A. Parker, *Proc. R. Soc. Lond.*, 1997, **235**, 518-536.
48. J. Orrego-Hernández, H. Hölzel, M. Quant, Z. Wang and K. Moth-Poulsen, *EurJOC*, 2021, **2021**, 5337-5342.

Paper I

Structure-property relationship in pyrene functionalised norbornadiene-quadricyclane fluorescent photoswitches: characterisation of their fluorescence properties and application in imaging of amyloid beta plaques

Pyrene Functionalized Norbornadiene-Quadricyclane Fluorescent Photoswitches: Characterization of their Spectral Properties and Application in Imaging of Amyloid Beta Plaques

Shima Ghasemi,[a] Monika Shamsabadi,[a] Axel Olesund,[a] Francisco Najera,[b,c] Andreas Erbs Hillers-Bendtsen,[d] Fredrik Edhborg,[a] Adil S. Aslam,[a] Wera Larsson,[a] Zhihang Wang,[e] Francoise M. Amombo Noa[a], Rebecca Jane Salthouse,[j] Lars Öhrström,[a] Helen Hölzel,[j] E. Perez-Inestrosa,[b,c] Kurt V. Mikkelsen,[d] Jörg Hanrieder,[f,g] Bo Albinsson,[a] Ambra Dreos,[f,b*] Kasper Moth-Poulsen.[a,h,i,j*]

[a]   Department of Chemistry and Chemical Engineering, Chalmers University of Technology, 41296 Gothenburg, Sweden

[b]   Instituto de Investigación Biomédica de Málaga y Plataforma en Nanomedicina-IBIMA Plataforma Bionand, 29590 Malaga, Spain

[c]   Departamento de Química Orgánica, Facultad de Ciencias, Universidad de Málaga, E-29071 Málaga, Spain.

[d]   Department of Chemistry, University of Copenhagen, Universitetsparken 5, Copenhagen Ø, Denmark

[e]   Department of Materials Science and Metallurgy, University of Cambridge, 27 Charles Babbage Rd, Cambridge CB3 0FS, U.K.

[f]   Department of Psychiatry and Neurochemistry, Sahlgrenska Academy, University of Gothenburg, 43180 Mölndal, Sweden

[g]   Department of Neurodegenerative Disease, Queen Square Institute of Neurology, University College London, London WC1N 3BG, UK.

[h]   The Institute of Materials Science of Barcelona, ICMAB-CSIC, Bellaterra, 08193 Barcelona, Spain.

[i]   Catalan Institution for Research & Advanced Studies, ICREA, Pg. Llu´ıs Companys 23, 08010 Barcelona, Spain.

[j]   Department of Chemical Engineering, Universitat Politècnica de Catalunya, EEBE, Eduard Maristany 10–14, 08019 Barcelona, Spain

Corresponding authors: Ambra Dreos (ambra.dreos@gu.se); Kasper Moth-Poulsen (kasper.moth-poulsen@upc.edu).
Supporting information for this article is given via a link at the end of the document.

Abstract: This study presents the synthesis and characterization of two fluorescent norbornadiene (NBD) photoswitches, each incorporating two conjugated pyrene units. Expanding on the limited repertoire of reported photoswitchable fluorescent NBDs, we explore their properties with a focus on applications in bioimaging of amyloid beta (Aβ) plaques. While the fluorescence emission of the NBD decreases upon photoisomerization, aligning with what has been previously reported, for the first time we observed luminescence after irradiation of the quadricyclane (QC) isomer. We deduce how the observed emission is induced by photoisomerization to the excited state of the parent isomer (NBD) which is then the emitting species. Thorough characterizations including NMR, UV-Vis, fluorescence, X-ray structural analysis and density functional theory (DFT) calculations provide a comprehensive understanding of these systems. Notably, one NBD-QC system exhibits exceptional durability. Additionally, these molecules serve as effective fluorescent stains targeting Aβ plaques in situ, with observed NBD/QC switching within the plaques. Molecular docking simulations explore NBD interactions with amyloid, unveiling novel binding modes. These insights mark a crucial advancement in the comprehension and design of future photochromic NBDs for bioimaging applications and beyond, emphasizing their potential in studying and addressing protein aggregates.

Introduction

Molecular photoswitches are a class of molecules that undergo reversible structural and property changes upon irradiation with an appropriate light source. Fluorescent photoswitches constitute a subclass of molecular switches that exhibit photochromism; they are fluorescent in one or two of the isomer forms, therefore their emission is toggled ON/OFF or otherwise manipulated by means of photoirradiation. Photochromic molecules have been widely used for different applications such as photochromic glasses[1], fluorescent labelling and bioimaging[2], super-resolution microscopy[3], photopharmacology[4], and others. Several examples of different classes of fluorescent photoswitches include diarylethenes, anthracenes, stilbenes, azo-based compounds, norbornadienes, and spiropyrans.[5] Photoswitchable fluorescent dyes for bioimaging applications have several advantages,[6] as for example advanced probing properties, multi-stimuli responsive and functional biosensors[7], improved signal quality[8], decreased photobleaching[9] and access to a series of advanced imaging

techniques such as super resolution imaging.[2c,10] The norbornadiene-quadricyclane (NBD-QC) photoswitch system has been investigated for different applications such as solar energy storage[11], molecular electronics[12], and bioimaging[13]. Norbornadiene (NBD) derivatives isomerize to highly strained quadricyclane (QC) by photoirradiation and convert back to NBD either by thermal[14], catalytic[11a] or light-induced activation.[15] Only a few photoswitchable fluorescent NBDs have been reported, and the in-depth understanding of their properties is of relevance for a range of applications, including bioimaging of protein aggregates. Previously, Dreos *et al.* investigated a photoswitchable fluorescent norbornadiene (a bis(ethynylphenylene) substituted NBD) as an imaging probe for amyloid beta (Aβ) plaques in Alzheimer disease (AD) mouse models.[13] Aβ protein aggregation is a major pathological hallmark of AD[16] and it recently emerged how Aβ aggregates are highly heterogeneous in their biochemical and morphological composition.[17] Unfortunately, the mechanism of Aβ aggregation and how Aβ toxicity is mediated is at present not fully understood. Gaining insights into how Aβ exerts its neurotoxic effects through changes in aggregation state and biochemical composition represents a fundamental goal in AD research. Aβ aggregation can be interrogated using fluorescent probes that exhibit aggregation-induced fluorescence[18], and photoswitchable probes that change their spectral properties upon irradiation with light have further expanded the imaging field enabling advanced imaging techniques as discussed above.[2c] The previously investigated bis(ethynylphenylene) substituted NBD is able to target and recognize Aβ aggregates, delineating their heterogeneity thanks to hyperspectral properties upon binding; moreover, it was switched off and on in tissue. However, there are still several challenges to be addressed to utilize NBD derivatives for advanced bioimaging techniques. For example, absorption and emission need to be red-shifted,[18] solubility in aqueous systems is needed for extended bio-applications,[18, 21] and QC to NBD switching *in situ* needs to be orders of magnitude faster or fully light-controlled to access advanced imaging applications.[2c, 3a, 21] Herein, we decided to further develop and explore NBD/QC systems for bioimaging applications. Pyrene derivatives have been extensively used to investigate biomolecules.[19] Their fluorescent properties are affected by the polarity of the microenvironment and by their intermolecular distance and orientation since they can form emissive excimers.[19] Moreover, pyrene-modified *trans*-stilbene salicylic acids have been successfully applied to target and study Aβ aggregation,[20] showing potential for applications as fluorescent probes of Aβ aggregates. Therefore, we decided to explore the combination of pyrene with the switchable norbornadiene unit to target Aβ aggregates and to investigate the potential of such systems for bioimaging. The molecular structures of the studied norbornadienes and their synthetic route is described in Scheme 1. NBD-1Py and NBD-2Py are functionalized with two pyrene groups linked via the 1 or 2 position of pyrene, and symmetrically attached to the core NBD molecule. The fluorescence and photoswitching properties of the two

structural isomers are significantly different, and show many interesting aspects, which require extensive spectroscopic and computational investigation to be understood. Additionally, NBD-1Py and NBD-2Py are investigated for Aβ plaques imaging in AD mouse models.

Synthesis

The synthesis of NBD pyrene end-capped molecules is delineated in Scheme 1. 2,3-Dibromonorbornadiene was synthesized from norbornadiene according to the method described in the literature.[22] To synthesize NBD-1Py, 1-ethynylpyrene was reacted with di-bromo NBD *via* Sonogashira coupling. The same procedure is applied for the synthesis of NBD-2Py using 2-ethynylpyrene as a starting material. The detailed synthetic procedures and characterisation are reported in the Supporting Information (SI).
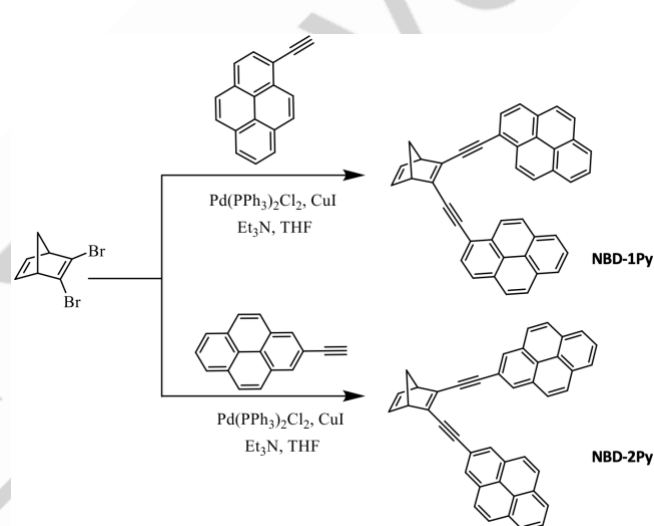
Scheme 1: Synthesis and molecular structures of NBD-1Py and NBD-2Py.

Spectroscopic characterization

Both synthesized norbornadienes are fluorescent, and the absorption and emission spectra of NBD-1Py and NBD-2Py are shown in Figure 1a,b. Interestingly, the emission profiles are quite different in the two systems. Spectral characterizations are complemented with DFT calculations and natural transition orbitals for relevant transitions (See following discussion and SI Section 4 for more details). NBD-1Py has the highest fluorescence quantum yield (55% $\pm$ 2%), while NBD-2Py has a fluorescence quantum yield of 19% $\pm$ 2%. The emission lifetime of NBD-1Py is 2.1 ns, and for NBD-2Py it is 0.8 ns. From the fluorescence quantum yield and the fluorescence lifetime, the fluorescence rate constant was calculated. Note that it is almost identical for both NBD-1Py and NBD-2Py (2.6×10^8 s^{-1} and 2.7×10^8 s^{-1} respectively), which indicates that competing processes such as non-radiative deactivation and photoisomerization are more prominent in NBD-2Py,
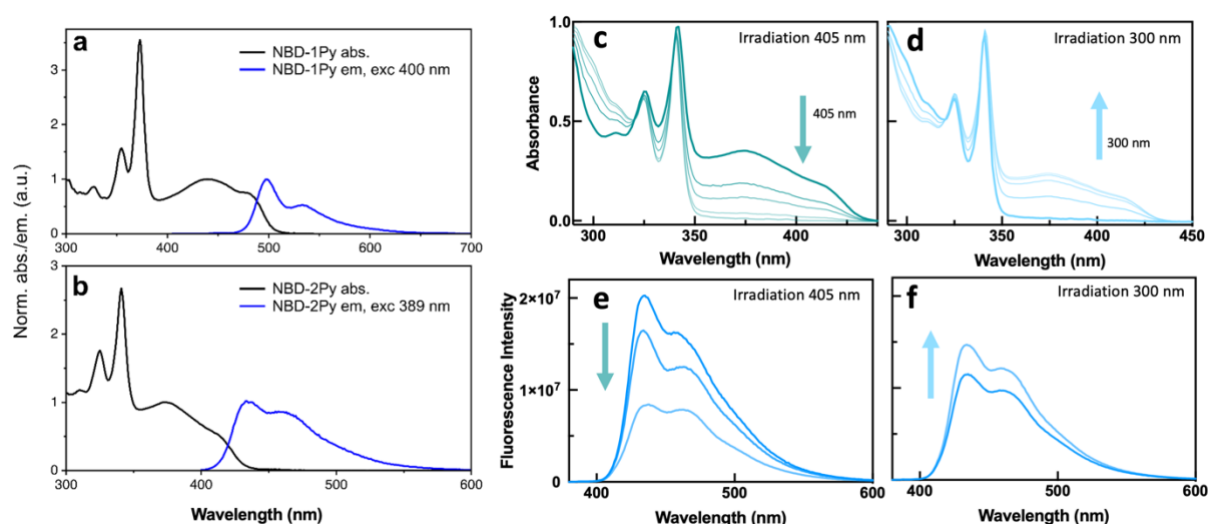
Figure 1: Normalized steady-state absorption and emission of (a) NBD-1Py, and (b) NBD-2Py in toluene. (c) Absorption changes of NBD-2Py isomerising to QC-2Py under 405 nm stepwise irradiations. (d) Absorption changes of QC-2Py isomerising to NBD-2Py under 300 nm stepwise irradiations. (e) Emission changes of NBD-2Py isomerising to QC-2Py under 405 nm stepwise irradiations. (f) Emission changes of QC-2Py isomerising to NBD-1Py upon 300 nm irradiation.

Table 1: Calculated electronic and photophysical data for the dyes NBD-1Py and NBD-2Py.[a]

Compound	Absorption					
	Transition	$f^{[b]}$	Dominant Component (%)[c]	$E_{\text{max calc.}}$ (eV)[d]	$E_{\text{max exp.}}$ (eV) [d]	$\Delta E_{\text{HOMO-LUMO}}$ (eV)[e]
NBD-1Py	$S_1 \leftarrow S_0$	0.996	LUMO←HOMO (88)	2.77	2.82	4.84
	$S_2 \leftarrow S_0$	1.085	LUMO←HOMO-1 (50) LUMO+1←HOMO (42)	3.51		
NBD-2Py	$S_1 \leftarrow S_0$	1.216	LUMO←HOMO (92)	3.18	3.32	5.48
	$S_2 \leftarrow S_0$	0.003	LUMO←HOMO-1 (37) LUMO+1←HOMO (22)	3.68		
	Emission					
NBD-1Py	$S_1 \rightarrow S_0$	1.057	LUMO→HOMO (94)	2.10	2.48	
NBD-2Py	$S_1 \rightarrow S_0$	0.994	LUMO→HOMO (95)	2.43	2.86	

[a] Calculated by TD-DFT at level PCM(toluene)/CAM-B3LYP/cc-pVDZ, corresponding to the $S_1 \leftarrow S_0$ and $S_2 \leftarrow S_0$ (absorption) and $S_1 \rightarrow S_0$ transitions (emission). [b] Oscillator strength. [c] Percentage contribution approximated by 2 x $(c_i)^2$ x100%. [d] Calculated (calc.) and experimental (exp.) energies. [e] Calculated HOMO–LUMO energy band gap.

Figure 2. Molecular orbitals of NBD-1Py and NBD-2Py.

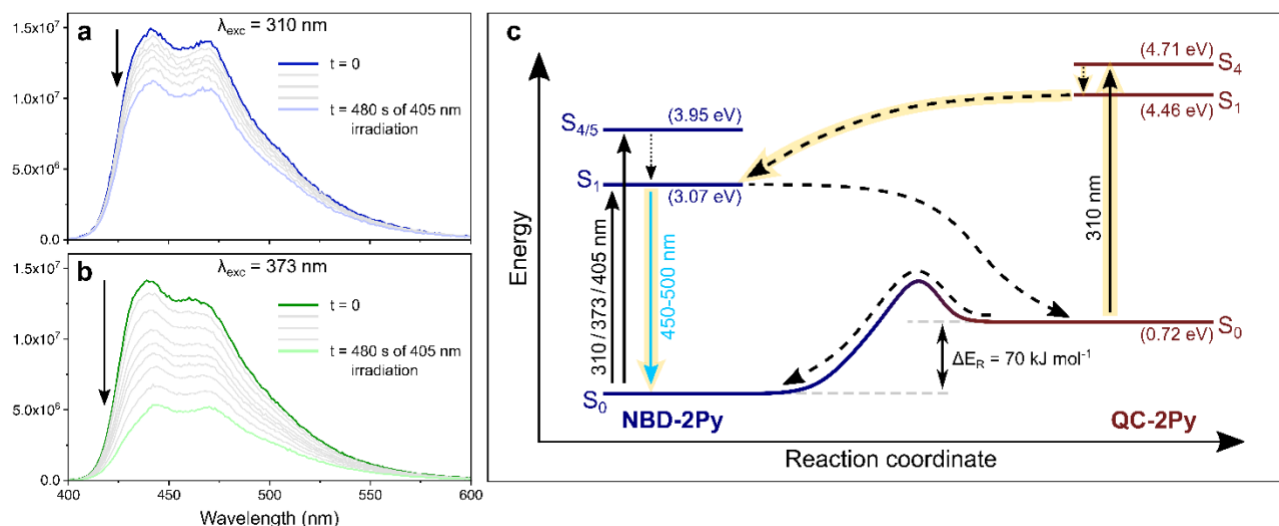|	HOMO-1	HOMO	LUMO	LUMO+1
NBD-1Py				
NBD-2Py				
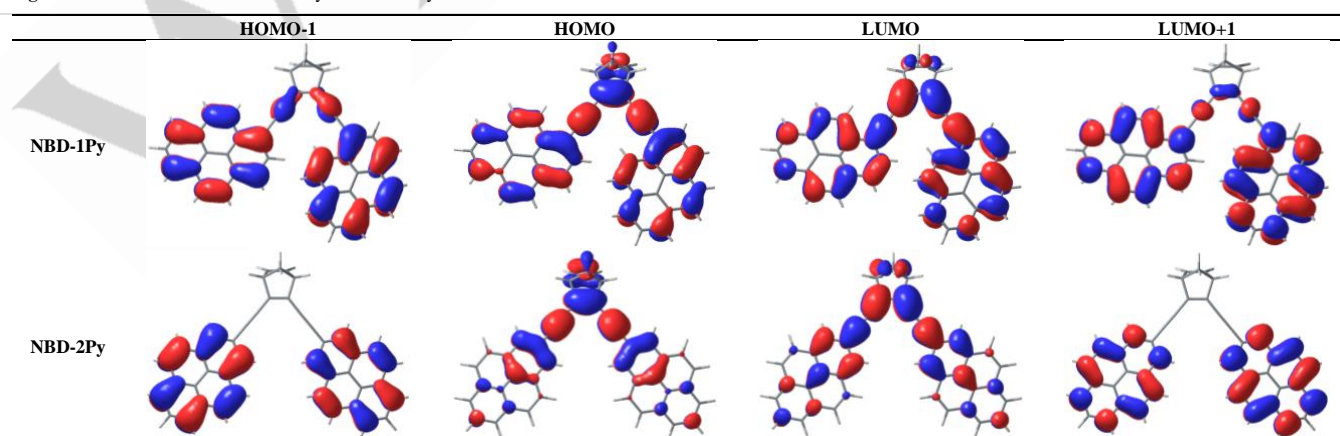
Figure 3: Steady state emission of NBD-2Py measured directly after different times (0-480 s) of exposure to 405 nm continuous-wave irradiation at 0°C. (a) λexc = 310 nm. (b) λexc = 373 nm. (c) Proposed reaction pathways in NBD-2Py. Highlighted in yellow is the suggested reaction pathway of photoinitiated back conversion from QC-2Py to NBD-2Py.

aligning with the observed isomerization behaviours (*vide infra*). Upon irradiation using a 405 nm LED lamp, NBD-2Py photoswitches to the respective QC-isomer with near-quantitative conversion (Figure 1c). The parent isomer of QC-2Py was thermally recovered, and the half-life was calculated to be 15 minutes at room temperature. The quantum yield of the photoisomerization reaction ($\phi_{NBD-2Py \rightarrow QC-2Py}$) was measured to be 46%. On the other hand, when irradiating NBD-1Py it did not seem to photoisomerize to QC, but rather to degrade (see SI Figure S6 for NMR characterization). To rationalize the experimental observations, we calculated DFT optimized geometries and natural transition orbitals for relevant transitions. These calculations show good correlation with the experimental absorptions and emissions of the NBD-derivatives (see Table 1). The absorption and emission of NBD-1Py are bathochromically shifted (ca. 50 nm) with respect to NBD-2Py. This can be explained by a better electronic interaction between the pyrene-ethynyl moiety and the NBD core in NBD-1Py. For this compound, the allowed transitions with a high value of their oscillator strength are the $S_1 \leftarrow S_0$ and the $S_2 \leftarrow S_0$ (see Table 1). For the first of these transitions the dominant component is LUMO←HOMO, for the second one the dominant components are LUMO←HOMO-1 and LUMO+1←HOMO. For NBD-1Py, the electronic density of the molecular orbitals involved in these transitions are distributed along the whole molecule. In contrast, for NBD-2Py only the transition $S_1 \leftarrow S_0$ is allowed with a dominant component LUMO←HOMO (Table 1) for which only one of the pyrene rings are conjugated with the NBD core (see Figure 2). This behaviour is in agreement with the photophysical properties of other previously describe ethynyl-pyrenes substituted in 1- or 2-positions.[23] These subtle differences likely provides also a qualitative explanation as to why NBD-2Py undergo photoisomerization to QC-2Py while NBD-1Py does not.

The isomerization effect on the absorption and emission properties of NBD-2Py was characterized in toluene solution, and upon photoisomerization of NBD-2Py to QC-2Py using a 405 nm LED, the emission measured upon excitation at 373 nm decreases (Figure

3b). This is in line with what has been observed in our previous studies with the fluorescent bis(ethynylphenylene) substituted NBD.[15] Unfortunately, upon extended irradiation at 405nm the emission did not decrease to zero but we observed a low intensity with a different shape (see SI Figure 8 right); based on several observations we deduced that a small amount of emissive impurities form upon irradiation. The emission was measured after stepwise irradiations at 405 nm and keeping the sample at 0°C and under stirring. Interestingly, when the emission was measured with excitation at 310 nm (where the formed QC absorbs), the intensity decreases at a much lower rate than when the emission was measured with excitation at 373 nm, while still retaining the spectral shape of the NBD fluorescence (Figure 3a). Even after maximised isomerization of NBD to QC and with the solution kept at 0°C to minimize thermal back isomerization, the emission remains (see SI Figure S8). While QC could theoretically emit given its pyrene moieties, the measured emission upon excitation at 310 nm resembles that of NBD, both in spectral shape and wavelength of emission, contradicting this hypothesis. Therefore, we believe this is indicative of QC back photoconverting to the NBD form on the excited state surface (S1), followed by emission from the first singlet excited state of NBD. The observed photoisomerization induced fluorescence through adiabatic photoisomerization is (to the best of our knowledge) reported here for the first time in these systems; importantly, an adiabatic QC to NBD photoisomerization mechanism would be different than what has been previously reported.[24]

The samples used for the spectroscopy studies had low concentrations which would prevent eventual intermolecular interactions between pyrenes the units. Based on the known literature regarding emissive excimer formations between spatially close pyrene moieties[19, 25] we investigated the eventual presence of intramolecular excimers in NBD-2Py/QC-2Py. We did not observe any emission indicative of excimer formation in any of the two isomers, which could be due to unfavourable orientation of the pyrene moieties or other processes preventing it.

The robustness of the NBD-2Py over multiple cycles of photoisomerization and thermal back-conversion was also
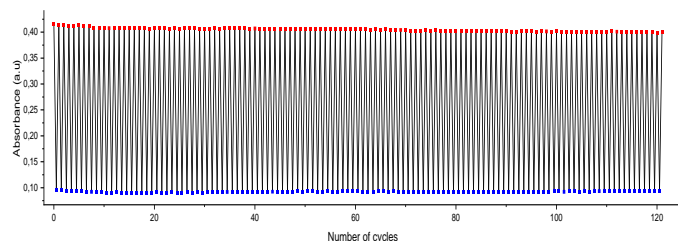
Figure 4: Absorption of NBD-2Py and QC-2Py at 392 nm through 120 cycles of photo and thermal switching.

characterized in solution. The relatively short back-conversion time allowed the utilization of an automated setup connected to a spectrofluorometer, which controlled sample temperature (80 °C) and irradiation intervals with a 405 nm LED. We completed 120 cycles (Figure 4), and notably, NBD-2Py exhibited remarkable stability against photodegradation at this excitation wavelength. Consequently, we conducted a longer photo-thermal cycling experiment, subjecting NBD-2Py to 3000 cycles (in SI, section 5). After 3000 cycles (6000 isomerization reactions) more than 33% of the original NBD compound was successfully recovered. The exceptional stability of NBD-2Py makes it an intriguing candidate for applications in optical memory storage, bioimaging,[2c] and other fields.

Crystal structures characterization

To gain insights into the exact molecular geometry, crystals of the two norbornadienes have been obtained in the mixture of DCM/Hexane (1:10) and characterised; more crystal data and refinement parameters of NBD-1Py and NBD-2Py are given in Table S1, section 2 in the SI. NBD-1Py crystallized in the monoclinic space group $P2_1/c$ (Z = 4) and its asymmetric unit comprises two molecules of NBD-1Py. There is a disorder between one of the 5 membered rings with a higher occupancy of 0.84. Notably NBD-1Py adopts an unsymmetric conformation, perhaps to optimize molecular

packing. This packing is mainly governed by π···π stacking between NBD-1Py pyrene rings with the shortest distance at 3.508 (2) Å as this is the main interaction in the crystal structure. Other weak interactions such as C-H···π are also perceived with the shortest distance at 2.700 (1) Å (Figure 5a,b). The packing diagram shows zigzag layers of the NBD-1Py molecules down the z-axis and Hirshfeld surface analysis,[26] as seen in Figure 5c. The NBD-2Py crystal structure is a solvate containing hexane. The structure was solved in an orthorhombic space group Pnma (Z = 8) with its asymmetric unit showing half a molecule of NBD-2Py and 0.25 hexane but for a better refinement, the hexane was squeezed using solvent mask in Olex 2 software (Figure 5d).[27] The NBD-2Py hexane solvate is mostly governed by a huge number of π···π interactions between NBD-2Py membered rings with the shortest distance measured at 3.377 (2) Å. There are eight C-H···π also perceived with a minimum distance at 2.720 (3) Å. Figure 5e shows that the hexane solvent is located down [100] running through NBD-2Py channels in the structure with a void volume (solvent accessible surface) of 97.3 Å³ and a unit cell volume percentage of 3.2 % at a probe radius of 1.2 Å, calculated using Mercury software. These channels have an approximate diameter of 4.4 Å as measured by CrystalMaker software. Figure 5f shows the Hirshfeld surface analysis for NBD-2Py. Further analysis indicate that the structure of NBD-2Py can be seen as a network[28] of C-H···π and π ···π interactions where each pyrene connects to three other pyrenes and then also *via* the norbornadiene bridge to form the four-connected **sra**-net[29], see Figure 5g. Deposition Numbers 2302599 for NBD-1Py and 2302598 for NBD-2Py contain the supplementary crystallographic data for this paper. These data are provided free of charge by the joint Cambridge Crystallographic Data Centre and Fachinformationszentrum Karlsruhe at http://www.ccdc.cam.ac.uk/structures.
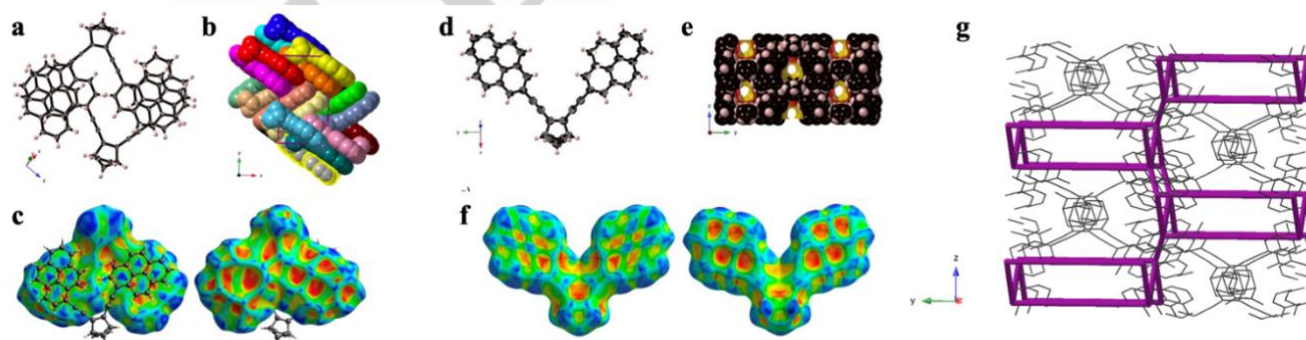

Figure 5: a) Molecular structure of NDB-1Py crystal, with displacement ellipsoids drawn at 50% probability level. b) Packing along z-axis, hydrogen atoms have been omitted and every NDB-1Py molecule coloured individually. c) Hirshfeld surface analysis, showing the shape index mapping. The triangular pattern showing in the left picture is indicative of π···π stacking and the rifts and valleys to the right signals C-H···π interactions. d) The molecular structure of NDB-2Py crystal, with displacement ellipsoids drawn at 50% probability level. e) Packing of NBD-2py along x-axis using a space filling model (vdW radii), emphasizing the channels in which the hexane molecules are located (these cannot be modelled correctly). f) Hirshfeld surface analysis, showing the shape index mapping. The triangular pattern showing in the left picture is indicative of π···π stacking and the rifts and valleys to the right signals C-H···π interactions. g) Network topology analysis of NBD-2Py based on C-H···π and π ···π interactions has each pyrene connecting to three other pyrenes and then also via the norbornadiene bridge to form the four-connected sra-net shown in burgundy. C-C bonds in black and hydrogens have been omitted.

NBD-Py as photoswitchable probes for fluorescent imaging of Alzheimer pathology *in situ*

Confocal and hyperspectral imaging

We evaluated pyrene substituted norbornadienes (NBD-Py) as fluorescent probes targeting Aβ pathology in mouse model tissues.

Moreover, we characterized the switching behaviour of NBD-2Py *in situ*. We used frozen brain sections (12 μm) from 21 month-old female transgenic tgAPPSwe AD mice models. This transgenic model have the human APP gene bearing the Swedish mutation, therefore expressing human Aβ peptide. At 21 months, tgAPPSwe mice are characterized by a high plaque load of large cored plaques in both the prefrontal cortex and hippocampus.[30] The tissue sections were mounted on microscope slides and after fixation and washing they were stained with an ethanol solution of NBD-1Py or NBD-2Py for 2 h (detailed method in SI) yielding clearly stained amiloyd plaques (Figure 6a and SI). To validate the probes target, co-staining of NBD-1Py and NBD-2Py with 6E10 anti β amyloid antibody was also performed. NBD-2Py staining (Figure 6c in green) and NBD-1Py (SI) both demonstrate excellent co-localisation with 6E10 antibody (in red), confirming what is also visually assessed: NBD-1Py and NBD-2Py effectively target and stain Aβ plaques in tgAPPSwe mouse models tissue. Hyperspectral confocal imaging using a Carl Zeiss LSM 880 Airyscan was also performed to assess the spectral properties of NBD-2Py *in situ* (Figure 6a). A 405 nm LED is used to irradiate the sample, and the emission is measured between 420 and 600 nm at 9 nm intervals. The signal was then measured in Fiji and averaged over the whole plaques area. It shows how the fluorescence emission profile of NBD-2Py is not significantly affected by the binding, as seen in Figure 6b. Given that the pyrene moieties are larger than the long conjugated "arms" of the bis(ethynylphenylene) substituted NBD we previously investigated[15], we think it is unlikely that they can bind to the same narrow pocket. For this reason, we chose to investigate further the binding modes with Aβ plaques by performing molecular docking simulations of the norbornadienes with Aβ aggregates.

Molecular Docking Studies

Molecular docking simulations were performed to evaluate the interactions between the NBD-Py and the Aβ plaques. We have chosen solid-state NMR structures (PDB ID: 2LMP) as a model for the Aβ1–40 plaques and (PDB ID: 2MXU) for Aβ1–42 plaques. The obtained binding affinities were slightly higher for Aβ1–40 (2LMP) amyloid, with a docking score of −14.1 kcal/mol for both NBD-Py. Comparatively, for Aβ1–42 (2MXU) structure the docking scores were −12.7 and -12.1 kcal/mol for NBD-1Py and NBD-2Py respectively. Regarding the Aβ1–40 amyloid model, NBD-2Py interacts with the 2LMP structure in a different domain than NBD-1Py (see SI section 6), placing one of its pyrene-arms inside a
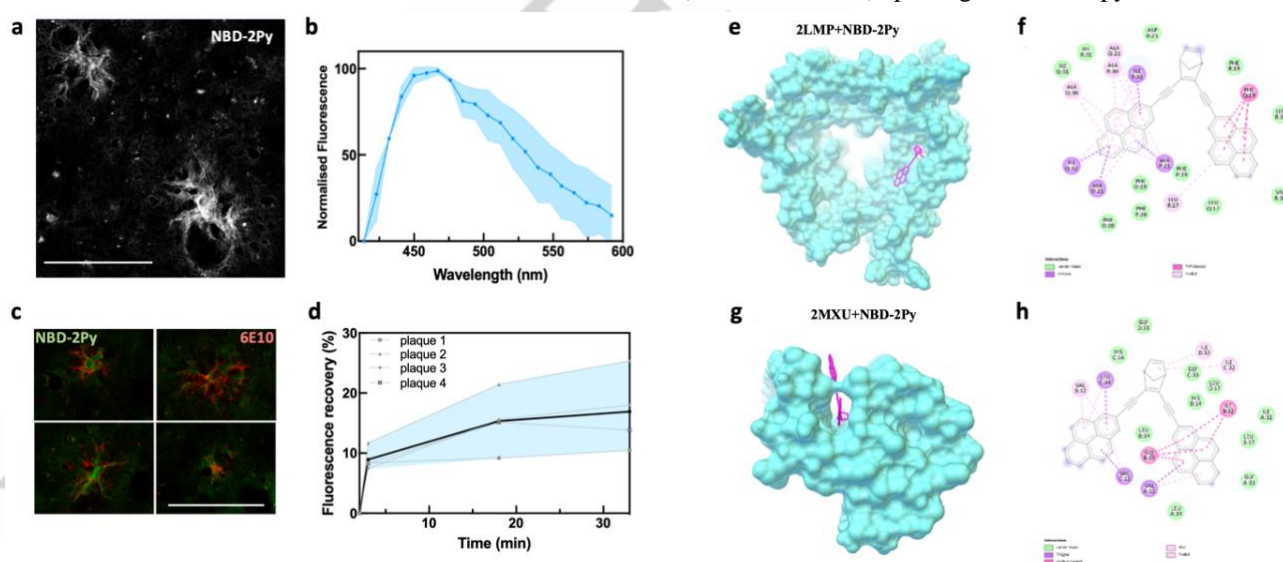

Figure 6: a) Confocal image of Aβ plaques in the cortex of brain sections of a TgSwe mouse model (21 months, female) obtained with NBD-2Py as a fluorescent stain. White bar = 100 μm. In situ measured emission spectra of NBD-2Py (b) when staining the plaques. Measures are an average of the 2 plaques areas, and range is shown as a blue band. c) Confocal images of Aβ plaques in the cortex of brain sections of a TgSwe mouse model (21 months, female). Green is NBD-2Py, red is 6E10 anti amyloid-β antibody; White bar = 100 μm. d) Recovery of NBD-2Py fluorescence signal over time after irradiation of the plaque's areas; 4 plaques are measured, and average and range of recovery are shown as blue lines and area respectively. 17% of recovery in average is observed after around 30 minutes. e), f) Binding modes of NBD-2Py with the Aβ1–40 (PDB ID: 2LMP) amyloid plaque. e) 3D image of the NBD-2Py-2LMP complex (surface of the receptor in light-blue and ligand in magenta). f) 2D interaction diagram of the interactions of NBD-2Py with 2LMP. g) h) Binding modes for NBD-2Py with the Aβ1–42 (PDB ID: 2MXU) amyloid plaque. g) 3D image of NBD-2Py-2MXU ligand-receptor (surface of the receptor in light-blue and ligand in magenta). h) 2D interaction diagram of the interactions of NBD-2Py with 2MXU.

tunnel (Figure 6e and 6f) displaying π - σ interactions with Ala and Ile residues (Figure 6f). The internal cavity of this tunnel exhibits a hydrophobic environment mainly composed of the following nonpolar amino acids: Ala, Leu, Ile and Phe (more detailed images and information of the binding sites are in SI Section 6. The other pyrene arm engages in π···π stacking interactions with the Phe residues at the beginning of the tunnel (Figure 6f). The docking simulations with the Aβ1–42 amyloid model yield similar results for both compounds. Both structures are located on a hydrophobic groove of the 2MXU model (Figure 6g, h for NBD-2Py, Figures for NBD-1Py are in SI Section 6). This groove is mainly composed of Gly, Ala, Leu and Ile amino acid residues, with π-σ and van der Waals interactions occurring between the NBD-Py compounds (more details in SI section 6). Overall, NBD-Py exhibit improved calculated binding to amyloid models compared to the previously investigated bis(ethynylphenylene) substituted NBD, which is mainly achieved thanks to insertion into hydrophobic sites in the plaques where the pyrene moieties are surrounded by non-polar amino acids.

Fluorescence photo-switching *in situ*

We investigated the photo-switching properties of NBD-2Py *in situ*. NBD-2Py stained AD mouse brain sections were irradiated with the confocal microscope light source (405 nm LED). Using the same Zeiss LSM 880 Airyscan microscope, the experiment was set to provide intense light irradiation (405 nm LED at 10% of intensity), followed by image acquisition every 5 seconds (405 nm LED at 1% intensity) for a total of 2 minutes. To capture the whole plaques which are three-dimensional objects, z-scan images were acquired each time, and the maximum intensity projection (obtained using Zeiss in-built processing tool) was used for signal intensity analysis. Subsequently, the intense irradiation was stopped, the imaged area was extended by zooming out (to monitor not irradiated plaques as well and to assess photobleaching), and images were acquired at regular intervals of 15 minutes. The signal from the irradiated plaques increased over time after the intense irradiation was stopped (despite slight photobleaching effects due to image acquisition), indicating back-conversion of QC-2Py to the fluorescent NBD-2Py *in situ*. The fluorescence signal was analysed over 4 different plaques, with different sizes and morphology; the whole plaque´s area was considered, with ROI selected using Fiji threshold (Moments), and the whole spectra extracted for these plaques over the experiment time. The peaks areas were plotted over time, and it can be seen in Figure 6d how they increase significantly: after only around 30 minutes we observe an average of 17% signal recovery, with a maximum of 25% recovery in plaque 2. This is a significant improvement compared to the previously reported bis(ethynylphenylene) substituted NBD (where 24% of signal recovery was achieved after 240 minutes), both because of increased signal recovery and faster recovery times. Nonetheless, almost quantitative recovery with a shorter time span (e.g. ms) is necessary for applications within super-resolution imaging.[3a, 21]

Conclusions

We present the synthesis and characterization of two novel pyrene substituted fluorescent NBD (NBD-1Py and NBD-2Py). Chemical, spectroscopic, and crystal structure characterisation of the two molecular systems are presented and discussed, with support of DFT calculations. It is observed that their spectral properties are significantly different, with NBD-1Py absorption and emission bands red-shifted compared to NBD-2Py. This is rationalised based on their calculated molecular orbitals which show extended conjugation over the whole molecule in NBD-1Py. Effects of the photoisomerization on the emission of NBD-2Py solutions are investigated; photoisomerization of NBD-2Py to QC-2Py induces a decrease in the fluorescence signal. Surprisingly, when exciting QC-2Py at 310 nm we observe higher luminescence than when exciting only NBD at 373 nm, and we hypothesize how this is due to light-induced back isomerization to the excited NBD-2Py which is then the emitting specie. These observations offer an insight into the QC to NBD photoisomerization mechanism which is for the first time observed following an adiabatic pathway followed by emission. Furthermore, NBD-1Py and NBD-2Py efficiently stain Aβ plaques in TgSwe mouse model tissues; their spectroscopic and switching properties are characterised *in situ* and their binding mode is described through docking simulations. Notably, they offer several improvements compared to the previously considered bis(ethynylphenylene) substituted NBD, including improved calculated binding to Aβ aggregates, shorter QC to NBD back-conversion time, higher switching efficiency, and enhanced cyclability. While these are very promising advances, some challenges are still to be addressed. The main future goals will be for example to improve the solubility in aqueous systems and faster QC to NBD isomerization in tissue, which when achieved would unlock applications for advanced imaging of Alzheimer pathology.

Author Contributions

Associated Content:

Supporting information regarding synthesis and chemical characterization, single crystal X-ray diffraction, spectroscopic characterization, theoretical calculations,

physical-chemical characterization, docking simulations and imaging with Aβ plaques are available free of charge.

**Keywords:** Norbornadienes; photochromism; photoswitches; imaging; Alzheimer.

Notes and references

[1] G. Smith, *Journal of Materials Science* **1967**, *2*, 139-152.

[2] aW. Szymanski, J. M. Beierle, H. A. Kistemaker, W. A. Velema, B. L. Feringa, *Chemical reviews* **2013**, *113*, 6114-6178; bA.-A. Nahain, J.-E. Lee, J. H. Jeong, S. Y. Park, *Biomacromolecules* **2013**, *14*, 4082-4090; cZ. Tian, A. D. Li, *Accounts of chemical research* **2013**, *46*, 269-279.

[3] aM. Minoshima, K. Kikuchi, *JBIC Journal of Biological Inorganic Chemistry* **2017**, *22*, 639-652; bE. A. Halabi, D. Pinotsi, P. Rivera-Fuentes, *Nature communications* **2019**, *10*, 1232; cO. Nevskyi, D. Sysoiev, J. Dreier, S. C. Stein, A. Oppermann, F. Lemken, T. Janke, J. Enderlein, I. Testa, T. Huhn, *Small* **2018**, *14*, 1703333.

[4] aW. A. Velema, W. Szymanski, B. L. Feringa, *Journal of the American Chemical Society* **2014**, *136*, 2178-2191; bJ. Broichhagen, J. A. Frank, D. Trauner, *Accounts of chemical research* **2015**, *48*, 1947-1960.

[5] aK. Mutoh, N. Miyashita, K. Arai, J. Abe, *Journal of the American Chemical Society* **2019**, *141*, 5650-5654; bR. Kashihara, M. Morimoto, S. Ito, H. Miyasaka, M. Irie, *Journal of the American Chemical Society* **2017**, *139*, 16498-16501; cS. Helmy, F. A. Leibfarth, S. Oh, J. E. Poelma, C. J. Hawker, J. Read de Alaniz, *Journal of the American Chemical Society* **2014**, *136*, 8169-8172.

[6] M. Olesińska-Mönch, C. Deo, *Chemical Communications* **2023**, *59*, 660-669.

[7] R. Bresolí-Obach, W. A. Massad, A. Abudulimu, L. Lüer, C. Flors, J. G. Luis, L. I. Rosquete, T. A. Grillo, O. Anamimoghadam, G. Bucher, *Dyes and Pigments* **2021**, *186*, 109060.

[8] G. Naren, W. Larsson, C. Benitez-Martin, S. Li, E. Pérez-Inestrosa, B. Albinsson, J. Andréasson, *Chemical Science* **2021**, *12*, 7073-7078.

[9] G. Lv, B. Cui, H. Lan, Y. Wen, A. Sun, T. Yi, *Chemical communications* **2015**, *51*, 125-128.

[10] D. Kim, A. Aktalay, N. Jensen, K. Uno, M. L. Bossi, V. N. Belov, S. W. Hell, *Journal of the American Chemical Society* **2022**, *144*, 14235-14247.

[11] aZ. Wang, A. Roffey, R. Losantos, A. Lennartson, M. Jevric, A. U. Petersen, M. Quant, A. Dreos, X. Wen, D. Sampedro, *Energy & Environmental Science* **2019**, *12*, 187-193; bM. Mansø, A. U. Petersen, Z. Wang, P. Erhart, M. B. Nielsen, K. Moth-Poulsen, *Nature Communications* **2018**, *9*, 1945; cZ. Wang, P. Erhart, T. Li, Z.-Y. Zhang, D. Sampedro, Z. Hu, H. A. Wegner, O. Brummel, J. Libuda, M. B. Nielsen, *Joule* **2021**, *5*, 3116-3136; dZ. Wang, H. Hölzel, K. Moth-Poulsen, *Chemical Society Reviews* **2022**; eF.-Y. Meng, I.-H. Chen, J.-Y. Shen, K.-H. Chang, T.-C. Chou, Y.-A. Chen, Y.-T. Chen, C.-L. Chen, P.-T. Chou, *Nature Communications* **2022**, *13*, 797.

[12] aB. E. Tebikachew, H. B. Li, A. Pirrotta, K. Börjesson, G. C. Solomon, J. Hihath, K. Moth-Poulsen, *The Journal of Physical Chemistry C* **2017**, *121*, 7094-7100; bH. B. Li, B. E. Tebikachew, C. Wiberg, K. Moth-Poulsen, J. Hihath, *Angewandte Chemie* **2020**, *132*, 11738-11743.

[13] A. Dreos, J. Ge, F. Najera, B. E. Tebikachew, E. Perez-Inestrosa, K. Moth-Poulsen, K. Blennow, H. Zetterberg, J. r. Hanrieder, *ACS sensors* **2023**, *8*, 1500-1509.

[14] V. A. Bren, A. D. Dubonosov, V. I. Minkin, V. A. Chernoivanov, *Russian Chemical Reviews* **1991**, *60*, 451-469.

[15] B. E. Tebikachew, F. Edhborg, N. Kann, B. Albinsson, K. Moth-Poulsen, *Physical Chemistry Chemical Physics* **2018**, *20*, 23195-23201.

[16] J. Hardy, D. Allsop, *Trends in pharmacological sciences* **1991**, *12*, 383-388.

[17] M. Fändrich, S. Nyström, K. P. R. Nilsson, A. Böckmann, H. LeVine III, P. Hammarström, *Journal of Internal Medicine* **2018**, *283*, 218-237.

[18] Y. W. Jun, S. W. Cho, J. Jung, Y. Huh, Y. Kim, D. Kim, K. H. Ahn, *ACS central science* **2019**, *5*, 209-217.

[19] G. Bains, A. B. Patel, V. Narayanaswami, *Molecules* **2011**, *16*, 7909-7935.

[20] aJ. Zhang, A. Sandberg, X. Wu, S. Nyström, M. Lindgren, P. Konradsson, P. Hammarström, *Acs Omega* **2017**, *2*, 4693-4704; bJ. Zhang, J. Wang, A. Sandberg, X. Wu, S. Nyström, H. LeVine III, P.

Konradsson, P. Hammarström, B. Durbeej, M. Lindgren, *ChemPhysChem* **2018**, *19*, 3001-3009.

[21] J. Valli, J. Sanderson, *Current Protocols* **2021**, *1*, e224.

[22] A. Lennartson, M. Quant, K. Moth-Poulsen, *Synlett* **2015**, *26*, 1501-1504.

[23] A. G. Crawford, A. D. Dwyer, Z. Liu, A. Steffen, A. Beeby, L.-O. Palsson, D. J. Tozer, T. B. Marder, *Journal of the American Chemical Society* **2011**, *133*, 13349-13362.

[24] W. Alex, P. Lorenz, C. Henkel, T. Clark, A. Hirsch, D. M. Guldi, *Journal of the American Chemical Society* **2021**, *144*, 153-162.

[25] M. Barale, M. Escadeillas, G. Taupier, Y. Molard, C. Orione, E. Caytan, R. Métivier, J. Boixel, *The Journal of Physical Chemistry Letters* **2022**, *13*, 10936-10942.

[26] M. A. Spackman, D. Jayatilaka, *Crystengcomm* **2009**, *11*, 19-32.

[27] O. V. Dolomanov, L. J. Bourhis, R. J. Gildea, J. A. K. Howard, H. Puschmann, *J. Appl. Crystallogr.* **2009**, *42*, 339-341.

[28] aL. Öhrström, *Chem. Eur. J.* **2016**, *22*, 13758-13763; bF. Hoffmann, M. Fröba, in *The Chemistry of Metal-Organic Frameworks: Synthesis, Characterization, and Applications,* (Ed.: S. Kaskel), John Wiley & Sons, **2016**; cO. Delgado-Friedrichs, S. T. Hyde, M. O'Keeffe, O. M. Yaghi, *Structural Chemistry* **2017**, *28*, 39-44.

[29] aM. O'Keeffe, M. A. Peskov, S. Ramsden, O. M. Yaghi, *Acc. Chem. Res.* **2008**, *41*, 1782-1789; bM. O'Keeffe, O. Delgado-Friedrichs, (Ed.: O. K. Reticular Structure Chemistry Resource, M.; Yaghi, O. M.; Ramsden, S.), **2019**.

[30] aO. Philipson, P. Hammarström, K. P. R. Nilsson, E. Portelius, T. Olofsson, M. Ingelsson, B. T. Hyman, K. Blennow, L. Lannfelt, H. Kalimo, *Neurobiology of aging* **2009**, *30*, 1393-1405; bM. Pagnon de la Vega, V. Giedraitis, W. Michno, L. Kilander, G. Güner, M. Zielinski, M. Löwenmark, R. Brundin, T. Danfors, L. Söderberg, *Science translational medicine* **2021**, *13*, eabc6184.

9

Entry for the Table of Contents
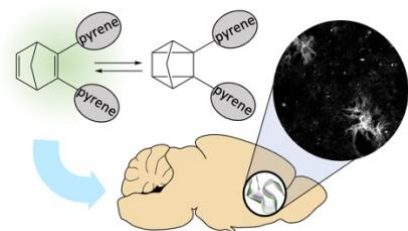
TOC text:

In this study we synthesize and characterise two novel fluorescent norbornadiene derivatives bearing pyrene moieties. In depth spectral and physico-chemical characterisation is presented; moreover, their application as dyes for imaging of amyloid beta aggregates in Alzheimers mice models is investigated, with implications for bioimaging and protein aggregate studies.

Pyrene functionalized norbornadiene-quadricyclane fluorescent photoswitches: characterization of their fluorescence properties and application in imaging of amyloid beta plaques

Supporting information

Shima Ghasemi,[a] Monika Shamsabadi,[a] Axel Olesund,[a] Andreas Erbs Hillers-Bendtsen,[b] Francisco Najera,[c,d] Fredrik Edhborg,[a] Adil S. Aslam,[a] Wera Larsson,[a] Zhihang Wang,[e] Francoise M. Amombo Noa, Rebecca Jane Salthouse,[j] Lars Öhrström,[a] Helen Hölzel,[j] E. Perez-Inestrosa,[c,d] Kurt V. Mikkelsen,[b] Jörg Hanrieder,[f,g] Bo Albinsson,[a] Ambra Dreos,[f,c*] Kasper Moth-Poulsen.[a,h,i,j*]

a. Department of Chemistry and Chemical Engineering, Chalmers University of Technology, 41296 Gothenburg, Sweden
b. Department of Chemistry, University of Copenhagen, Universitetsparken 5, Copenhagen Ø, Denmark
c. Instituto de Investigación Biomédica de Málaga y Plataforma en Nanomedicina-IBIMA Plataforma Bionand, 29590 Malaga, Spain
d. Departamento de Química Orgánica, Facultad de Ciencias, Universidad de Málaga, E-29071 Málaga, Spain.
e. Department of Materials Science and Metallurgy, University of Cambridge, 27 Charles Babbage Rd, Cambridge CB3 0FS, U.K.
f. Department of Psychiatry and Neurochemistry, Sahlgrenska Academy, University of Gothenburg, 43180 Mölndal, Sweden
g. Department of Neurodegenerative Disease, Queen Square Institute of Neurology, University College London, London WC1N 3BG, UK.
h. The Institute of Materials Science of Barcelona, ICMAB-CSIC, Bellaterra, 08193 Barcelona, Spain.
i. Catalan Institution for Research & Advanced Studies, ICREA, Pg. Lluʹıs Companys 23, 08010 Barcelona, Spain.
j. Department of Chemical Engineering, Universitat Politècnica de Catalunya, EEBE, Eduard Maristany 10–14, 08019 Barcelona, Spain

Contents

1.Synthesis and chemical characterization

General procedure:

All reactions were performed under a nitrogen atmosphere using oven-dried glassware. Products were characterized by Proton (^{1}H) and carbon (^{13}C) nuclear magnetic resonance (NMR) using an automated Agilent (Varian) (400 MHz) spectrometer and Bruker (700 MHz). Dry solvents (toluene and tetrahydrofuran) were used from a MBraun MB SPS-800 solvent purification system. Column chromatography for purification was carried out using a Biotage IsoleraTM and preparative TLC plate using silica gel GF 2000 micron. General procedure for the synthesis:
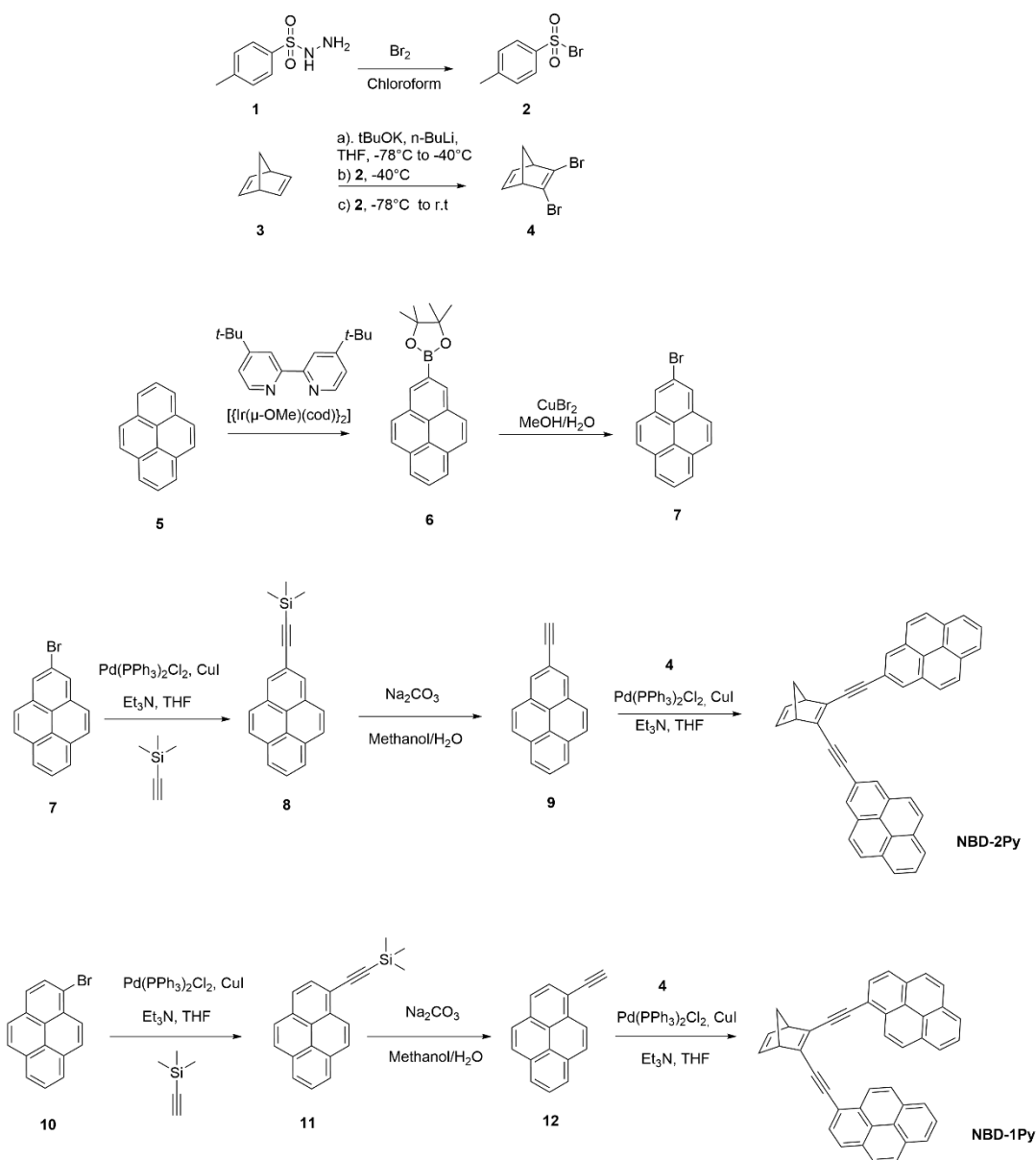
Scheme S1: Synthetic procedure for NBD-1Py and NBD-2Py.

p-**Toluenesulfonyl Bromide (2)**

p-Toluenesulfonyl hydrazide (50 g, 0.27 mol) was dissolved in $CHCl_3$ (500 mL) in a two-neck flask at 0 °C equipped with a dropping funnel. Bromine (27 mL, 0.54 mol) was added dropwise to the mixture using the dropping funnel. (Attention: Added small amounts of ice frequently to keep the temperature inside the reaction media at 0 ºC). When the last portion of bromine was added to the solution, the color of the mixture was still white. Additional bromine was added until a light orange color persisted. After separation of the organic phase from the aqueous phase, the organic phase was washed with sat. aq. $NaHCO_3$ solution (2 x 100 mL) and 1% aq. $Na_2S_2O_3$ solution (2 x 100 mL). The organic phase was dried over Na_2SO_4, filtered, and the solvent was removed to give the product as a white solid (yield: 95%). Data according to literature.

2,3-Dibromonorbornadiene (4)

Potassium *tert*-butoxide (11.2 g, 0.1 mol) was transferred to a three-neck flask equipped with a dropping funnel inside the glove box. After transferring the flask to the fume hood, dry THF (200 mL) was added to the flask by cannula and then the reaction mixture was cooled inside -84 ºC bath. Liquid nitrogen was added constantly to ethyl acetate to keep the temperature at –84 ºC during the reaction. In the next step, norbornadiene (12.2 mL, 0.12 mol) was added to the mixture followed by the dropwise addition of n-BuLi (2.5 M in hexanes, 40 mL, 0.1 mol) over 60 min while the reaction temperature was kept around – 84 ºC. After 15 minutes of keeping the reaction mixture at -84 ºC, the mixture was brought to -41 ºC (acetonitrile, liquid N_2 bath) and stirred for 60 minutes. After one hour, the temperature was decreased to -84 ºC, *p*-toluenesulfonyl bromide **2** (11.7 g, 0.05 mol) was added portion-wise to the reaction mixture under an atmosphere of nitrogen. After 15 min at -84 ºC , the mixture was brought to -41 ºC for 1 h. In the final step, the solution was decreased to -84 ºC and *p*-toluenesulfonyl bromide (11.7 g, 0.05 mol) was added to the mixture. After an additional 15 min at -84 ºC, the reaction mixture was stirred at ambient temperature for 1 hour. Water (50 mL) was added to the reaction mixture for quenching and the organic phase separated from the aqueous. Subsequently, the aqueous phase was extracted with diethyl ether (2 x 50 mL). All the organic phases were combined and dried over $MgSO_4$, and the solvent was evaporated *in vacuo* to give a brown crude residue. The crude compound was dissolved in pentane, washed with DI water and brine, dried over $MgSO_4$, and filtered. After evaporation of the solvent *in vacuo*, the product was purified *via* distillation over a short Vigreux column. At 30-50 ºC and 5×10^{-2} mbar, the first fraction containing mono-bromo-norbornadiene was collected. When the temperature was increased to 90-100 ºC, dibromo-norbornadiene **4** was collected as a main product. The product was stored in the -80 ºC freezer to avoid any possible degradation. (Yield: 16%), ^{1}H NMR (400 MHz, $CDCl_3$) δ [ppm] = 6.88 (m, 1H), 3.62 (m, 1H), 2.45 (dt, 1H), 2.18 (dt, 1H). Data according to literature.

4,4,5,5-Tetramethyl-2-pyren-2-yl-[1, 3, 2]dioxaborolane [2-(Bpin)pyrene] (6)

To a round bottom flask was added pyrene (5 g, 24.7 mmol), [Ir(μ-OMe)(cod)]$_2$ (117 mg, 250 μmol) and 4,4'-di-tert-butyl-2,2'-dipyridine (113 mg, 484 μmol), followed by addition of hexane (200 ml) under N_2 atmosphere. A solution of bis(pinacolato)diboron (5.96 g, 23.5 mmol) in hexane (250 ml) was added dropwise to the suspension during 1 h at 80 ºC. The reaction mixture was stirred overnight at 80 ºC and then filtered through a short plug of

silica using dichloromethane as an eluent. The residue was concentrated under reduced pressure and purified by flash column chromatography (DCM/Hexane, 1:1) to afford **6** (3.5 g, 43%) as a solid. ^{1}H NMR (MHz 400, CDCl$_3$) δ [ppm] = 8.64 (s, 2H), 8.17 (d, J = 7.6 Hz, 2H), 8.11 (d, J = 9.0 Hz, 2H), 8.06 (d, J = 9.0 Hz, 2H), 8.02 (dd, J = 8.1, 7.2 Hz, 1H), 1.47 (s, 12H). Data according to literature.[1]

2-bromopyrene (7)

To a round bottom flask fitted with a condenser, **6** (3.3 g, 10.06 mmol) and CuBr$_2$ (4.94 g, 22 mmol), dissolved in MeOH/H$_2$O (150 ml, 1:1), were added. The mixture was heated at 90 °C for 16 h. The mixture was cooled to room temperature. H$_2$O (250 ml) was added, and a white precipitate was collected by filtration and washed with H$_2$O. Recrystallization from hexane gave **5** (1.4 g, 44.27%) as a white solid. ^{1}H NMR (MHz 400, CDCl$_3$) δ [ppm] = 8.29 (s, 2H), 8.21 (d, J = 7.6 Hz, 2H), 8.11 (d, J = 9.0 Hz, 2H), 8.06 – 8.01 (m, 1H), 7.99 (d, J = 9.0 Hz, 2H). Data according to literature.[1]

Trimethyl(pyren-2-ylethynyl) silane (8)

In an oven-dried two-neck flask, dichlorobis(triphenylphosphine)palladium (II) (190 mg) and copper iodide (70 mg) were added in the mixture of Et$_3$N/THF (2.5:1, 180 mL) and degassed for 1 hour. After the addition of trimethylsilylacetylene (0.8 mL), the reaction was refluxed for 48 hours. After checking the progress of the reaction by TLC, the solvent was removed by rotary evaporation to give the crude as a black residue. The crude product was purified by column chromatography using hexane to give the product as a white solid (43%). ^{1}H NMR (CDCl$_3$, 400 MHz): δ [ppm] = 8.32(s, 2H), 8.20(d, 2H), 8.10(d, 2H), 7.90-8.09(m, 3H), 0.26 (s, 9H). Data according to literature. [2]

2-ethynylpyrene (9)

Compound **8** (125 mg) and sodium carbonate (156 mg) were dissolved in a mixture of methanol/H$_2$O (10:1, 38 mL). The reaction mixture was stirred 30 h. The progress of reaction was monitored by TLC. After completion of the reaction, the aqueous phase was extracted with ethyl acetate. Then the organic layer was washed with brine and dried over Mg$_2$SO$_4$. The solvent was removed under reduced pressure to obtain a beige solid product that was used in subsequent steps without further purification. ^{1}H NMR (CDCl$_3$, 400 MHz): d [ppm]= 8.36(s, 2H), 8.24(d, 2H), 8.09(d, 2H), 7.95-8.12(m, 3H), 3.21(s, 1H). Data according to literature. [2]

(1R,4S)-2,3-bis(pyren-2-ylethynyl) bicyclo[2.2.1]hepta-2,5-diene(NBD-2Py)

A two-neck oven-dried flask was charged with dichlorobis(triphenylphosphine)palladium (II) (14 mg, 0.02 mmol) and copper iodide (3.8 mg, 0.02 mmol) in THF (5 mL). Subsequently, dibromoNBD (124 mg, 0.5 mmol) was added to the reaction mixture and the solution was degassed for 30 min. In the next step, a solution of compound **9** (120 mg, 0.8 mmol) in 2 mL dry THF was added to the mixture and followed by the addition of triethylamine (1 mL, 7.5 mmol). The reaction mixture was stirred at room temperature and poured into water (25 mL). After extraction of the organic phase with dichloromethane (3 x 20 mL), the organic layers were washed with water (3 x 50 mL), and brine (2 x 30 mL), and dried over Na_2SO_4. The solvent was removed under reduced pressure to afford the crude product as an orange solid. The crude product was purified by column chromatography using Hexane/DCM (10:3) to give the final product as an orange solid (35% yield). ^{1}H-NMR (CDCl₃, 700 MHz): δ [ppm] = 8.38 (s, 1H), 8.20 (m, 4H), 8.11(m, 11H), 6.99(s, 2H), 3.95 (dt, 2H), 2.46 (dt, 1H), 2.30 (dt, 1H). ^{13}C-NMR (CDCl₃, 175 MHz): δ [ppm] = 56.27, 71.54, 86.66, 104.24, 121.01, 124.33, 124.45, 125.39, 126.36, 127.02, 127.58, 128.11, 131.14, 131.29, 142.07.

Trimethyl(pyren-1-ylethynyl) silane (11)

In an oven-dried two-neck flask, dichlorobis(triphenylphosphine)palladium (II) (190 mg) and copper iodide (70 mg) were added in the mixture of Et₃N/THF (2.5:1, 180mL) and degassed for 1 hour. After the addition of trimethylsilylacetylene (0.8 mL), the reaction was refluxed for 48 hours. After checking the progress of the reaction by TLC, the solvent was removed by rotary evaporation to give the crude product as a black residue, which was purified by column chromatography using hexane to yield the title compound as a white solid (43%). ^{1}H NMR (CDCl₃, 400 MHz): δ [ppm] = 8.57 (d, 1H), 8.24-8.01 (m, 8H), 0.40 (s, 9H). Data according to literature. [2]

1-ethynylpyrene (12)

Compound **9** (125 mg) and sodium carbonate (156 mg) were dissolved in a mixture of methanol/H₂O (10:1, 38 mL). The reaction mixture was stirred for 30 h. The progress of reaction was monitored by TLC, and the aqueous phase was extracted with ethyl acetate. Then the organic layer was washed with brine and dried over with Mg₂SO₄. The solvent was removed under reduced pressure to obtain a beige solid product that was used in subsequent steps without further purification. ^{1}H NMR (CDCl₃, 400 MHz): δ [ppm]= 8.60 (d, 1H), 8.25-8.02 (m, 8H), 3.63 (s, 1H). Data according to literature. [2]

(1R,4S)-2,3-bis(pyren-1-ylethynyl) bicyclo[2.2.1]hepta-2,5-diene (NBD-1Py)

A two-neck oven-dried flask was charged with dichlorobis(triphenylphosphine)palladium (II) (14 mg, 0.02 mmol) and copper iodide (3.8 mg, 0.02 mmol) in THF (5 mL). Subsequently, dibromoNBD (124 mg, 0.5 mmol) was added to the reaction mixture and the solution was degassed for 30 min. In the next step, a solution of compound **10** (120 mg, 0.8 mmol) in 2 mL dry THF was added to the mixture and followed by addition triethylamine (1 mL, 7.5 mmol). The reaction mixture was stirred at room temperature and poured into water (25 mL). After extraction of the organic phase with dichloromethane (3 x 20 mL), the organic layers were washed with water (3 x 50 mL),

and brine (2 x 30 mL), and dried over Na$_2$SO$_4$. The solvent was removed under reduced pressure to afford the crude residue as a yellow solid. The crude product was purified by column chromatography using hexane/DCM (10:3) to give the final product as a yellow solid (45% yield). ^{1}H-NMR (CDCl$_3$, 700 MHz): δ (ppm) = 8.38 (s, 1H), 8.82 (d, 2H), 8.25 (m, 12H), 8.00(m, 4H), 7.05(s, 2H), 4.05 (dt, 2H), 2.55 (dt, 1H), 2.36 (dt, 1H). ^{13}C-NMR (CDCl$_3$, 175 MHz): δ [ppm] = 56.23, 71.51, 92.47, 103.23, 118.15, 124.35, 124.58, 125.58, 125.65, 125.90, 126.23, 127.30, 128.26, 128.58, 131.11, 131.29, 131.43, 131.68, 142.13.

NMR spectra
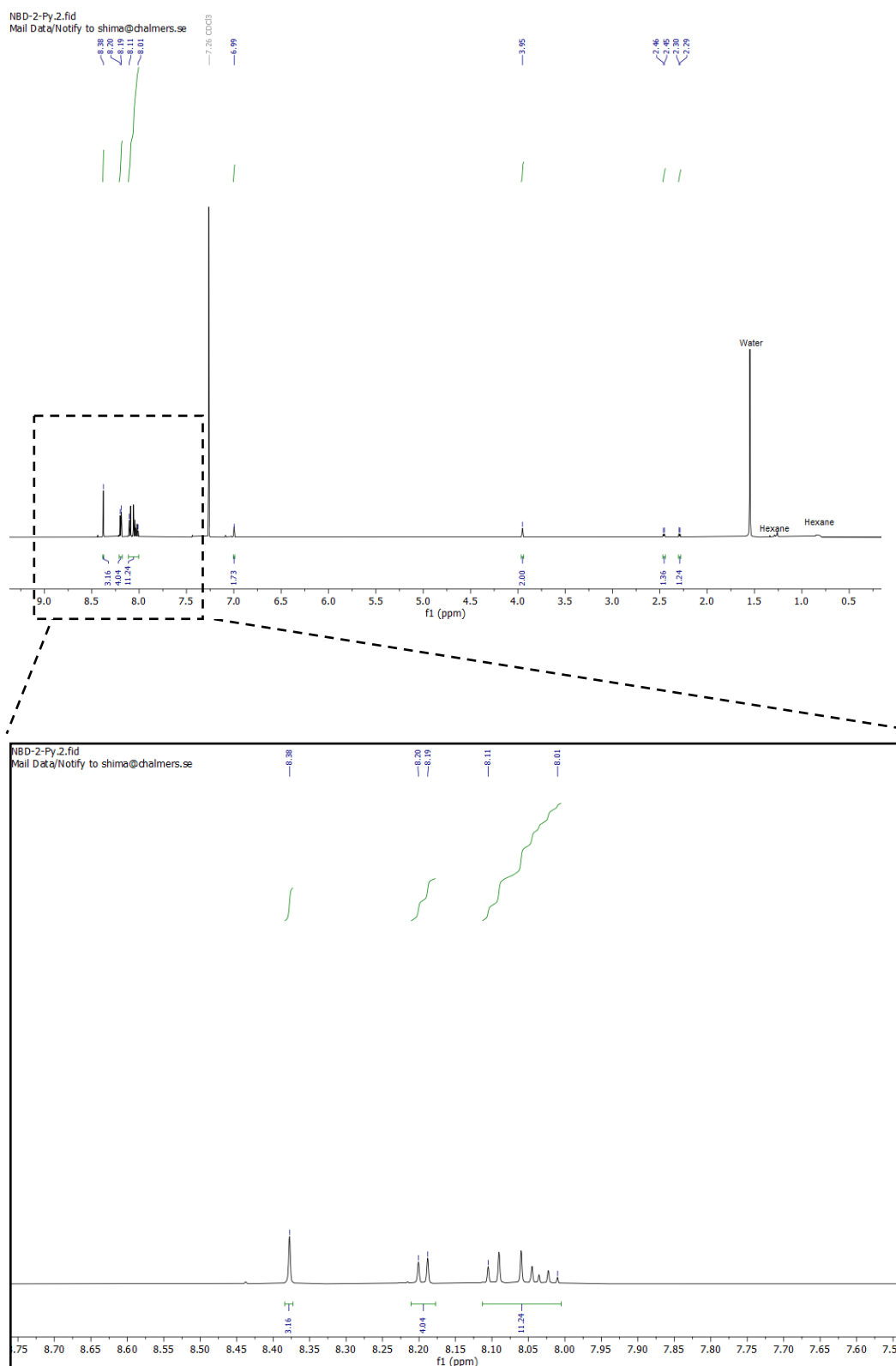
Figure S1: ^{1}H-NMR spectrum of NBD-2Py.
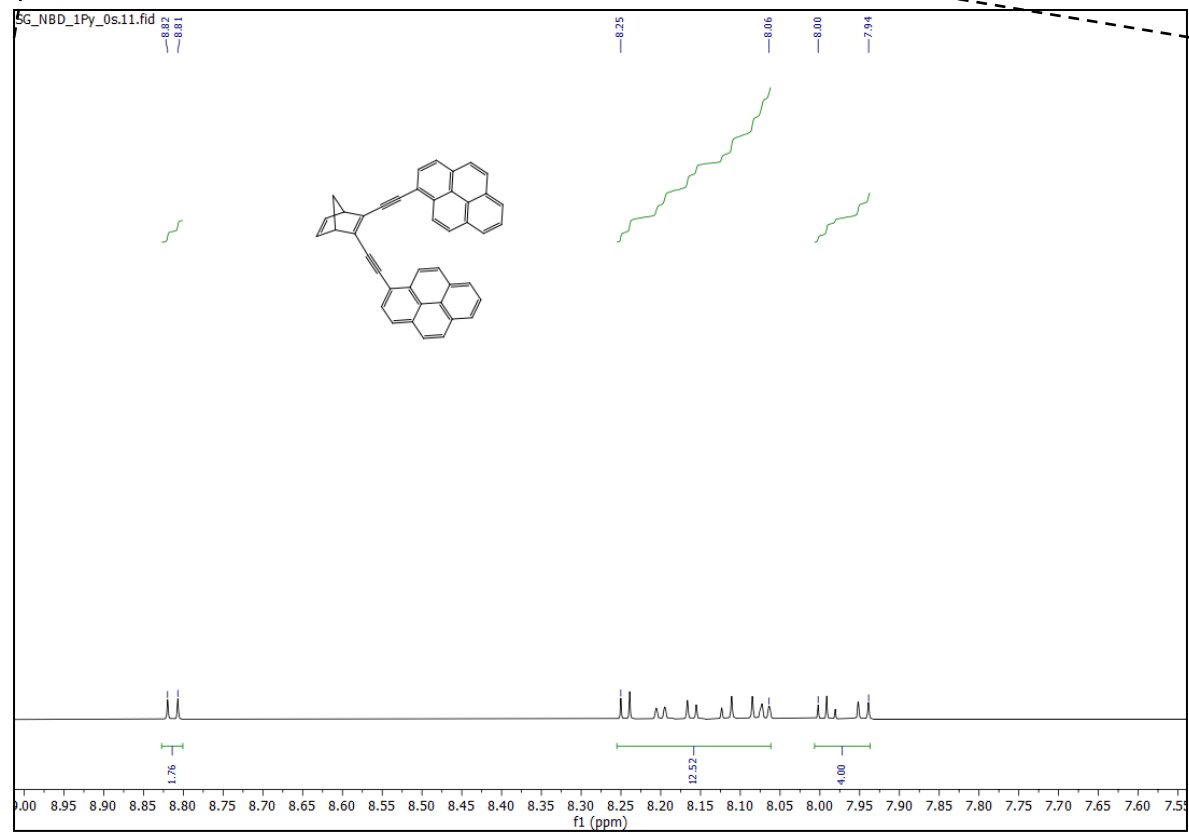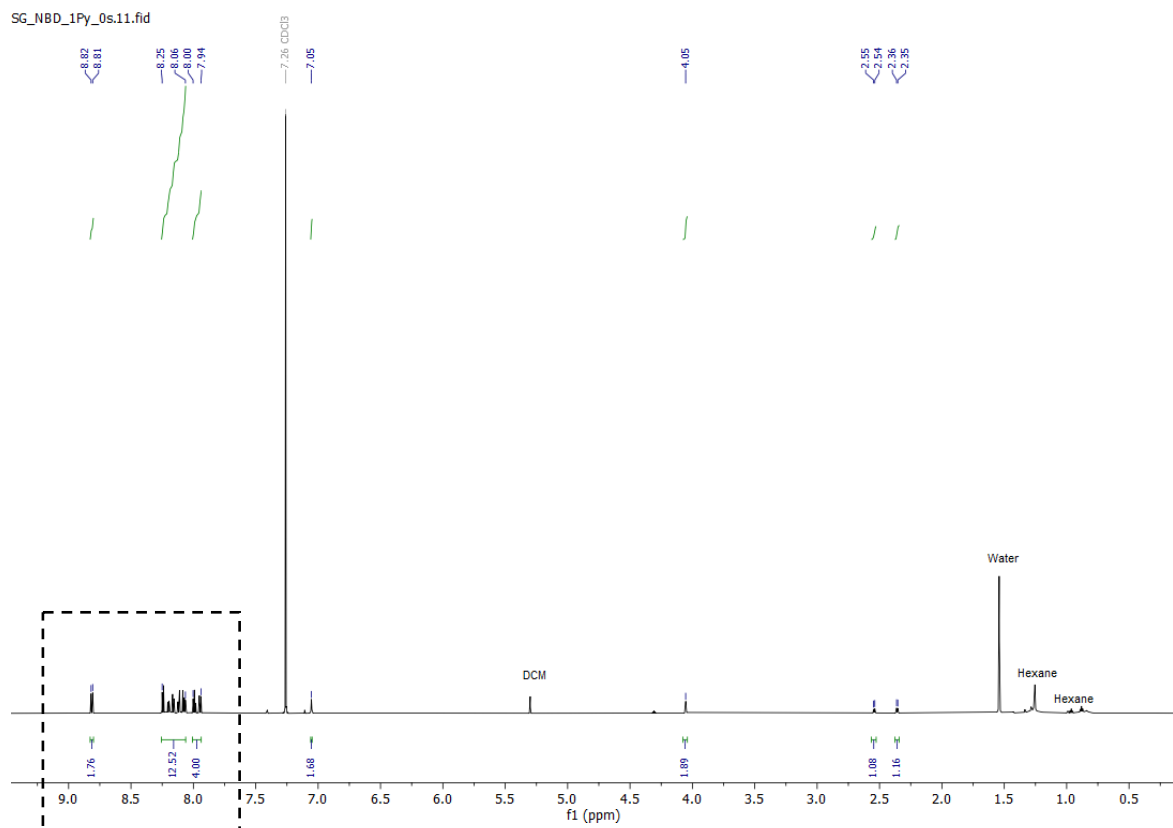
Figure S2: ^{1}H-NMR spectrum of NBD-1Py.
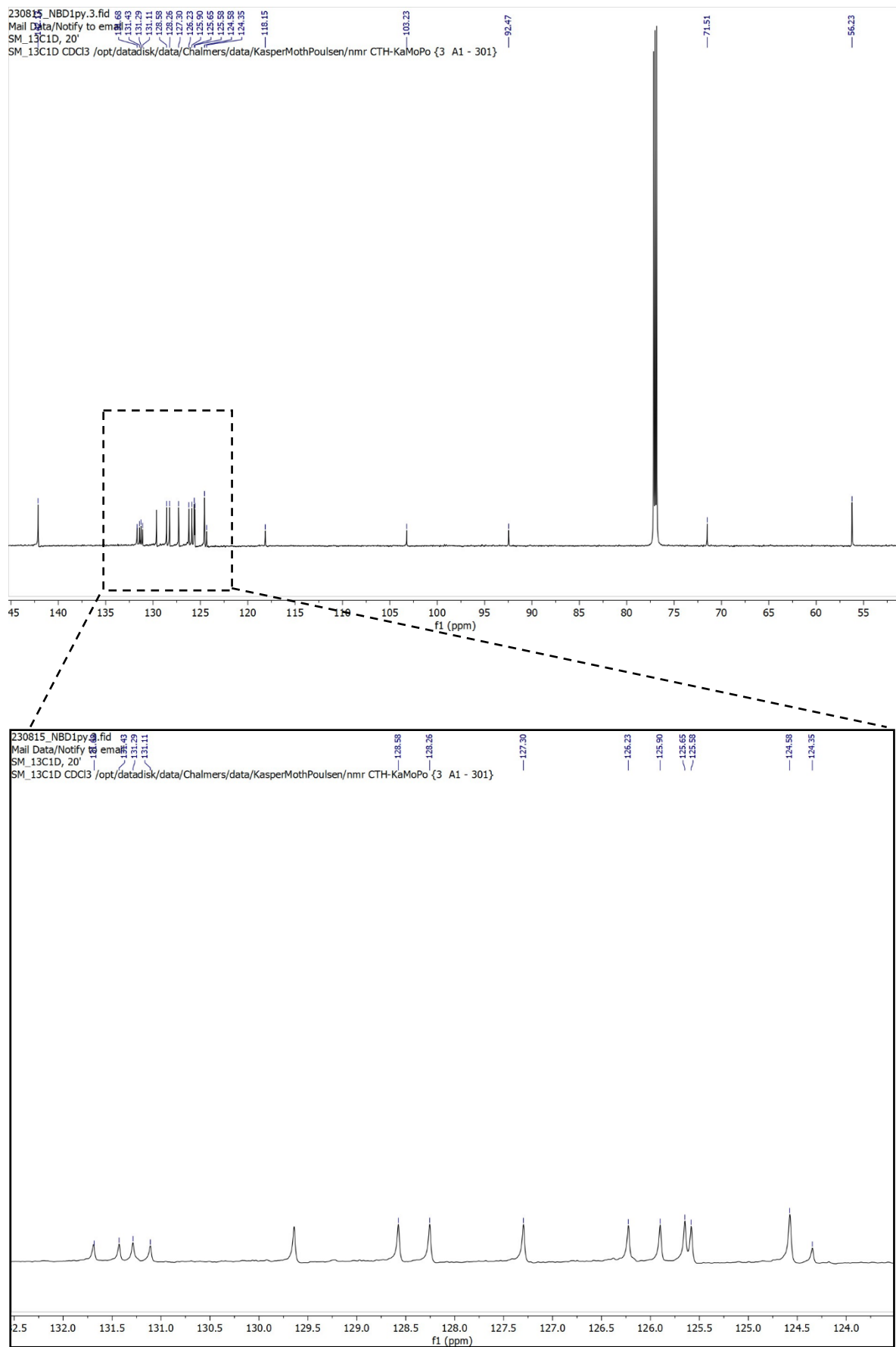
Figure S3: ^{13}C-NMR spectrum of NBD-1Py.
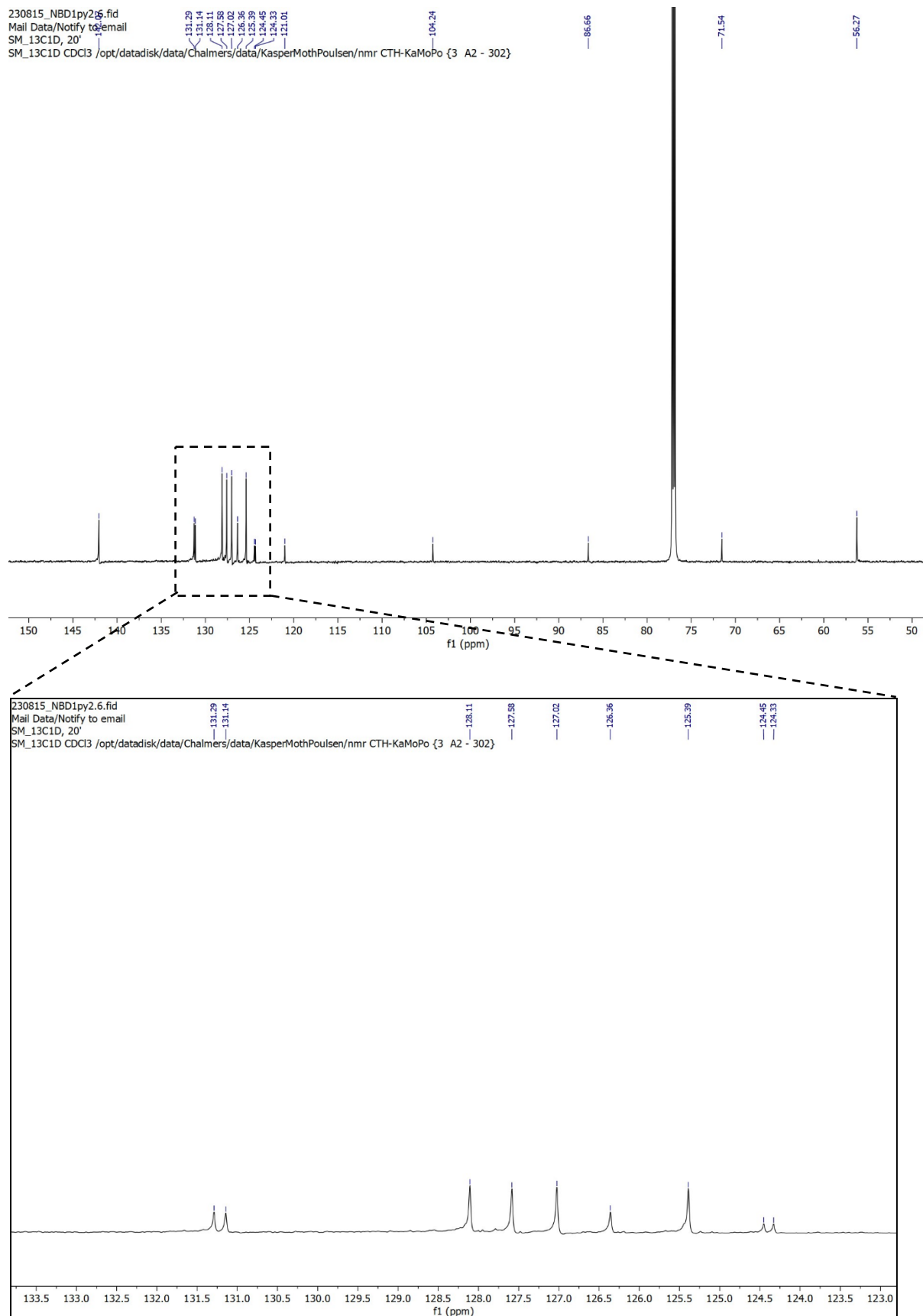
Figure S4: ^{13}C-NMR spectrum of NBD-2Py.
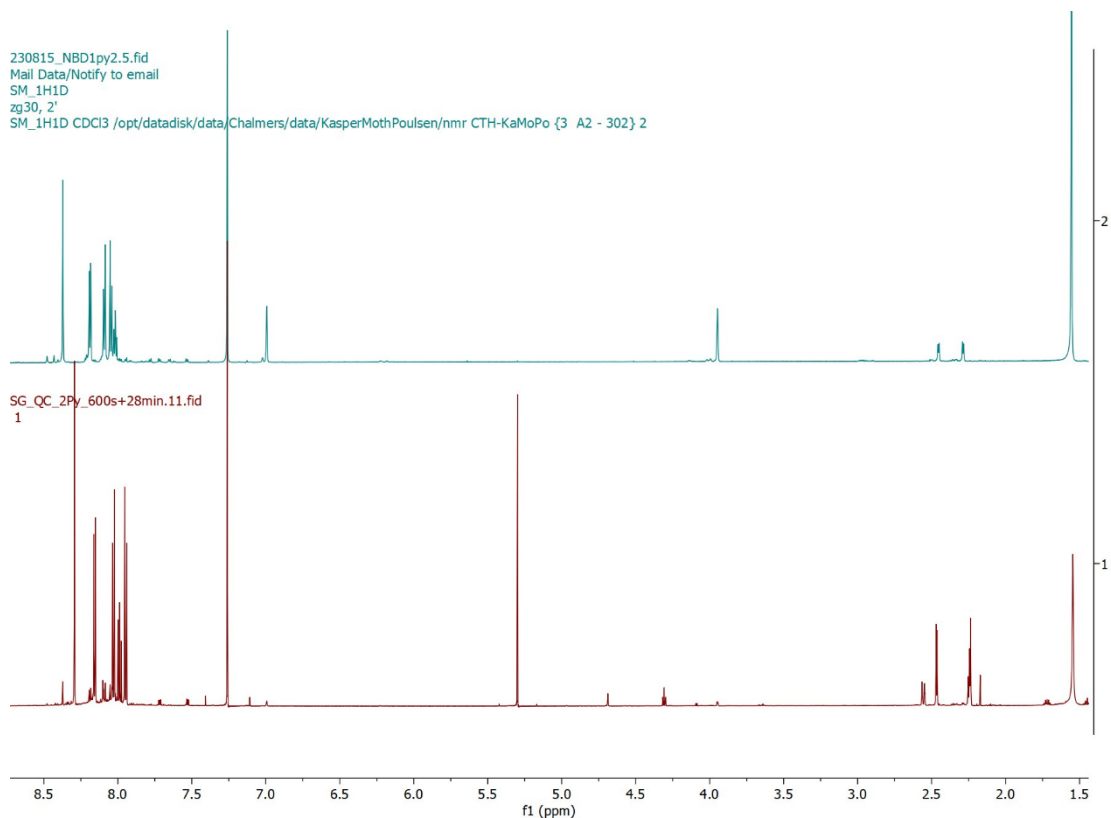
Figure S5: Conversion of NBD-2Py to QC-2Py.
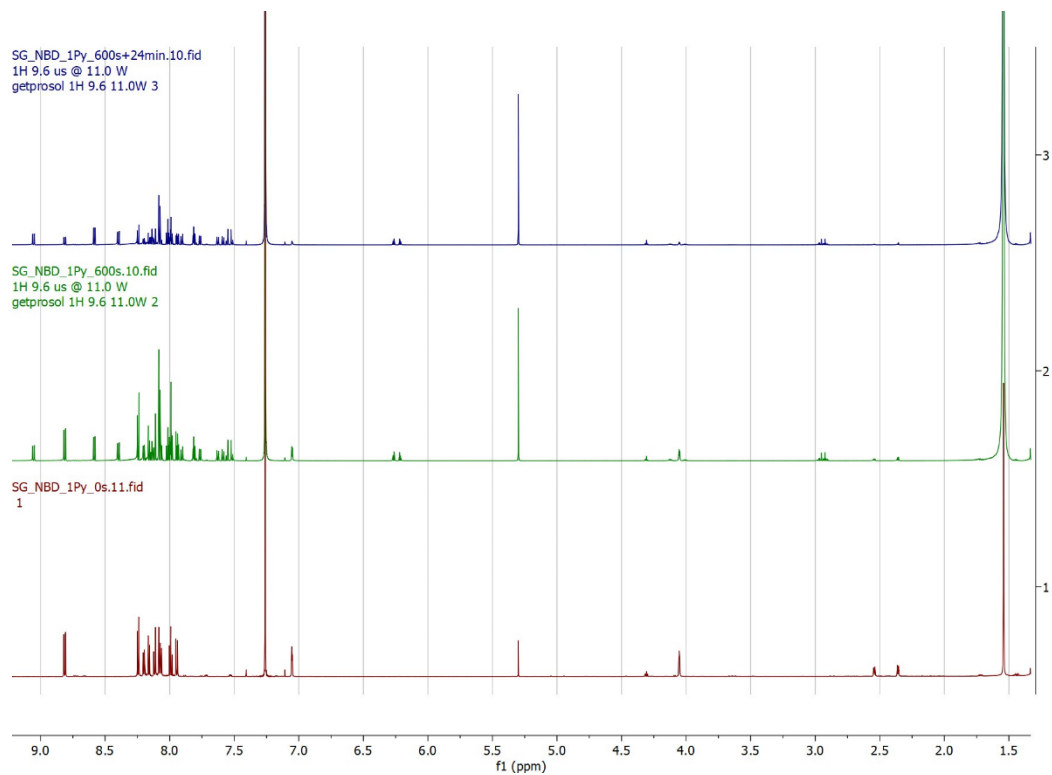
Figure S6: Degradation of NBD-1Py upon irradiation over time.

2. Single crystal X-ray diffraction

Table S1. Experimental details.

	NBD-1Py	NBD-2Py
Crystal data		
Chemical formula	$2(C_{43}H_{24})$	$C_{21.5}H_{12} \cdot 0.25(C_6H_{14})$
M_r	1081.24	291.85
Crystal system, space group	Monoclinic, $P2_1/c$	Orthorhombic, $Pnma$
Temperature (K)	100	122
a, b, c (Å)	10.2460 (1), 18.1151 (2), 29.8581 (3)	10.8946 (6), 24.7697 (18), 11.3593 (6)
β (°)	93.670 (1)	
V (Å^3)	5530.52 (10)	3065.4 (3)
Z	4	8
Radiation type	Cu $K\alpha$	Cu $K\alpha$
μ (mm^{-1})	0.56	0.54
Crystal size (mm)	$0.10 \times 0.03 \times 0.02$	$0.07 \times 0.03 \times 0.03$
Data collection		
Diffractometer	XtaLAB Synergy R, HyPix	XtaLAB Synergy R, HyPix
T_{min}, T_{max}	0.927, 1.000	0.957, 1.000
No. of measured, independent and observed [$I > 2\sigma(I)$] reflections	51705, 10890, 8677	15621, 3141, 1914
R_{int}	0.038	0.048
$(\sin \theta/\lambda)_{max}$ (Å^{-1})	0.628	0.629
Refinement		
$R[F^2 > 2\sigma(F^2)]$, $wR(F^2)$, S	0.049, 0.136, 1.04	0.078, 0.271, 1.06
No. of reflections	10890	3141
No. of parameters	821	196
No. of restraints	134	3
H-atom treatment	H atoms treated by a mixture of independent and constrained refinement	H-atom parameters constrained
$\Delta\rangle_{max}$, $\Delta\rangle_{min}$ (e Å^{-3})	0.68, -0.51	0.50, -0.25
CCDC No	2302599	2302598

Computer programs: olex2.solve 1.5-alpha (Bourhis *et al.*, 2015), *SHELXL* 2018/3 (Sheldrick, 2015), Olex2 1.5-alpha (Dolomanov *et al.*, 2009).

Absorption correction was performed using CrysAlis PRO 1.171.41.119a (Rigaku Oxford Diffraction, 2021) Numerical absorption correction based on gaussian integration over a multifaceted crystal model and empirical absorption correction using spherical harmonics, implemented in SCALE3 ABSPACK scaling algorithm. The crystallographic data can be obtained free of charge from the Cambridge Crystallographic Data Centre, via www.ccdc.cam.ac.uk/conts/retrieving.html.

3. Spectroscopic characterization

Absorption spectroscopy and kinetics experiments were performed by a Cary 50, Cary 100 or Cary 4000 UV-vis spectrophotometer provided with a water heating system. Emission spectra were recorded on a Horiba Jobin Yvon Fluorolog FL3-22. Fluorescence lifetimes were measured by time correlated single photon counting (TCSPC) using an Edinburgh Instruments LifeSpec II, equipped with an MCP-PMT detector. The excitation source in TCSPC was a 405 nm (NBD-1Py) or 377 nm (NBD-2Py) laser diode from PicoQuant. The fluorescence quantum yield, Φ_f, was measured using a previously published method [3] and calculated according to equation 1.

$$\Phi_f = \Phi_{f,ref} \frac{I_s(1 - 10^{-A_r})\eta_s^2}{I_{ref}(1 - 10^{-A_s})\eta_{ref}^2} \tag{1}$$

where $\Phi_{f,ref}$ is the fluorescence quantum yield of the reference, I_s and I_{ref} is the area integrated emission spectrum of the sample and the reference, respectively, A_s and A_r is the absorbance of the sample and the reference at the excitation wavelength, respectively, and η_s and η_{ref} is the solvent refractive index at the emission wavelength for the sample and the reference, respectively. Photoswitching experiments were carried out using Thorlabs LED lamps 340 nm (M340L4), 365 nm (M365F1) and 405 nm (M405LP1). Photoisomerization quantum yields were measured according to a published literature method using a concentrated sample (absorbance > 2) at room temperature.

Coumarin 102 (also known as Coumarin 480) dissolved in ethanol ($\Phi_{f,ref} = 0.798$) was used as reference for both NBD-1Py and NBD-2Py. The use of the same reference for both compounds enables a direct comparison of the measured fluorescence quantum yields. For NDB1-Py, also Coumarin 6 dissolved in ethanol ($\Phi_{f,ref} = 0.908$) was used as a second reference because its absorption spectrum better matches that of NBD1-Py. The measured fluorescence quantum yield of NBD-1Py was the same for both references, within experimental error. Both NBD-1Py and NBD-2Py were dissolve in toluene and 10 mm cuvettes were used for the quantum yield measurements. The emission spectrum of the sample and reference was measured using at least three different excitation wavelengths in the range of 400-465 nm for NBD-1Py and 368-413 nm for NBD-2Py. The reported quantum yield

is the average quantum yield measured at these excitation wavelengths. The absorbance of the sample and the reference was adjusted to be below 0.07 in a 10 mm cuvette to minimize inner filter effects (see Figure S4). For NBD-2Py, stirring was used in the cuvette when recording the emission spectrum and when measuring the emission lifetime to reduce the effect of photoisomerization during the experiment. The absorbance of all samples was measured before and after each experiment to verify that no significant isomerization or degradation had occurred.
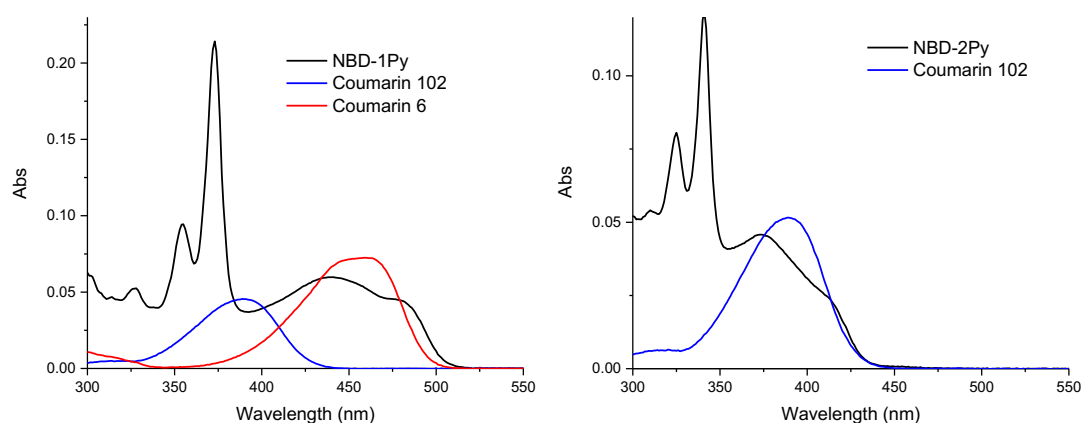
Figure S7. Absorption spectra of NBD-1Py and NBD-2Py together with the absorption spectra of the respective references used for measuring fluorescence quantum yield. All spectra measured with 10 mm optical pathlength.
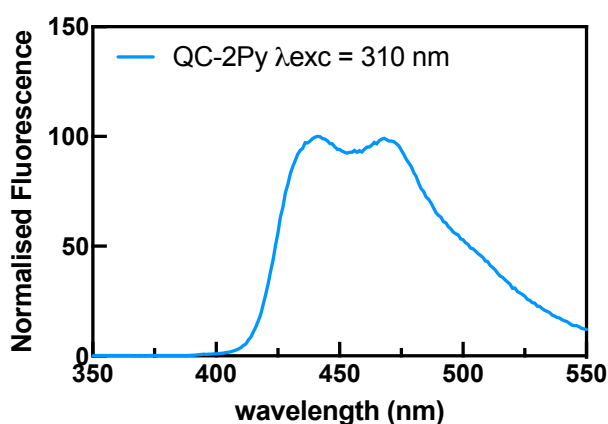
Figure S8: Emission measured after photoisomerization of NBD to QC, at λexc=310 nm.

4. Theoretical calculations

To complement the observed spectroscopic properties, we performed quantum chemical calculations on NBD-1PY, QC-1PY, NBD-2PY, and QC-2PY. Initially, we performed a systematic conformational search using RDkit[4] and subsequent geometry optimization using GFN2-xTB[5] to obtain the lowest energy conformer of each

compound. These initial calculations follow the workflow of previous screening studies on NBD systems[6, 7]. Subsequently, we optimized the geometries of NBD-1PY, QC-1PY, NBD-2PY, and QC-2PY at the CAM-B3LYP/def2-SVPD level of theory[8, 9] with empirical dispersion D3 included using the GFN2-xTB structures as input. We then performed harmonic frequency calculations on the converged structures.

To simulate absorption, we first calculated the lowest 50 vertical excitation energies and associated oscillator strengths using time-dependent density functional theory (TD-DFT) at the CAM-B3LYP/def2-SVPD level of theory. Using these results, UV-Vis absorption spectra were simulated by convolution with Lorentzian functions using a broadening of 0.4 eV. In addition to that, we also determined natural transition orbitals (NTOs) for the lowest excited states with an oscillator strength of at least 0.01. All density functional theory calculations were performed in Orca 5[10] using the large DEFGRID3 integration grid.

From the thermochemical data obtained in the frequency calculations, we can determine the energy difference between the NBD and QC forms, ΔE_R. This is done using the determined Gibbs Free energies at 298.15 K and the results are shown in Table S2.

Table S2: Predicted energy differences between NBD and QC.

System	ΔE_R / kJ mol^{-1}
NBD/QC 1	79.07
NBD/QC 2	69.83

We see that the energy difference between the NBD/QC forms of each system is moderately large. However, given the large system size and associated molecular weight, the energy difference is only modest. We were unfortunately not able to converge a transition state for the thermal conversion between NBD and QC for any of the studied systems, which is why we cannot reliably estimate the thermal reaction barrier.

Turning the attention to the optical properties, the NTOs and excitation data are shown in Figures S9-26 and in Table S3.

Table S3: Wavelength of absorption (oscillator strength) for the five lowest singlet excited states for each compound. The NTOs of those highlighted in bold were also computed.

System	S_1	S_2	S_3	S_4	S_5
NBD 1	**462.9 nm (0.25)**	**376.3 nm (0.64)**	**367.6 nm (0.30)**	343.0 nm (0.01)	337.2 nm (0.00)
QC 1	**360.3 nm (0.32)**	**343.0 nm (0.90)**	324.3 (0.00)	323.6 nm (0.00)	294.1 nm (0.04)
NBD 2	**403.5 nm (0.69)**	346.6 nm (0.00)	345.5 nm (0.00)	**315.3 nm (0.28)**	**313.9 nm (0.16)**
QC 2	331.3 nm (0.00)	329.1 nm (0.00)	323.2 nm (0.00)	**311.1 nm (0.17)**	294.3 nm (0.00)

NBD 1-Py

S_1 particle:
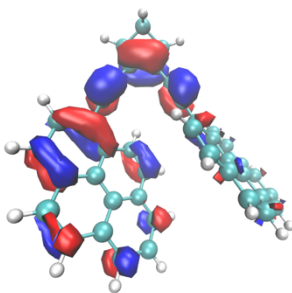
Figure S9: Particle orbital involved in the S_0-S_1 transition in NBD-1Py.

S_1 hole:
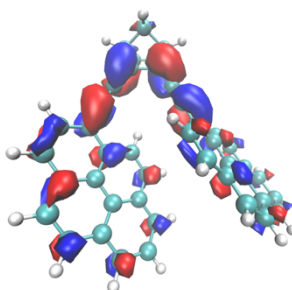
Figure S10: Hole orbital involved in the S_0-S_1 transition in NBD-1Py.

S$_2$ particle:
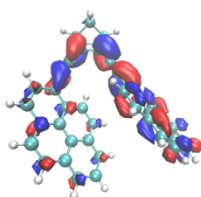
Figure S11: Particle orbital involved in the S$_0$-S$_2$ transition in NBD-1Py.

S$_2$ hole:
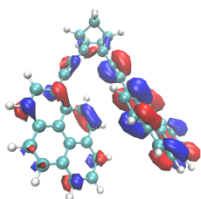
Figure S12: Hole orbital involved in the S$_0$-S$_2$ transition in NBD-1 Py.

S$_3$ particle:
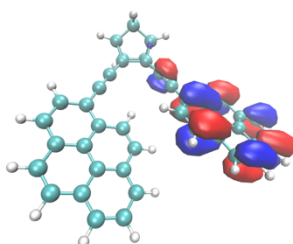
Figure S13: Particle orbital involved in the S$_0$-S$_3$ transition in NBD-1 Py.

S₃ hole:
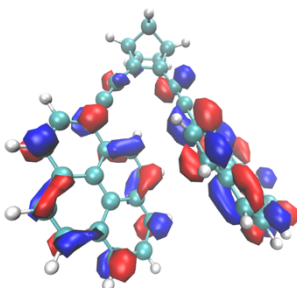
Figure S14: Hole orbital involved in the S_0-S_3 transition in NBD-1Py.

QC 1-Py

S₁ particle:
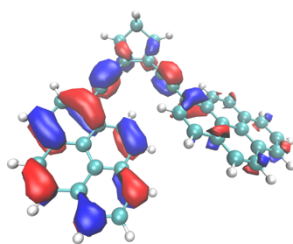
Figure S15: Particle orbital involved in the S_0-S_1 transition in QC-1Py.

S₁ hole:
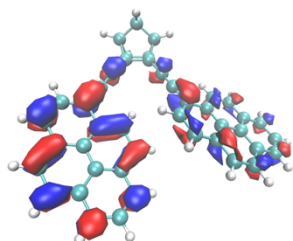
Figure S16: Hole orbital involved in the S_0-S_1 transition in QC-1Py.

S₂ particle:
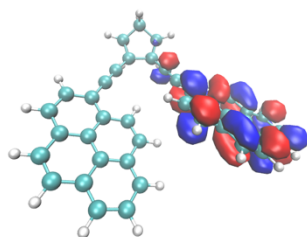
Figure S17: Particle orbital involved in the S_0-S_2 transition in QC-1Py.

S₂ hole:
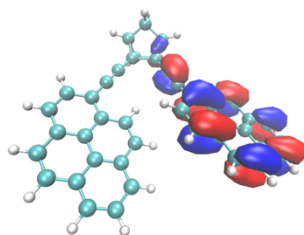
FigureS18: Hole orbital involved in the S_0-S_2 transition in QC-1Py.

NBD 2-py

S₁ particle:
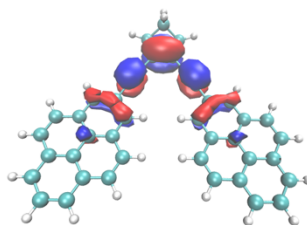
Figure S19: Particle orbital involved in the S_0-S_1 transition in NBD-2Py.

S$_1$ hole:
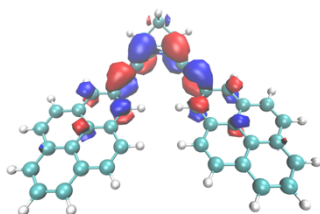
Figure S20: Hole orbital involved in the S$_0$-S$_1$ transition in NBD-2Py.

S$_4$ particle:
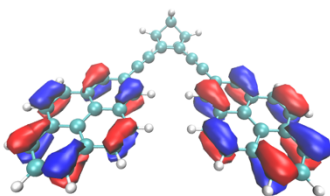
Figure S21: Particle orbital involved in the S$_0$-S$_4$ transition in NBD-2Py.

S$_4$ hole:
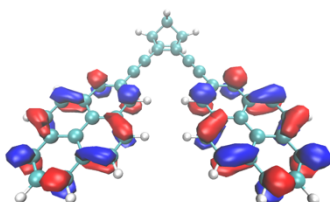
Figure S22: Hole orbital involved in the S$_0$-S$_4$ transition in NBD-2Py.

S$_5$ particle:
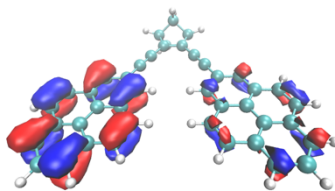
Figure S23: Particle orbital involved in the S$_0$-S$_5$ transition in NBD-2Py.

S$_5$ hole:
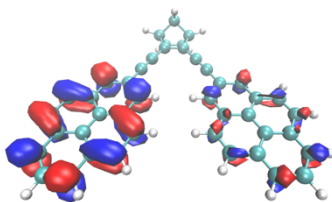
Figure S24: Hole orbital involved in the S$_0$-S$_5$ transition in NBD-2Py.

QC 2-Py

S$_4$ particle:
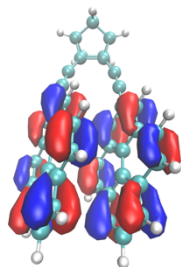
Figure S25: Particle orbital involved in the S$_0$-S$_4$ transition in QC-2Py.

S₄ hole:
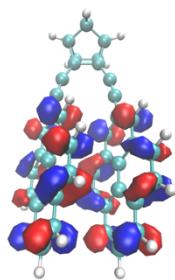
Figure S26: Hole orbital involved in the S_0-S_4 transition in QC-2Py.

5. Photoisomerization quantum yield, cycling, and kinetics of QC to NBD thermal isomerization
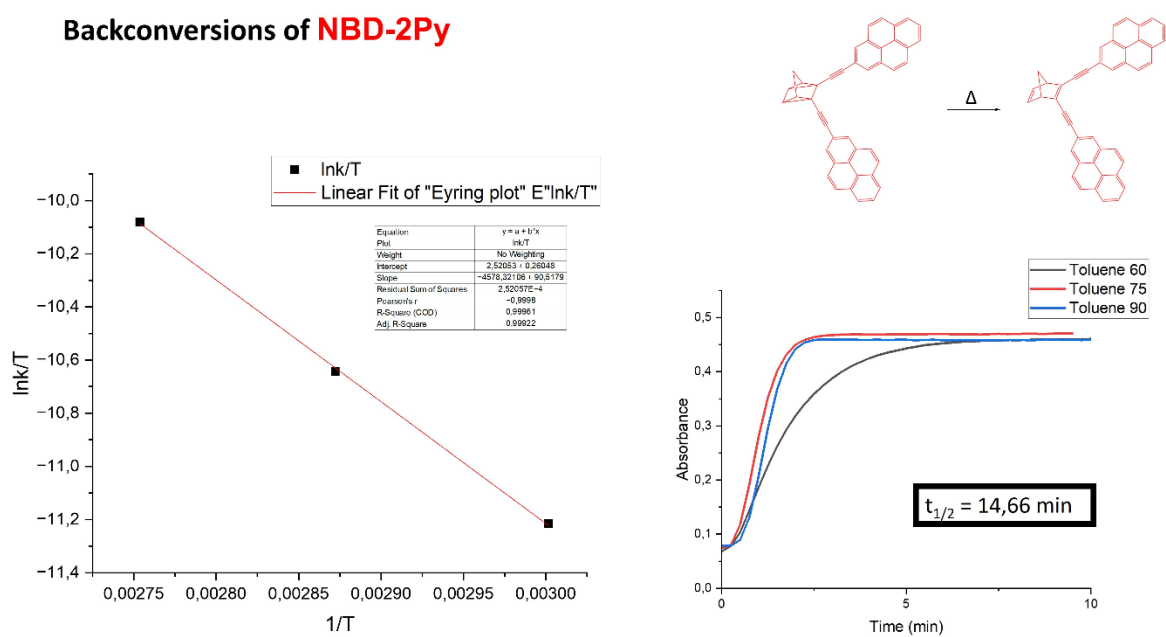
Figure S27: Measures of the half-life of thermal isomerization of QC-2Py to NBD-2Py.
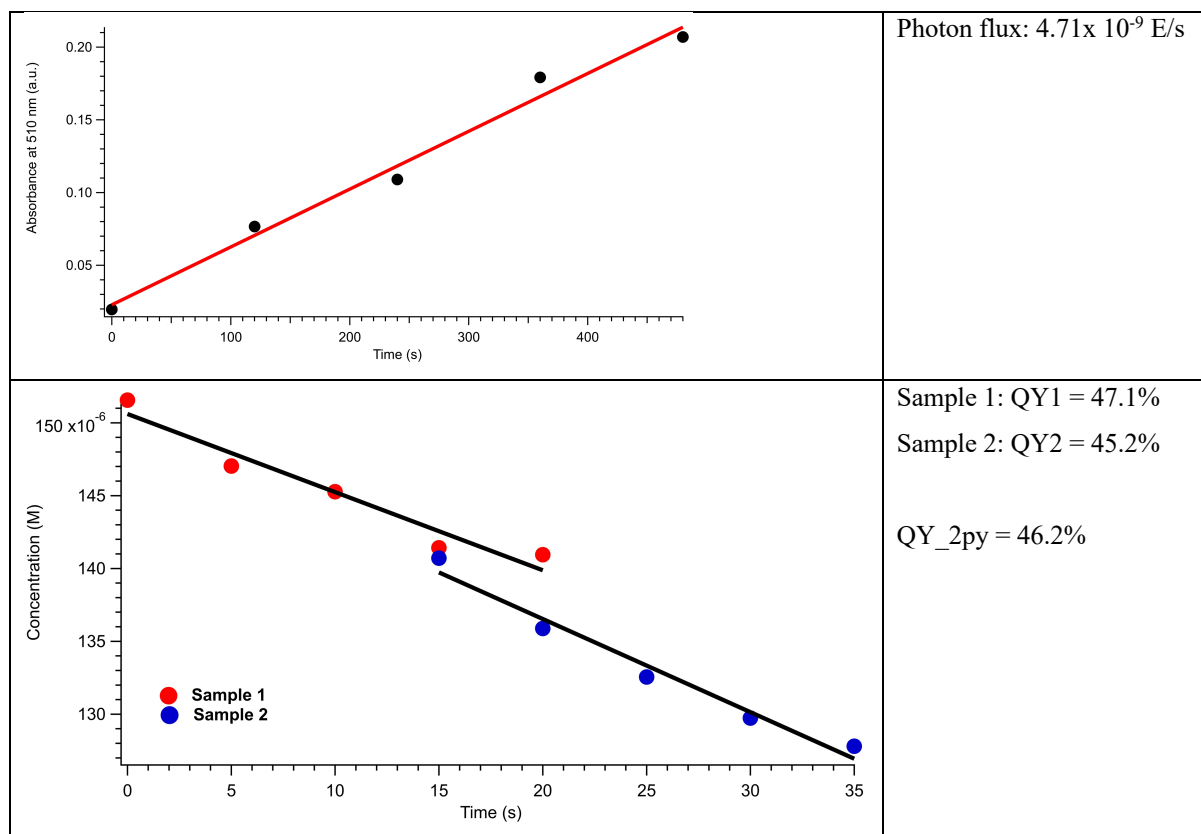
Figure S28: Measures of the photoisomerization quantum yield for NBD-2Py to QC-2Py isomerization.
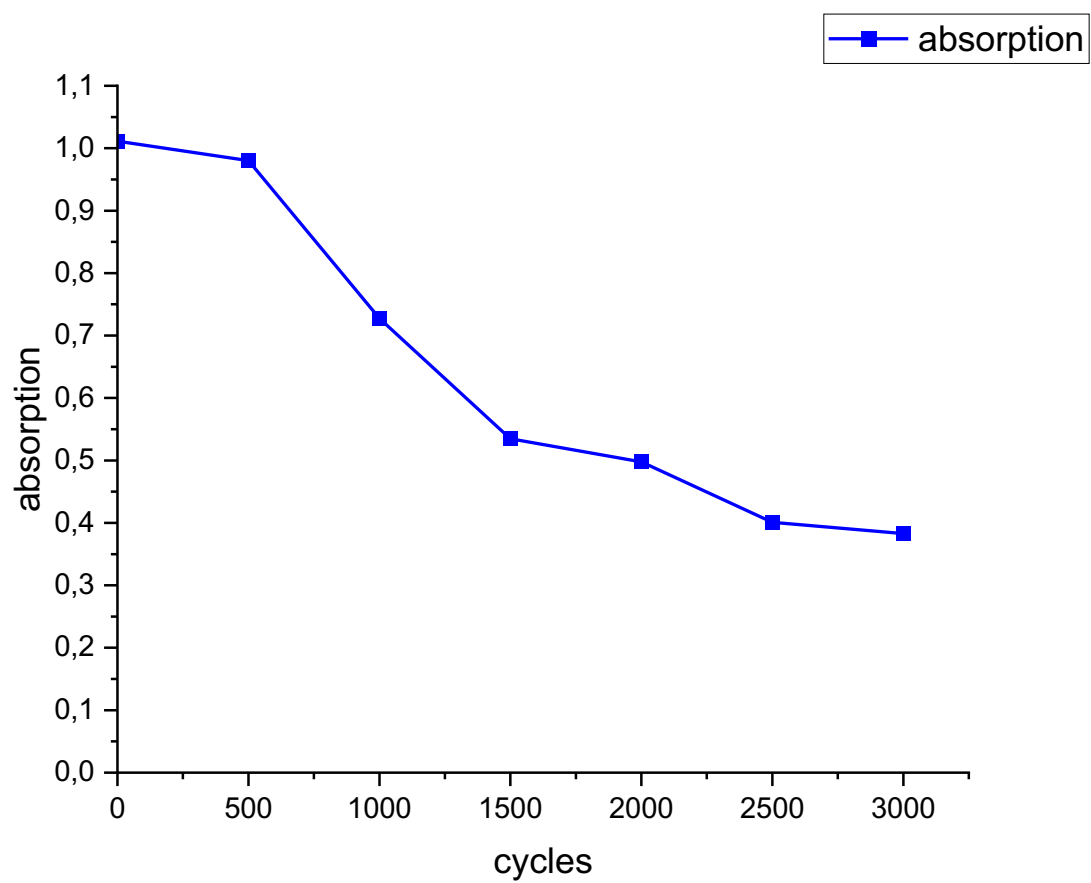
Figure S29: 3000 cycles of NBD→QC→NBD conversion of the NBD-2Py/QC-2Py system, followed by measurement of absorption at 392nm.

6. Docking simulations

The molecular docking simulation was performed with the free software AutoDock Vina v1.1.2[11]. The structures of amyloid aggregates were obtained from RCSB Protein Data Bank (PDB ID: 2LMP for the Aβ_{40} and PDB ID: 2MXU for the Ab$_{42}$).[14] The docking simulations were carried out with a box centered on the Aβ oligomers and an adequate grid to contain the entire receptor. The number of cpus employed were 4, with an exhaustiveness of 1000 and a maximum number of binding modes to generate of 100. The other parameters of AutoDock Vina were left with the default settings. The analysis of the docking results was done with the AutoDock Tools 4.2 software [12]and the obtained complexes were ranked considering their Vina score (kcal/mol) and the lowest binding energy conformer was selected for analysis. 2D diagrams of the interactions between the ligand and the receptor and the hydrophobic binding sites were represented with the software Discovery Studio Visualizer v.21.1.0.20298.[13]

NBD-1Py binding to Aβ:

Figure S30: a) to c) Binding modes for NBD-1Py with with the Aβ1–40 (PDB ID: 2LMP) amyloid plaque, and d) to f) for NBD-1Py with the Aβ1–42 (PDB ID: 2MXU) amyloid plaque. a) 3D image of the NBD-1Py-2LMP complex (surface of the receptor in light-blue and ligand in magenta). b) 3D image of the NBD-1Py-2LMP complex (receptor represented as ribbons and ligand with carbons in gray. Hydrogens are omitted for clarity). c) 2D-diagram of the interactions of NBD-1Py with 2LMP.

d) 3D image of NBD-1Py-2MXU ligand-receptor (surface of the receptor in light-blue and ligand in magenta). e) 3D image of NBD-1Py-2MXU interaction (receptor represented as ribbons and ligand with carbons in gray. Hydrogens are omitted). f) 2D-diagram of the interactions of NBD-1Py with 2MXU.

Table S4: Analysis of the close contacts between **NBDs-Py** and the amino acids residues of the amyloid plaque 2LMP ($A\beta_{1-40}$).

2LMP ($A\beta_{1-40}$)								
Amino acids[a]	Gly G	Ala A	Val V	Leu L	Ile I	Phe F	Asp D	Lys K
NBD-1Py ($E_{binding}$ = -14.1 kcal/mol)	L:GLY25	K:ALA21, L:ALA21	L:VAL24		L:ILE32	J:PHE19 K:PHE19 K:PHE20 L:PHE19		K:LYS28 L:LYS28
NBD-2Py ($E_{binding}$ = -14.1 kcal/mol)		O:ALA21 P:ALA21 Q:ALA30 R:ALA30		Q:LEU17	Q:ILE32 R:ILE32	O:PHE19 P:PHE19 P:PHE20 Q:PHE19 R:PHE19	R:ASP23	

[a] Legend: L:G25 is the amino acid Glycine 25 in the chain L.

Table S5: Analysis of the close contacts between **NBDs-Py** and the amino acid residues of the amyloid plaques 2MXU ($A\beta_{1-42}$).

2MXU ($A\beta_{1-42}$)					
Amino acids[a]	Gly G	Val V	Leu L	Ile I	His H
NBD-1Py ($E_{binding}$ = -12.7 kcal/mol)	D:GLY33	A:VAL12 B:VAL12 C:VAL12	A:LEU34 B:LEU17 B:LEU34 C:LEU34 D:LEU17	A:ILE32 B:ILE32 C:ILE32	B:HIS14 C:HIS14
NBD-2Py ($E_{binding}$ = -12.1 kcal/mol)	A:GLY33 D:GLY33	A:VAL12 B:VAL12 C:VAL12	A:LEU34 B:LEU17 C:LEU34 D:LEU17	B:ILE32 C:ILE32	B:HIS14 C:HIS14

[a] Legend: D:G33 is the amino acid Glycine 33 in the chain D.
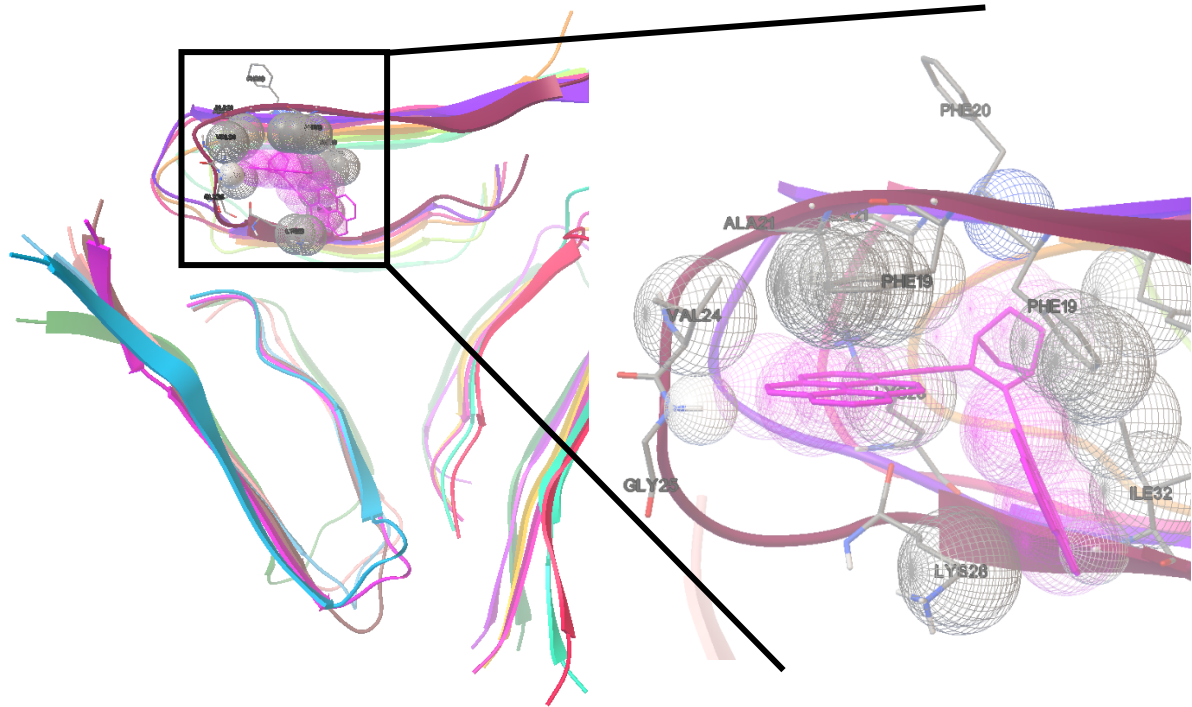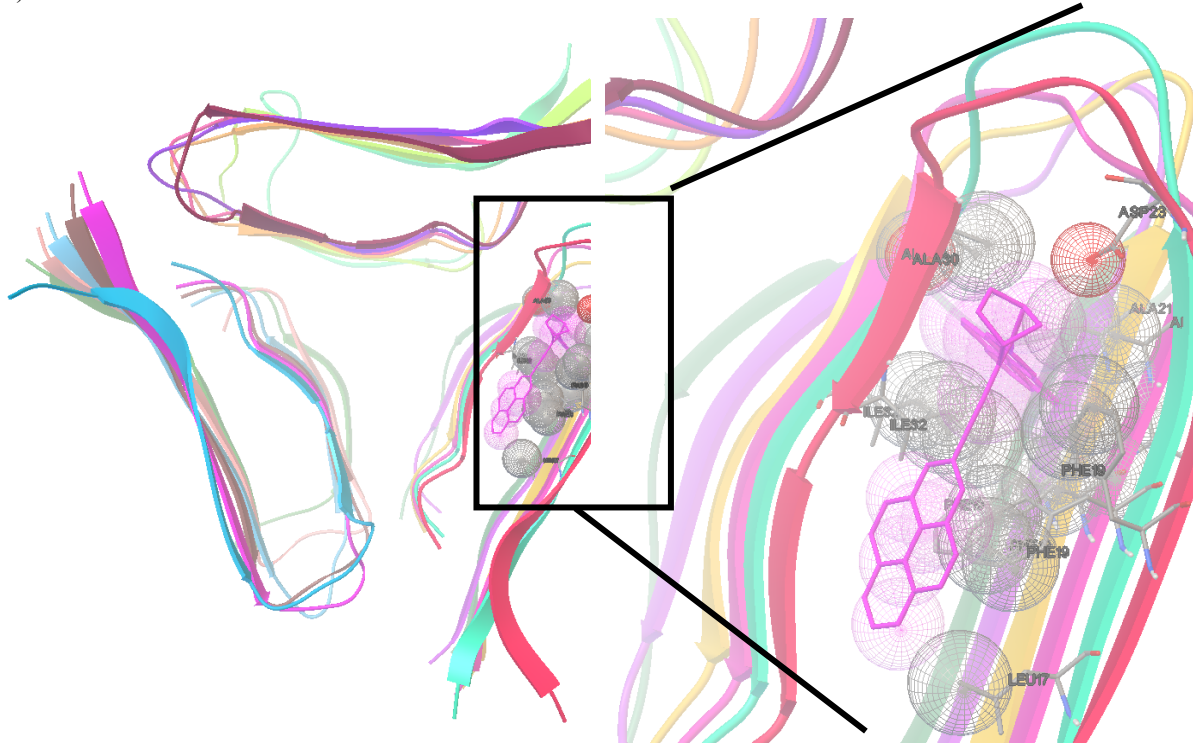
Figure S31: (a) Close contacts between **NBD-1Py** and (b) **NBD-2Py** interacting with the Aβ$_{1-40}$ amyloid fibril 2LMP. The receptors structures are coloured by chains and the ligands (NBDs-Py) are in magenta.
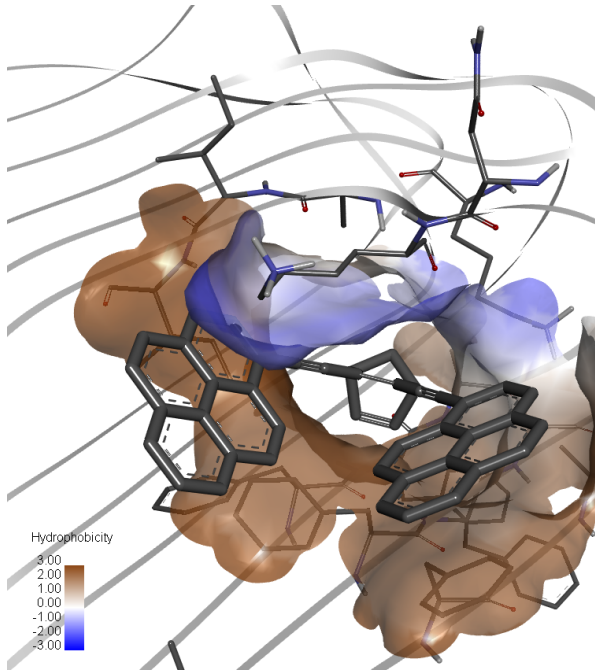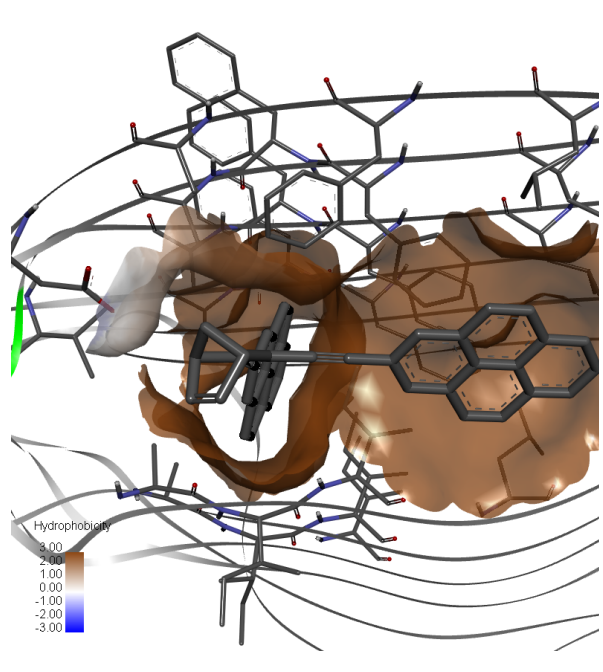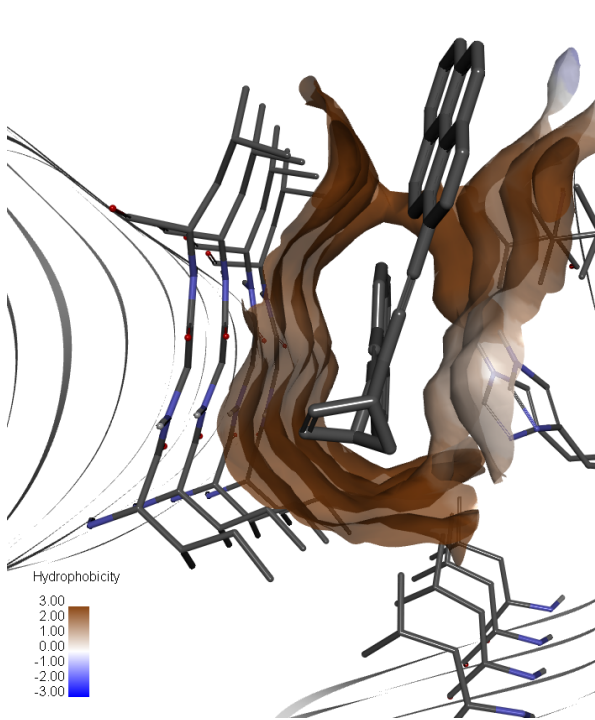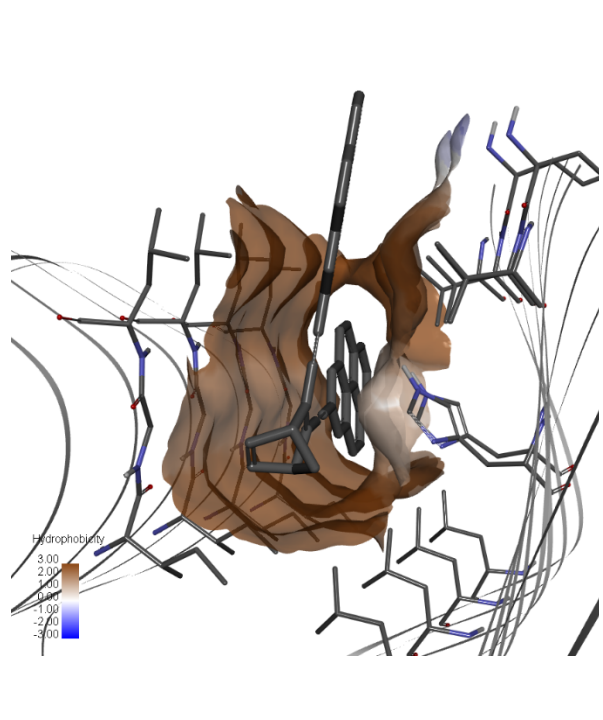
Figure S32: Hydrophobic binding sites for the interaction between (a) **NBD-1Py**-2LMP, (b) **NBD-2Py**-2LMP, (c) **NBD-1Py**-2MXU and (d) **NBD-2Py**-2MXU.

a)
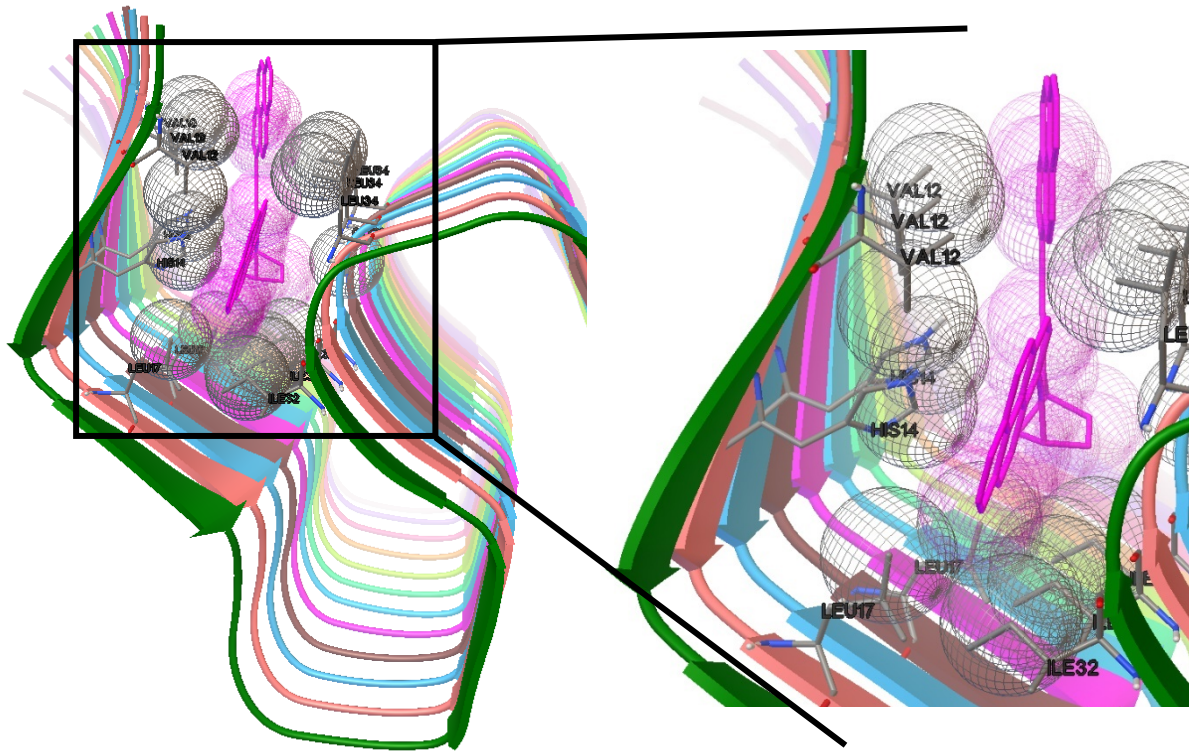
b)
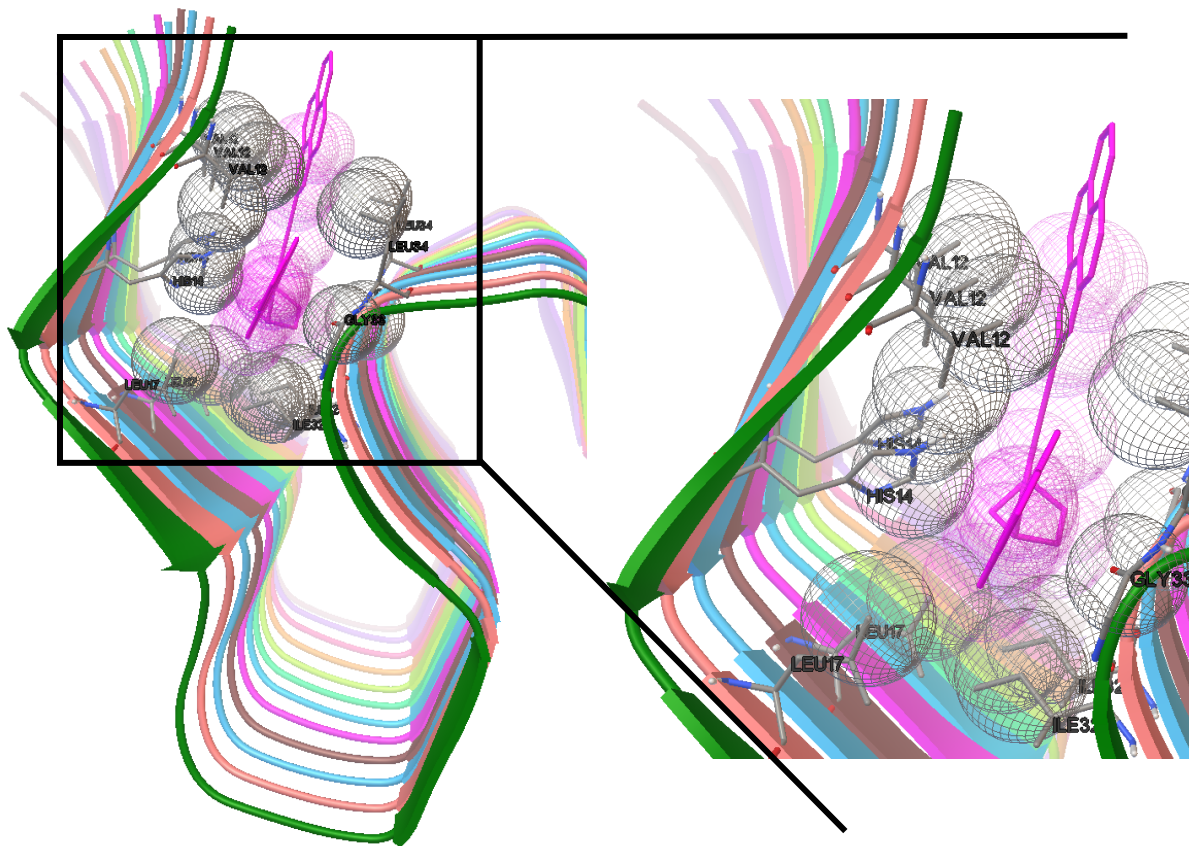
Figure S33: (a) Close contacts between **NBD-1Py** and (b) **NBD-2Py** interacting with the $A\beta_{1-42}$ amyloid fibril 2MXU. The receptors structures are colored by chains and the ligands (NBDs-Py) are in magenta.

7. Imaging of Abeta plaques

Mouse tissue preparation and NBD staining for imaging procedure

Mice tissues were provided by Dr. Dag Sehlin at Uppsala University. Transgenic AD mice carrying the Swedish mutation in APP (tgAPP$_{SWE}$) were reared *ad libitum* at an animal facility at Uppsala University under a 12/12 light cycle. Female 21-months old animals were anesthetized with isoflurane and sacrificed. The brains were dissected within 3 min post-mortem and frozen on dry ice. Animal procedures were approved by an ethical committee and performed in compliance with national and local animal care and use guidelines (DNr #C17/ 14 at Uppsala University). Frozen tissue sections of 12 μm thickness were cut in a cryostat microtome (Leica CM 1520, Leica Biosystems, Nussloch, Germany) at -18°C, collected on frosted microscope glasses (VWR). They were stored at -20°C and they were thawed under vacuum for up to 1 hour prior to performing the staining. NBD-1Py and NBD-2Py saturated solution in EtOH was prepared as followed: 1 mg was added to 10 mL of EtOH. The mixture was sonicated for 3 hours, and afterward it was centrifuged at 3000 rpm for 5 min. The obtained saturated solution was decanted to a new vial. The glasses mounted with the mouse brain sections were immersed in EtOH (1 min), EtOH 70% in MQ H$_2$O (1 min) and MQ H$_2$O or PBS (5 min), followed by 10 seconds in EtOH 70%. The samples were then positioned in a humidified chamber, 200 μL of a saturated solution of NBD in EtOH were added on top of the tissue and left to rest for 2 hours in the dark. Afterward, the samples were washed in EtOH (3 x 10 s) and MQ H$_2$O (3 x 5 min) and dried in an exicator for at least 30 minutes.

Immunohistochemistry

Brain sections collected on frost glasses were fixed in ice cold 95% ethanol, 70% ethanol and 1xPBS at room temperature. The sections were then blocked with Bovine Serum Albumin (BSA), Normal Goat Serum (NGS) and Triton in 0.1% PBST for 90 minutes at room temperature. The sections were incubated with anti Aβ antibody 6E10 (mouse, dilution 1:500 in NGS and 0.2% PBST) for over 18 hours at 4°C. Sections were washed with 0.1% PBST and incubated with the secondary antibody (Alexa-flour 647nm, goat anti mouse, 1:1000) for 60 min at room temperature, and then washed with PBS (3 x 5 min). Sections were finally mounted with DAKO fluorescent mounting media and left to rest for 24 hours at room temperature.

Imaging

Widefield fluorescence microscopy images were acquired with a Zeiss Axiolab 5 equipped with three fluorescence LED channels at 365 nm, 470 nm, 530 nm in combination with filter set 109. Confocal and hyperspectral images were collected on a Zeiss 880 Airscan laser scanning microscopy equipped with a 32-Channel GaAsP spectral detector and two PMTs. The objective used was Plan-Apochromat 20×/0.8 (WD = 0.55 mm), ∞/0.17. The excitation wavelength used for NBD imaging was 405 nm. The emission spectra were acquired between 415–600 nm. Images were processed with the Zen Black software (Zeiss) and ImageJ.
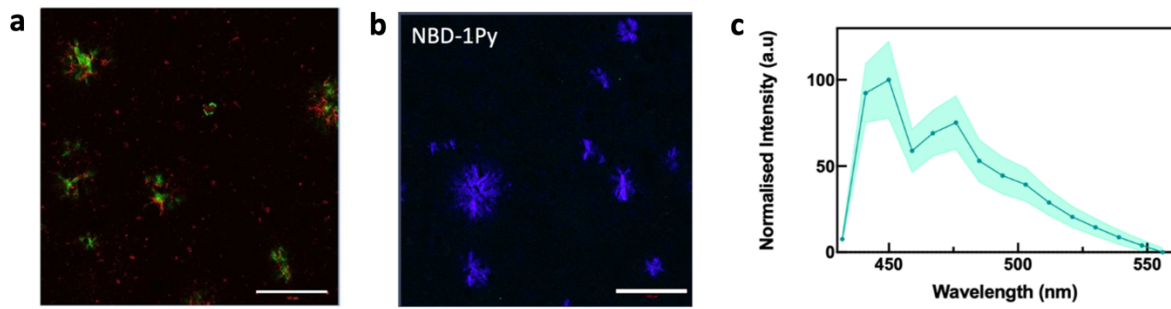
NBD-1Py staining of mouse tissues

Figure S34: a) Confocal image of Aβ plaques in cortex brain sections of Tg-APPSwe mouse model (21 months, female). Green is NBD-1Py, red is 6E10 anti amyloidβ antibody, white bar = 100 μm; b). Confocal hyperspectral image of Aβ plaques in cortex brain sections of a TgSwe mouse model (21 months, female) obtained with NBD-1Py as a fluorescent stain. White bar = 100 μm. c) *In situ* measured emission spectra of NBD-1Py when staining the plaques. The mean intensity values over the whole plaques area were extracted, and the average of 3 plaques together with the (green band) is shown.

NBD-2Py photoisomerization experiment *in situ* example
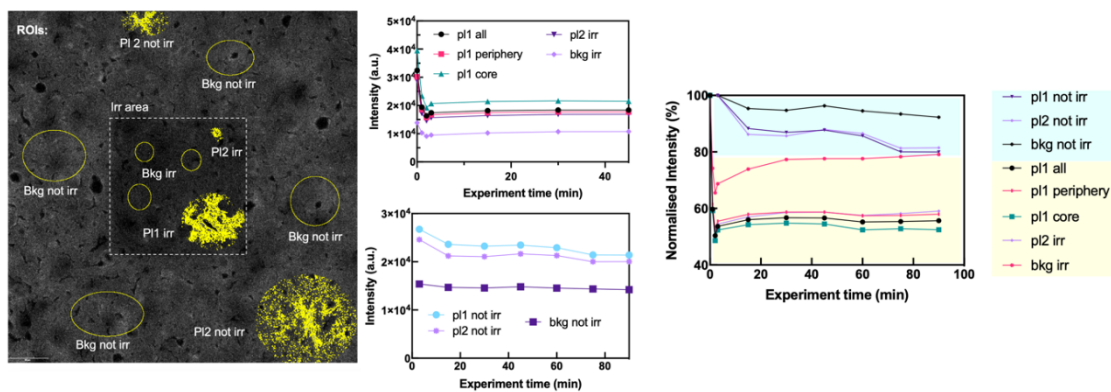
Figure S35: Example of photoisomerization experiment in situ with NBD-2Py. Zeiss LSM 880 airscan was used for this experiment. The irradiated area is subjected to intense irradiation (405nm LED at 10%), subsequently the image is zoomed out and images are acquired every 15 minutes with lower irradiation intensity (405nm LED 1%). After irradiation the signal of the plaques is significantly reduced (to about half of original values), and afterward is increasing. The plaques in the not irradiated areas show a decrease in signal intensity due to photobleaching or photoirradiation.

References

1. A. G. Crawford, Z. Liu, I. A. Mkhalid, M. H. Thibault, N. Schwarz, G. Alcaraz, A. Steffen, J. C. Collings, A. S. Batsanov and J. A. Howard, Synthesis of 2-and 2, 7-Functionalized Pyrene Derivatives: An Application of Selective C   H Borylation, *Chemistry–A European Journal*, 2012, **18**, 5022-5035.

2. Y.-Y. Chen, H. Wang, D.-W. Zhang, J.-L. Hou and Z.-T. Li, Organogels formed by substituent-free pyrene-appended oligo (m-phenylene ethynylene) s, *Chemical Communications*, 2015, **51**, 12088-12091.

3. K. Stranius and K. Börjesson, Determining the photoisomerization quantum yield of photoswitchable molecules in solution and in the solid state, *Scientific reports*, 2017, **7**, 41145.

4. G. Landrum, RDKit: A software suite for cheminformatics, computational chemistry, and predictive modeling, *Greg Landrum*, 2013, **8**, 31.

5. C. Bannwarth, S. Ehlert and S. Grimme, GFN2-xTB—An accurate and broadly parametrized self-consistent tight-binding quantum chemical method with multipole electrostatics and density-dependent dispersion contributions, *Journal of chemical theory and computation*, 2019, **15**, 1652-1671.

6. J. L. Elholm, A. E. Hillers-Bendtsen, H. Hölzel, K. Moth-Poulsen and K. V. Mikkelsen, High throughput screening of norbornadiene/quadricyclane derivates for molecular solar thermal energy storage, *Physical Chemistry Chemical Physics*, 2022, **24**, 28956-28964.

7. A. E. Hillers-Bendtsen, J. L. Elholm, O. B. Obel, H. Hölzel, K. Moth-Poulsen and K. V. Mikkelsen, Searching the Chemical Space of Bicyclic Dienes for Molecular Solar Thermal Energy Storage Candidates, *Angewandte Chemie International Edition*, 2023, e202309543.

8. T. Yanai, D. P. Tew and N. C. Handy, A new hybrid exchange–correlation functional using the Coulomb-attenuating method (CAM-B3LYP), *Chemical physics letters*, 2004, **393**, 51-57.

9. F. Weigend and R. Ahlrichs, Balanced basis sets of split valence, triple zeta valence and quadruple zeta valence quality for H to Rn: Design and assessment of accuracy, *Physical Chemistry Chemical Physics*, 2005, **7**, 3297-3305.

10. F. Neese, The ORCA program system, *Wiley Interdisciplinary Reviews: Computational Molecular Science*, 2012, **2**, 73-78.

11. O. Trott and A. Olson, Software news and update AutoDock Vina: Improving the speed and accuracy of docking with a new scoring function, *Effic. Optim. Multithreading*, 2009, **31**, 455-461.

12. G. M. Morris, R. Huey, W. Lindstrom, M. F. Sanner, R. K. Belew, D. S. Goodsell and A. J. Olson, AutoDock4 and AutoDockTools4: Automated docking with selective receptor flexibility, *Journal of computational chemistry*, 2009, **30**, 2785-2791.

13. D. S. Biovia, Discovery Studio Visualizer v21. 1.0. 20298, *San Diego: Dassault Systèmes*, 2021.

14. (DOI: 10.2210/pdb2lmp/pdb for 2LMP and DOI: 10.2210/pdb2mxu/pdb for 2MXU).

Paper II

Synthesis and Structure-Property Relationship of Multiple Site Functionalised Norbornadiene-Quadricyclane as Molecular Solar Thermal Materials for Energy Storage

Manuscript In Preparation, 2024

Synthesis and Structure-Property Relationship of Multiple Site Functionalised Norbornadiene-Quadricyclane as Molecular Solar Thermal Materials for Energy Storage

Monika Shamsabadi [a], Joost Kimpel [a], Christian Müller [a] and Kasper Moth-Poulsen [a,b,c]

[a] Department of Chemistry and Chemical Engineering, Chalmers University of Technology, 41296 Gothenburg, Sweden

[b] The Institute of Materials Science of Barcelona, ICMAB-CSIC, Bellaterra, 08193 Barcelona, Spain.

[c] Catalan Institution for Research & Advanced Studies, ICREA Pg. Lluís Companys23, 08010 Barcelona Spain

ABSTRACT:

The pursuit of efficient and sustainable energy storage technologies is paramount in transitioning towards a cleaner energy future. Norbornadienes (NBDs) have emerged as promising candidates owing to their reversible photoisomerisation capabilities, offering potential solutions to the challenges faced by traditional energy storage systems. However, the practical implementation of NBDs is hindered by issues such as solubility and stability. In this study, we investigate site modifications of NBDs to enhance their solubility and half-life, crucial parameters for their utility in molecular solar thermal systems (MOSTs). Leveraging experimental investigations and computational simulations, we comprehensively characterise the solvation behaviour of NBDs in various solvents and assess their stability under diverse operating conditions. Furthermore, we delve into the synthesis and purification of NBD products to ensure high yields and purity, essential for their effective deployment in energy storage applications. Our findings offer insights into addressing key challenges in NBD-based energy storage, propelling the development of sustainable and efficient alternatives for renewable energy integration.

Introduction

The shift towards a cleaner, more sustainable energy future necessitates the development of efficient and scalable energy storage technologies to overcome the intermittency of renewable energy sources. Traditional energy storage solutions, such as lithium-ion batteries, have made significant advancements, but they still face challenges related to energy density, cost, and environmental sustainability. As a result, there is a growing interest in exploring alternative materials and chemistries to address the escalating demand for high-performance energy storage systems. Organic compounds, known for their versatility and tuneable properties, have garnered considerable attention in recent years as potential candidates for next-generation energy storage materials. Among these, norbornadienes (NBDs) have emerged as fascinating molecules with the potential to address some of the limitations of current energy storage technologies. NBDs exhibit photoisomerization, transitioning into highly strained quadricyclanes (QCs) upon irradiation. This photoswitching behaviour enables efficient energy capture and release. Additionally, NBDs feature reversible isomerization, triggered by thermal, catalytic, or light-induced activation. This isomerization process is highly exothermic, making NBD an ideal candidate for energy storage applications, where efficient energy storage and release are paramount.

However, before NBD can be harnessed as a practical energy storage material, several critical aspects must be thoroughly investigated and understood. The solubility of NBD in various solvents, which directly impacts its practicality in energy storage applications, needs to be comprehensively characterized. Additionally, the stability of NBD and its ability to withstand repeated cycling without significant degradation are crucial factors in determining its viability as a long-term energy storage solution.

In this study, we embark on a systematic exploration of the solubility and stability of NBD, aiming to provide a comprehensive understanding of its potential for advanced energy storage applications. Through a combination of experimental investigations and computational simulations, we will elucidate the solvation behaviour of NBD in different solvents and assess its stability under various operating conditions. Our findings hold the promise of unlocking new possibilities in the field of energy storage, paving the way for sustainable and efficient energy solutions in the years to come.

Experimental

General Procedure. A one-step synthesis was conducted using available starting materials, to explore the impact of functionalising different sites of norbornadiene (NBD) on the system's properties. Beginning with a substituted cyclopentadiene mono, the electron-

donating diene underwent efficient reaction in a Diels-Alder reaction with an alkyne functionalised with electron-accepting ester groups.

Microwave Synthesis. To a solution of diethyl acetylenedicarboxylate (XX g, X mmol) in oDCB were added cyclopentadiene precursor. The microwave vial was sealed, and the mixture was heated in a microwave reactor at 190°C for 8 hours. The reaction mixture was then purified by automated flash chromatography with 0-20% ethyl acetate in hexane. The product was collected as a pale-yellow oil after the solvent had been removed using a rotary evaporator. After the sample was kept at an oven temperature of 50°C to remove residual diethyl acetylenedicarboxylate.

Thermal Synthesis. A 50 mL round-bottomed flask, XX g (XX mmol) of diethyl acetylenedicarboxylate was added, followed by the gradual addition of XX g (XX mmol) of cyclopentadiene. The reaction mixture generated a significant amount of heat shortly after the addition of cyclopentadiene, persisting for several minutes. After 10mins, 10mL of solvent was added if the reaction was not performed neat. It was then left at to stir overnight to ensure completion. The crude product was purified using automated flash chromatography with 0-20% ethyl acetate in hexanes. The resultant NBD was collected as a pale-yellow oil after the fractions had been collected and the solvent had been removed using rotary evaporator.
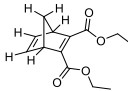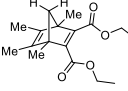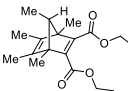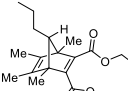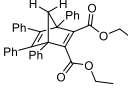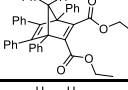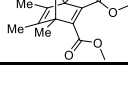
Theoretical Modelling. Initial geometry optimization of NBD and QC structures was performed using the B3LYP functional with 6-311++G level of theory. A solvent model (SMD) with chloroform simulated the eluent of the HPLC measurement. Natural bond orbital analysis (POP = NBO) was added since the intramolecular cycloadditions in the interconversion invokes the σ^* and π^* orbitals. Even though the contribution of this interaction is generally minimal, especially in the extrema (NBD *versus* QC), it is considered nonetheless given the pericyclic nature of the interconversion. Structures are verified to be at a minimum energy by vibrational analysis.

Result and discussion

Optimisation. Starting with the unsubstituted dicyclopentadiene (DCPD), the cleavage of this moiety into the cyclopentadiene monomer was achieved *via* Microwave-assisted synthesis. This was carried out in the presence of diethyl acetylenedicarboxylate, thereby enabling the

subsequent generation of NBD1 *via* Diels-Alder reaction (Scheme X). To refine the reaction conditions for both dicyclopentadiene cracking and Diels-Alder reactions, small-scale experiments were carried out where Microwave-assisted synthesis parameters such as, temperature, reaction time and the pressure were studied. The results are presented in Table XX.

With this information in hand, synthesis of the other NBD derivatives was conducted as a comparative study between Thermal synthesis and Microwave-assisted synthesis with the previous optimised parameters (Table XX).

Molecule	Structure	Type	Solvent	Yield
NBD 1		MR	None	28%
		MR	oDCB	45%
NBD 2		TR	CDCl$_3$	73%
		MR	oDCB	10%
		TR	None	24%
NBD 3		TR	CDCl$_3$	50%
		MR	oDCB	76%
		TR	None	41%
NBD 4		TR	CDCl$_3$	83%
		MR	oDCB	23%
		TR	None	25%
NBD 5		TR*	oDCB	60%
		MR	oDCB	35%
		TR	None	20%
NBD 6		TR	oDCB	0%
		MR	oDCB	34%
NBD 7		TR	CDCl$_3$	85%
		MR	oDCB	26%

Excluding NBD1 and NBD6, Thermal synthesis sufficed for the synthesis of all other NBDs. This approach was facilitated by the availability of pre-purchased monomeric cyclopentadiene starting materials for NBD2-NBD5 and NBD7, negating the necessity for cracking conditions. Intrudingly, the experiments unveiled a significant decrease in yields at high temperatures during Thermal synthesis, contradicting the expected yield enhancement thought to come from cracking any dimer formed during the reaction. Microwave-assisted synthesis was conducted in *o*-dichlorobenzene (oDCB) to achieve the required temperatures for dimer cracking, while Thermal synthesis was carried out in either chloroform or without solvent (neat). The high-temperatures in Microwave-assisted synthesis enabled the formation

of undesired side-products, including NBD polymers and ester decarboxylation, along with retro Diels-Alder reactions. However, this method orived advantageous in the case of NBD6, circumventing the unfavourable reaction between the bulky 1,2,3,4,5-pentaphenyl-1,3-cyclopentadiene precursor and the electron-poor dienophile, diethyl acetylenedicarboxylate, a feat unachievable under Thermal synthesis conditions.

Notably, an increase in yield during Thermal synthesis was not observed in the synthesis of NBD3 (XX%) when compared to Microwave-assisted synthesis (XX%). Further analysis revealed significant variations in the ratios of desired product to side-products, an occurrence attributed to the varying chemical compositions of the precursors. This variance was reasoned to be influenced by the fluctuating levels of inactive cyclopentadiene dimer present as well as the competing interactions between the increase in electron-donating power and the steric hindrance.

The subsequent phase involved optimising the Diels-Alder procedure within Thermal synthesis. Starting with the cyclopentadiene monomer, 1,2,3,4-tetramethyl-1,3-cyclopentadiene and diethyl acetylenedicarboxylate for the synthesis of NBD2, additional small-scale experiments were screened, with the results of which are summarised in Table XX. Initial findings from the comparative study revealed that the highest yields of NBD2 (XX%) were obtained when replicating conditions that were used for conventional synthesis (Thermal synthesis). The optimisation experiments underscored that high temperatures were dispensable for NBD formation, as the electron-donating diene readily engaged with the electron-accepting ester-functionalised alkyne. Furthermore, it was further emphasised from this study that higher temperatures favoured the formation of impurities, exacerbating with longer reactions times, prompting investigation into shorter durations with hight temperatures.

For the NBDs synthesised without the assistance of microwave irradiation, the results consistently showed higher presence of the corresponding NBD's photoisomer. In response, a new strategy was devised to mitigate the formation of the quadricyclane (QC) photoisomer, a particularly challenging impurity to separate due to similarities in molecular polarity and weight. This strategy involved conducting the reaction in amber vials, facilitated by the small reaction volume achievable by running the reaction neat. Although, reactions neat resulted in lower yields (XX%) – the employment of the amber vials increased the yield as less QC was formed.

Purification. Facing the challenge of isolating side-products, a comparative evaluation of various purification methods was undertaken. Initially, the hydrodynamic volumes of NBD and
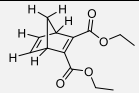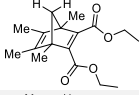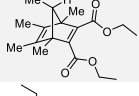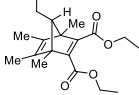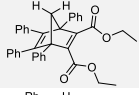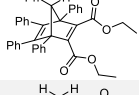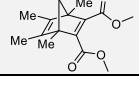
QC were computed using Density Functional Theory (DFT) intending to purify them *via* High-Pressure Liquid Chromatography (HPLC). HPLC proved successful in purifying NBD 2 after approximately 40 cycles spanning 1110 minutes. However, as sample sizes increased, the feasibility of HPLC diminished due to the typical maximum loading capacity of HPLC columns, limited to 500 mg (requiring 180 hours for complete purification of 5 grams.) Consequently, NBD 3 and 4 were purified using a Kugelrohr apparatus under a 5 mtorr dynamic vacuum. This method effectively purified the sample as it aided in DCPD cracking and removal of residual alkyne due to its low boiling point. Nevertheless, exposure to light during purification resulted in a mixture of the parent compound and photoisomer, surpassing the light exposure experienced during HPLC purification. Subsequently, automated flash chromatography was employed for purification, offering superior light protection compared to Kugelrohr apparatus but was unable to completely eliminate the acetylene. Thus, the comparative investigation underscores the efficacy of HPLC in purifying these NBDs. In cases where the product crystallised in the reaction mixture (NBD5 and NBD6), further purification was achieved through HPLC to separate the solid product from its unreacted solid precursor.

Solubility. The solubility of the synthesised NBDs was assessed, considering the inherent challenges posed by the limited solubility of NBDs complicating material integration in devices. Qualitative analysis of raw experimental data pertaining to the solubility of NBD derivatives revealed that the positioning, quantity, and nature of substituents exerted notable influences on the compound's solubility. A direct correlation was observed between increased substitution (NBD1 – NBD3) and enhanced solubility, a trend further underscored by longer bridge chain lengths (NBD3 and NBD4). Comparison with NBD phenyl variants (NBD5 and NBD6) highlighted the significantly diminished solubility of bulkier groups.

These findings highlight the improved solubility achieved through the incorporation of alkyl groups, offering potential solutions to previously reported poor solubility encountered with top-performing NBDs in the field. However, it is important to acknowledge the qualitative nature of the experiment. The pale appearance of NBD1 – NBD4 oils complicates visual assessment of complete dissolution, particularly under dim lighting conditions required during experiments. As a result, the quantity of solvent required for full dissolution may occur.

Photophysical evaluation. UV-vis spectra of the new NBD series were recorded in both acetonitrile (MeCN) and toluene, as shown in Table X. A comparative analysis of the NBD

data was conducted to observe the effects of altering the number of substitution sites on the absorption spectra (Figure X).

Entry	Structure	A_{max}	A_{onset}	M_w	ε_{max}
NBD 1		232	282	236.3	4304
NBD 2		239	293	292.4	3768
NBD 3		234	315	306.4	4738
NBD 4		242	286	334.5	4039
NBD 5		220	294	540.7	12198
NBD 6		-	-	616.8	-
NBD 7		240	276	264.3	4452

An increase in the number of carbons around the NBD structure (NBD 1 to NBD 4) resulted in a slight redshift in the spectra. However, this trend was not observed with phenyl substituents, as these groups are weakly electron-withdrawing, likely reducing the HOMO – LUMO gap and causing a more blue-shifted spectrum. Notably, changing the ester groups from ethyls to methyls led to a significant redshift, possibly due to the steric effects of the less bulky methyl groups.
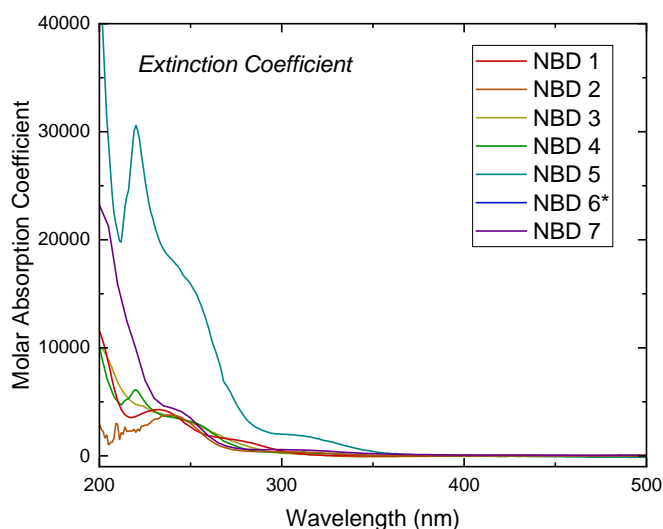
Upon converting the NBDs to their respective QC derivatives via irradiation under short UV light (265 nm), degradation of the molecules was observed. Previous studies suggested that irradiation of an ester at 258 nm produced a localised excited state, yielding a bicyclo[4.1.0] derivative. To circumvent this mechanism, a 300 nm lamp was employed. Furthermore, the irradiation was carried out using a degassed solution to explore any mechanisms involving ambient oxygen (Figure XX).
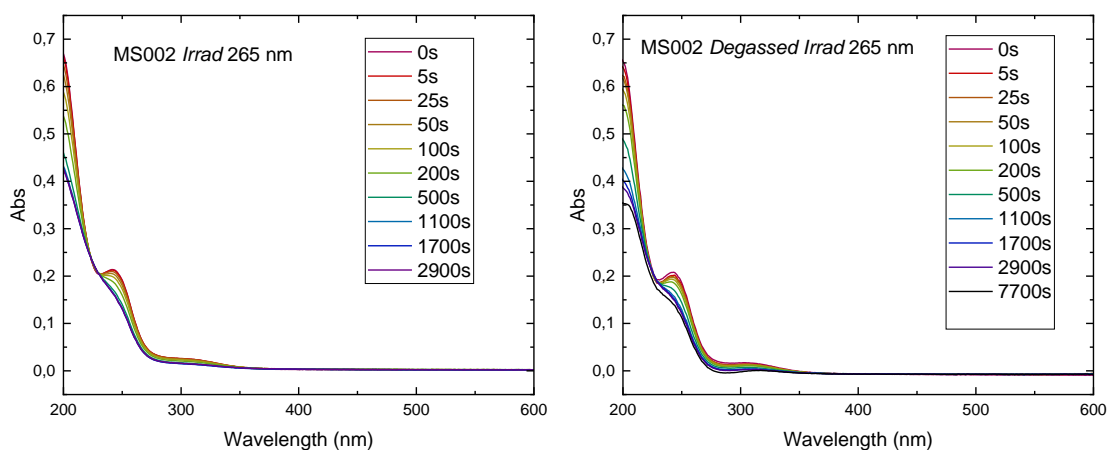
Despite implementing these measures, degradation persisted following back conversion. In an attempt to mitigate this issue, *N,N*-dimethylformamide (DMF) with a cut-off wavelength was utilized as a solvent to filter out input light below 270 nm, thereby minimizing photodegradation. However, even upon recovery of the parent molecule, degradation persisted, albeit to a lesser extent. Subsequently, investigation into the degradation of the back conversion was conducted, revealing increased degradation at higher temperatures, suggestive of a combination of mechanisms, possibly including a retro Diels-Alder reaction (Figure XX). As a result, accurate measurement of the quantum yield and half-lives of the molecules was precluded due to the involvement of multiple mechanisms.
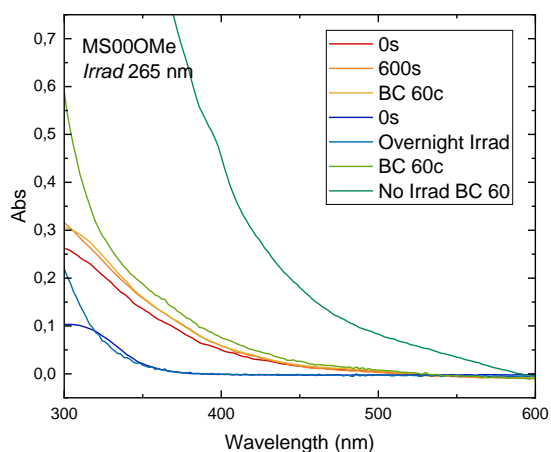
Supporting Information

Synthesis and Structure-Property Relationship of Multiple Site Functionalised Norbornadiene-Quadricyclane as Molecular Solar Thermal Materials for Energy Storage

Monika Shamsabadi [a], Joost Kimpel [a], Christian Müller [a] and Kasper Moth-Poulsen [a,b,c]

TABLE OF CONTENTS

1 General Materials and Methods

Chemicals. All chemicals, reagents and solvents were purchased from commercial sources and used as received unless otherwise noted.

NMR Spectroscopy. NMR spectra were recorded on an Avance NEO 600 FT spectrometer (^{1}H: 600 MHz, ^{13}C: 150.9 MHz). The spectra were referenced to the residual solvent peaks (chloroform: δ (^{1}H) = 7.26 ppm, δ (^{13}C) = 77.16 ppm). Analysis was executed with Mestrelab Mestrenova v11.0.4. Peak assignments were supported by COSY, HSQC and HMBC experiments.

UV-vis Spectroscopy. All UV-vis spectra were measured in transmission. UV-vis spectra in solution were measured at 25 °C on a Cary 60 UV-vis (Agilent Technologies). High Temperature UV/Vis spectra were measured using 0.02 mg/mL solutions of polymers in *o*-DCB in sealed glass cuvettes. The samples were heated using a sample holder from Agilent and 10°C/min heating rate from 30°C to 150°C, with a stabilization time of 5 min for each temperature.

2 Experimental Procedures

Synthesis of 1a
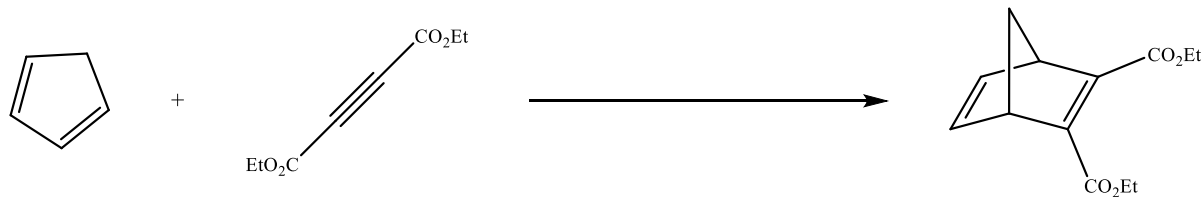
¹H NMR (600 MHz, CDCl3) δ 6.92 (t, J = 2.0 Hz, 2H), 4.23 (q, J = 7.2 Hz, 4H), 3.97 – 3.88 (m, 2H), 2.28 (dt, J = 6.7, 1.7 Hz, 1H), 2.08 (dt, J = 6.7, 1.5 Hz, 1H), 1.30 (t, J = 7.1 Hz, 6H).

Synthesis of 2a
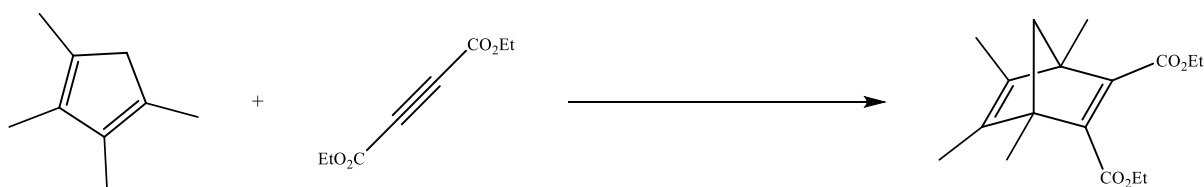
¹H NMR (800 MHz, CD₃CN) δ 4.15 (q, J = 7.1 Hz, 4H), 2.04 (d, J = 6.4 Hz, 1H), 1.80 (d, J = 6.4 Hz, 1H), 1.67 (s, 6H), 1.40 (s, 6H), 1.23 (t, J = 7.1 Hz, 6H).

Synthesis of 3a
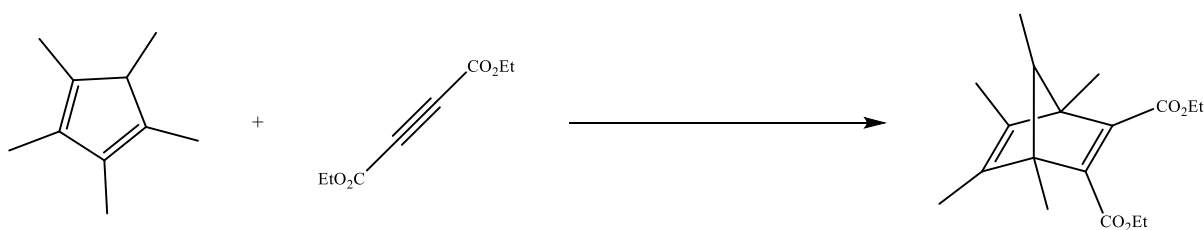
¹H NMR (800 MHz, CD3CN) δ 4.17 – 4.10 (m, 4H), 2.27 (q, J = 6.4 Hz, 1H), 2.11 (d, J = 6.4 Hz, 0H), 1.68 (s, 5H), 1.63 (s, 5H), 1.22 (td, J = 7.2, 0.8 Hz, 11H), 0.81 (d, J = 6.4 Hz, 2H), 0.70 (d, J = 6.3 Hz, 3H).

Synthesis of 4a
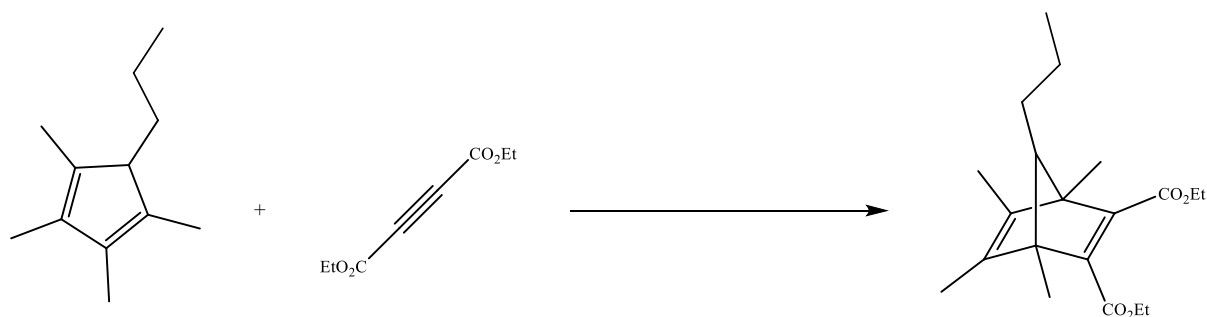
Synthesis of 5a
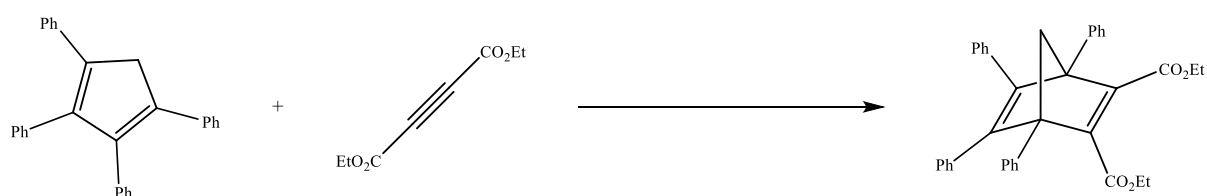
^{1}H NMR (400 MHz, CDCl3) δ 7.22 – 7.01 (m, 3H), 6.93 (ddd, J = 13.6, 7.2, 1.9 Hz, 2H), 4.17 (qd, J = 7.1, 4.6 Hz, 1H), 1.15 (t, J = 7.1 Hz, 2H).

Synthesis of 6a
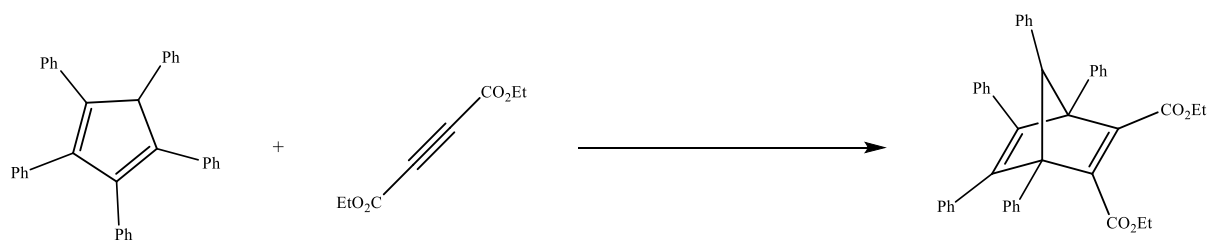
^{1}H NMR (600 MHz, CD3CN) δ 7.21-6,98 (m, 25H), 4.55 (s, 2H), 4.21 – 4.09 (m, 4H), 1.15 (m, J = 11.0 Hz, 6H).

Synthesis of 7a
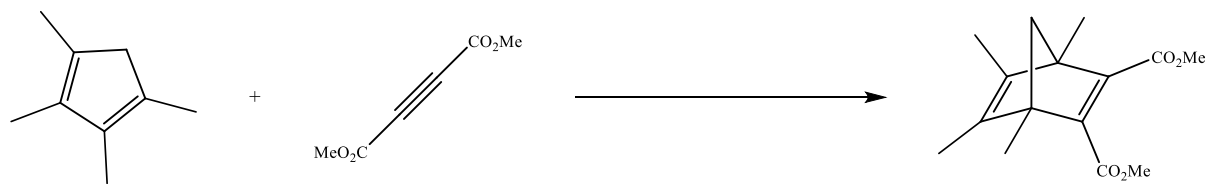
^{1}H NMR (800 MHz, CD3CN) δ 3.68 (s, 6H), 2.05 (d, J = 6.4 Hz, 1H), 1.80 (d, J = 6.4 Hz, 1H), 1.66 (s, 6H), 1.39 (s, 6H).

3 NMR Spectra

MS003FCa2.2.fid
PCAL
SM_1H1D CDCl3 /opt/nmrdata/Chalmers CTH-KaMoPo{2 E6 - 254}

Figure S1. ^{1}H-NMR spectrum of (**1a**) in CDCl3 at 298K.
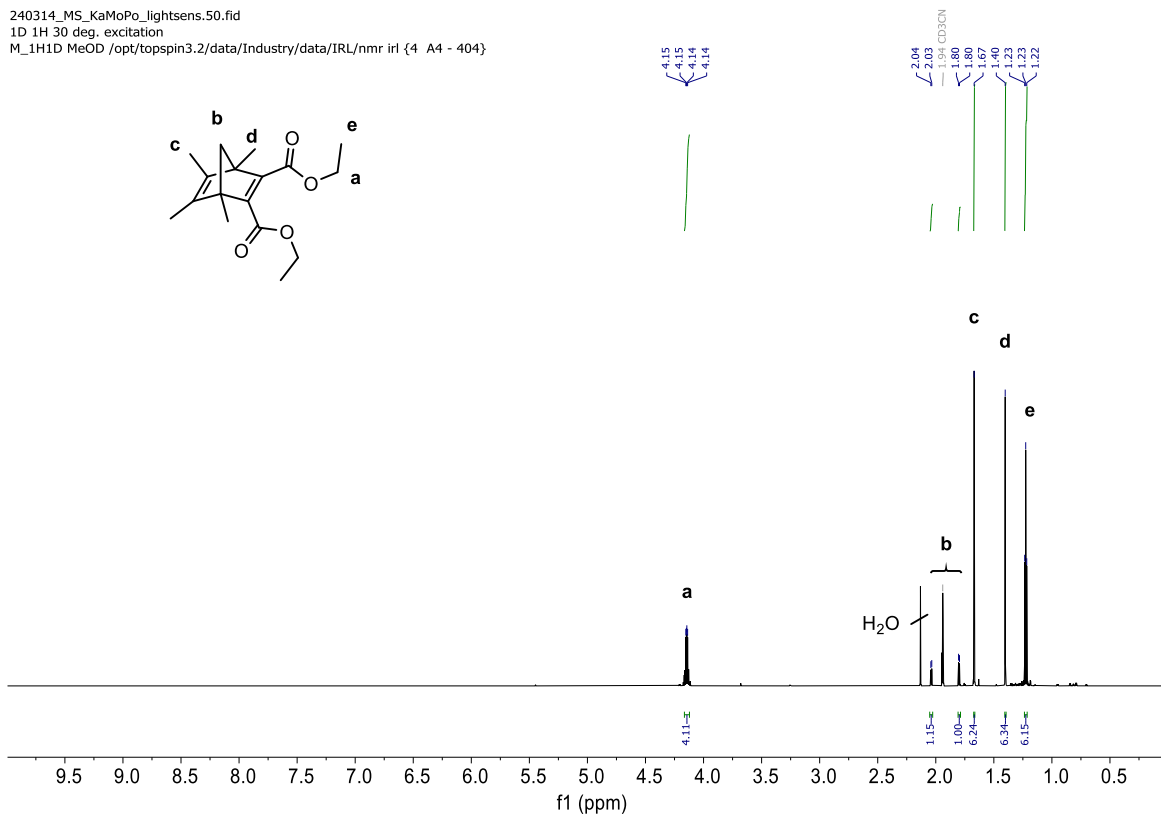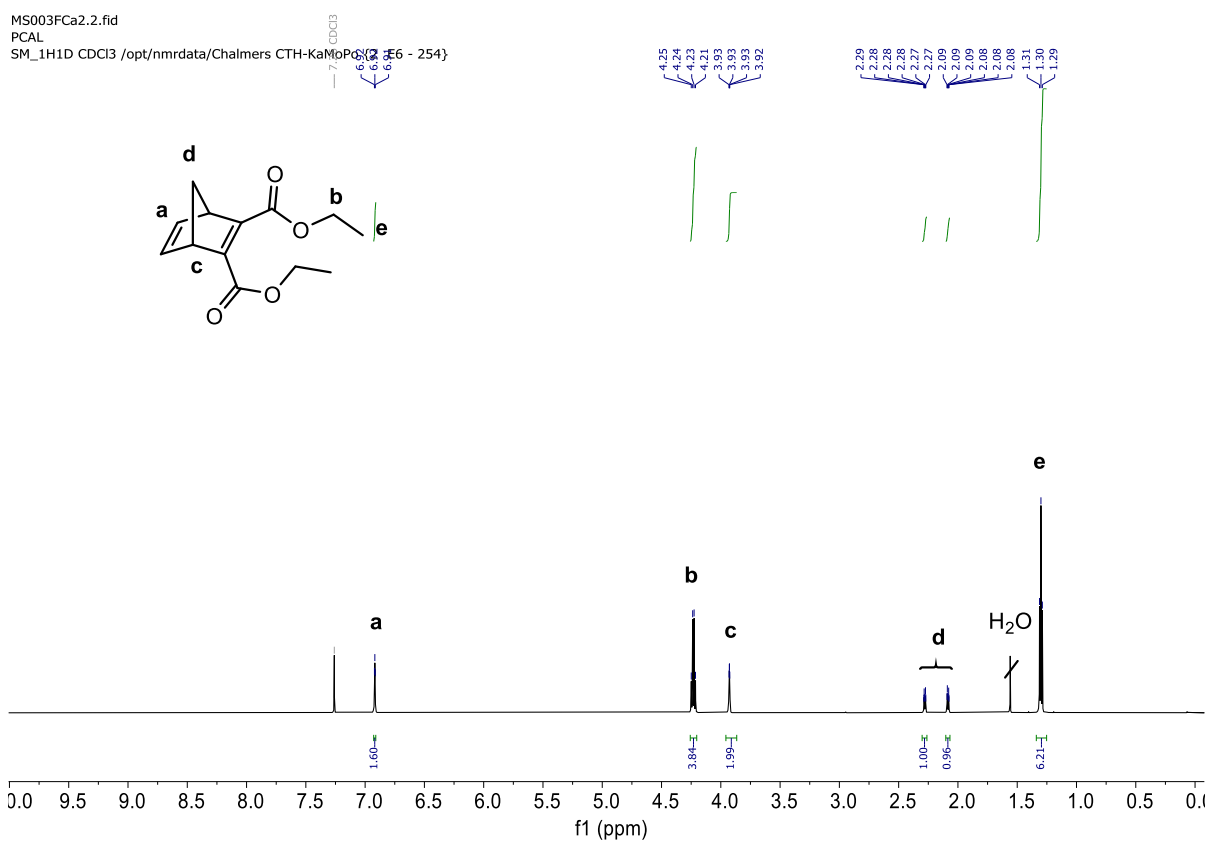
240314_MS_KaMoPo_lightsens.50.fid
1D 1H 30 deg. excitation
M_1H1D MeOD /opt/topspin3.2/data/Industry/data/IRL/nmr irl {4 A4 - 404}

Figure S2. ^{1}H-NMR spectrum of (**2a**) in CD3CN at 298K.
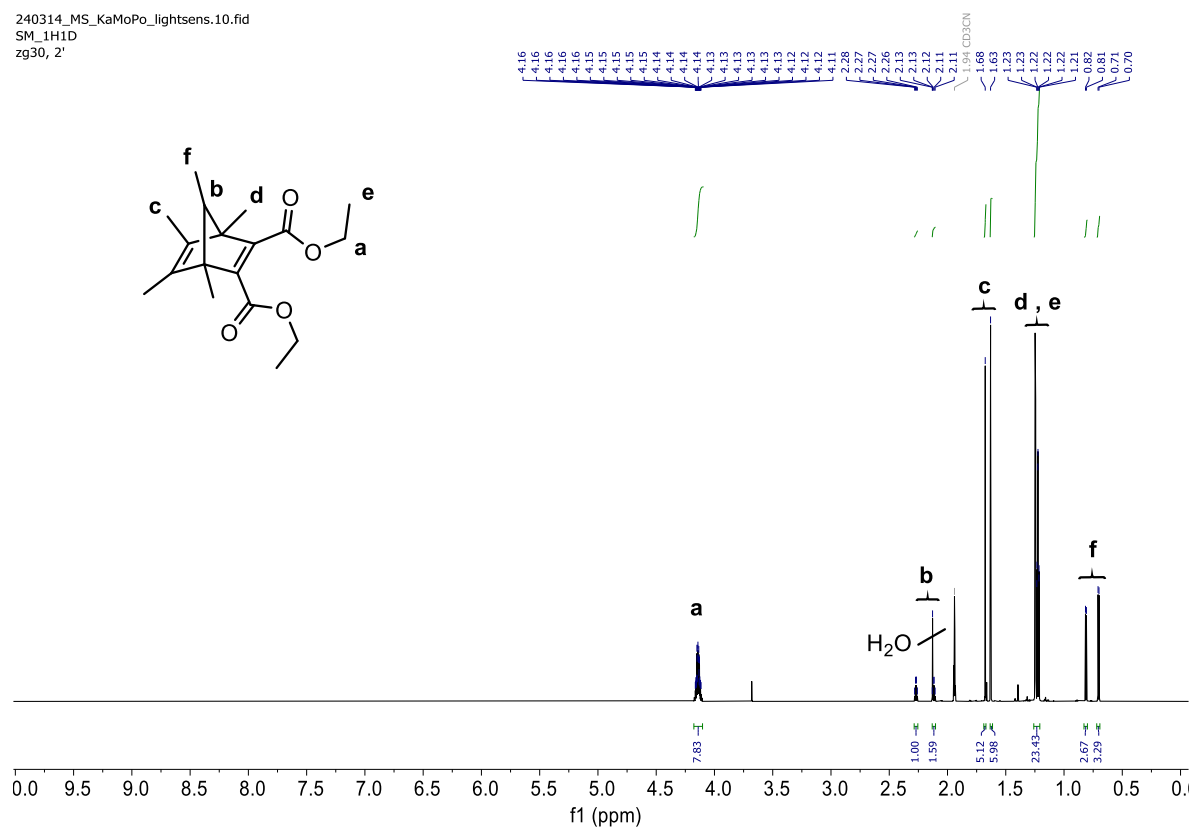
Figure S3. ^{1}H-NMR spectrum of (**3a**) in CD3CN at 298K.
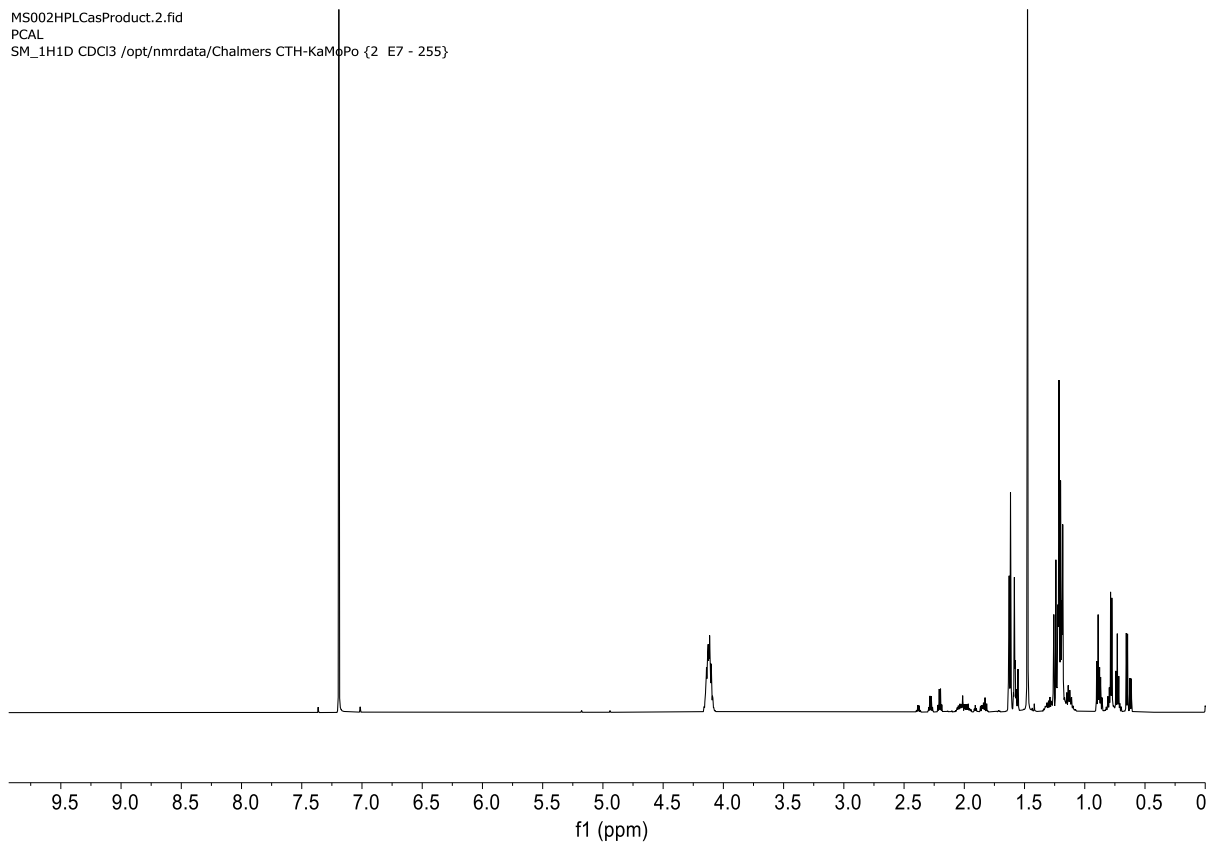
Figure S4. ^{1}H-NMR spectrum of (**4a**) in CD3CN at 298K.
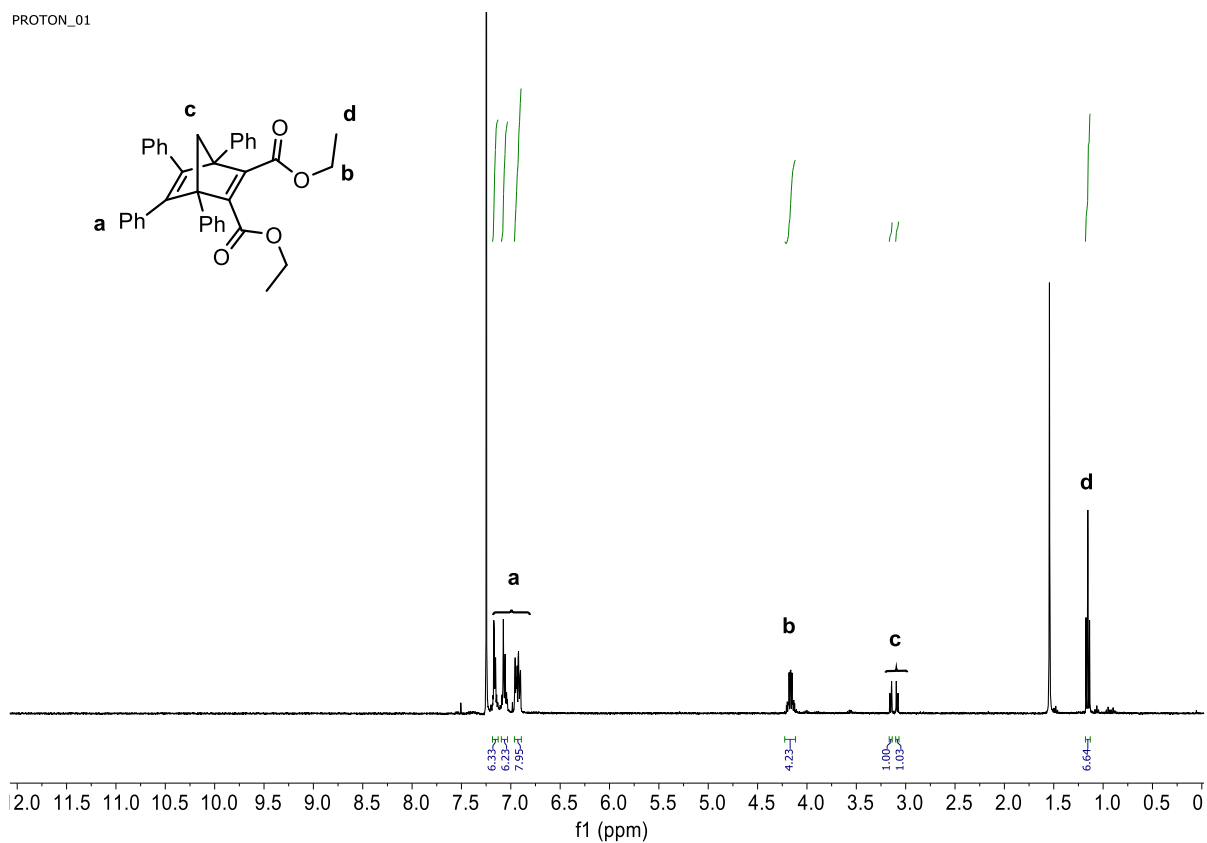
Figure S5. ^{1}H-NMR spectrum of (**5a**) in CD3CN at 298K.
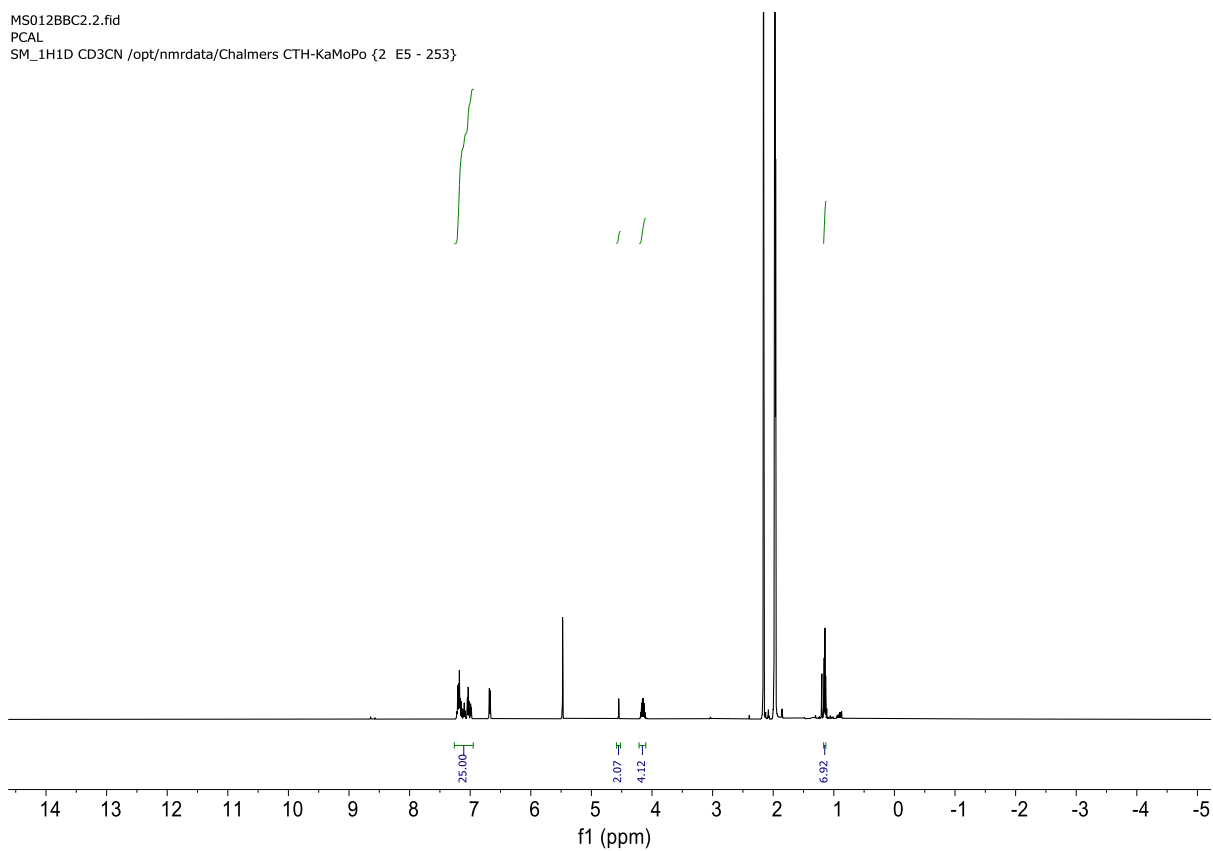
Figure S6. ^{1}H-NMR spectrum of (**6a**) in CD3CN at 298K.
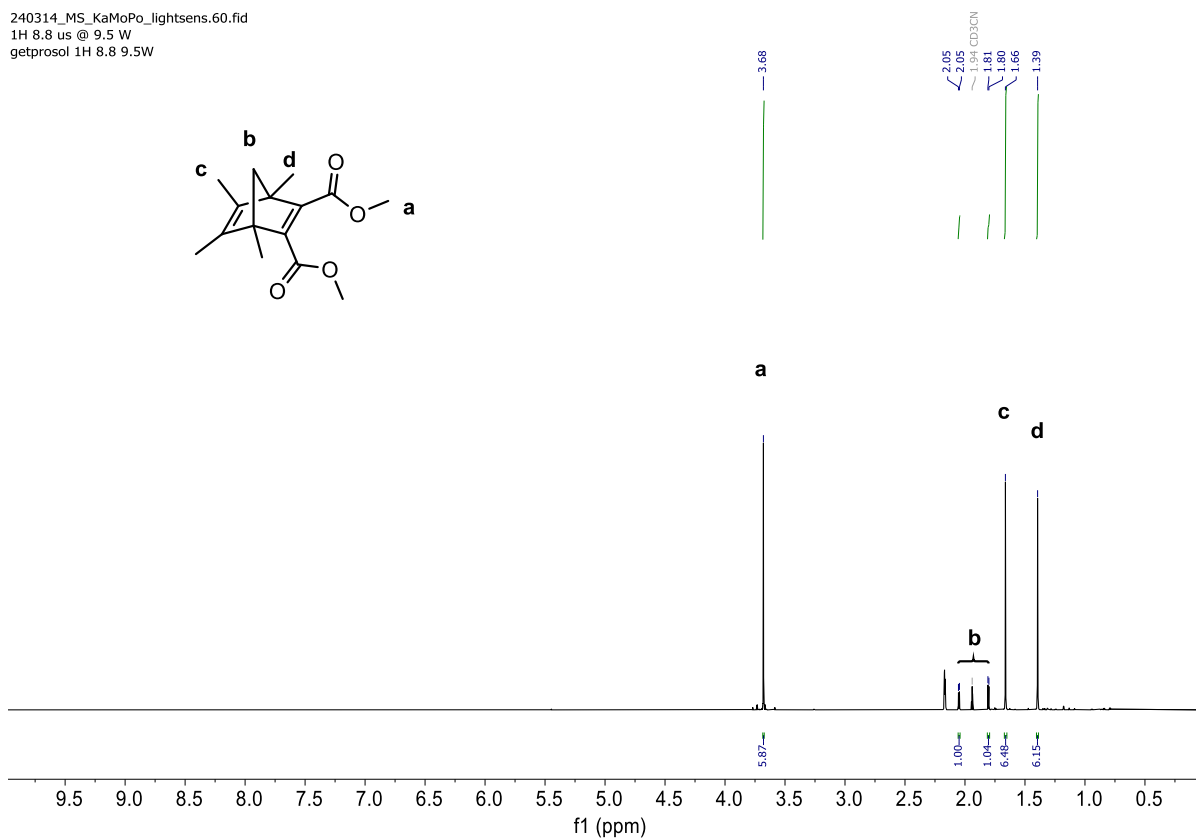
Figure S7. ^{1}H-NMRspectrum of (**7a**) in CD3CN at 298K.

4 Computation

```python
import numpy as np

def distance(point, center):
    return np.linalg.norm(point - center)

def find_smallest_sphere(points, threshold=1e-6):
    center = np.mean(points, axis=0)
    radius = np.max(np.linalg.norm(points - center, axis=1))

    while True:
        distances = np.array([distance(point, center) for point in points])

        new_radius = np.max(distances)

        if np.abs(new_radius - radius) < threshold:
            break

        surface_points = points[np.isclose(distances, new_radius)]
        center = np.mean(surface_points, axis=0)
        radius = new_radius

    return center, radius

coordinates = [
    [x, y, z],
    [x, y, z],
    [x, y, z],
    [x, y, z]
]

points = np.array(coordinates)

center, radius = find_smallest_sphere(points)
```

Subsequently, the hydrodynamic volume of the molecules was determined by using the following algorithm, which iteratively creates the smallest sphere that encompasses all points (atoms):

Given the low rotational energy barrier for the ethyl groups on the ester in **NBD/QC 1-7** and the propyl group in **NBD/QC 4**, determined by scanning these angles with the B3LYP functional at 6-31+G level of theory, free rotation is expected at room temperature. Note that this rotation is not considered for the methyl esters as the rotation would be the CH_3 cone rotation and insignificant. Regioisomers on the bridgehead are assumed to be pointing away from the ester groups. Coordinates of several conformers are determined where the dihedral angle of the ethyl groups are separately rotated in steps of 60° (0° to 180°) and the dihedral angle of the propyl group is rotated in steps of 30° (90° to 180°). Coordinates of all other atoms relax after each scan to accommodate for the structural change, i.e. no imaginary frequencies observed. An average hydrodynamic volume is then determined from sixteen sets of coordinates for **NBD/QC 1-3** and **NBD/QC 5-7**, and sixty-four sets of coordinates for **NBD/QC 4**.

In the interconversion between NBD and QC, changes in molecular volume are observed. In all cases except the unsubstituted core (**NBD/QC 1**), the volume decreases as the molecule converts from NBD to QC. The unsubstituted core is the only molecule where the atoms on the different ester groups create the largest atom-atom distances which could explain this irregularity in the trend. More substituted cores have a smaller percentage difference in volume between the NBD and QC. The conformational change of the relatively flat NBD to the puckered QC would intuitively lead to a decrease in volume.

X_1 = H, Me, Ph; X_2 = H, Me, Ph
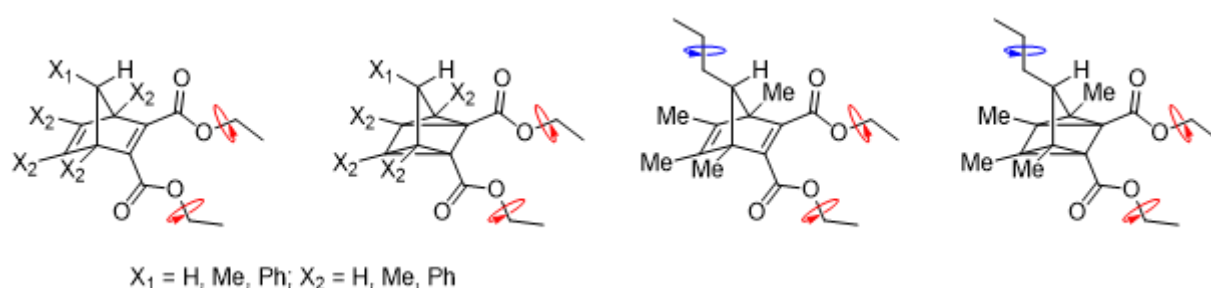
Figure SX. Dihedral angles altered to determine conformer structures. Red arrows are rotated in steps of 60° (0° to 180°) and blue arrows are rotated in steps of 30° (90° to 180°). Conformers shown in image have all angles of interest set to 180°, extended chain.

Table SX. Volumes of different structures determined by smallest enclosing sphere analysis of conformers.

Molecule	Structure	Volume ($Å^3$)	Molecule	Structure	Volume ($Å^3$)	ΔV (%)
NBD 1		534 ± 8	QC 1		656 ± 16	+ 23
NBD 2		804 ± 16	QC 2		768 ± 15	- 4.5
NBD 3		867 ± 14	QC 3		856 ± 9	- 1.3
NBD 4		1125 ± 7	QC 4		1107 ± 9	- 1.6
NBD 5		1651 ± 9	QC 5		1474 ± 11	- 12
NBD 6		1511 ± 27	QC 6		1462 ± 7	- 3.2
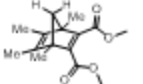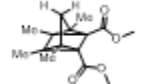
Molecule	Structure	Volume	Molecule	Structure	Volume	
NBD 7		530	QC 7		491	- 7.4

Table SX. Volumes of different structures determined by Monte Carlo analysis (volume function in Gaussian) of molecules.

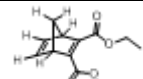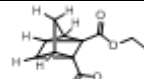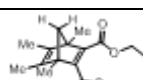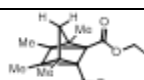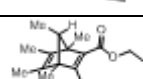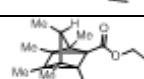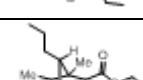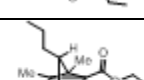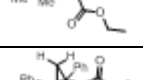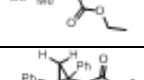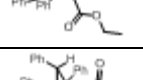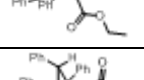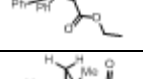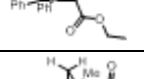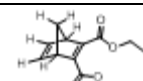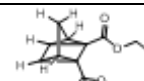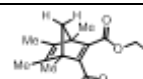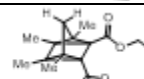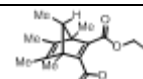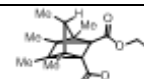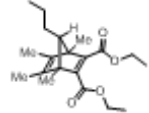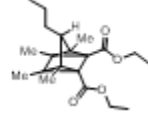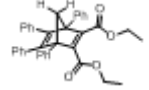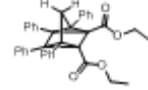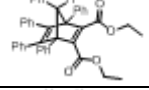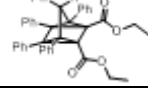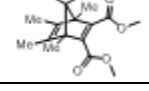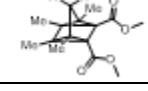| Molecule	Structure	Volume (Å^3)	Molecule	Structure	Volume (Å^3)
NBD 1		280 ± 210	QC 1		230 ± 160
NBD 2		370 ± 200	QC 2		420 ± 360
NBD 3		420 ± 40	QC 3		400 ± 205
NBD 4		465 ± 430	QC 4		280 ± 240
NBD 5		680 ± 120	QC 5		630 ± 390
NBD 6		780 ± 390	QC 6		Not done
NBD 7		350 ± 240	QC 7		320 ± 220

Table SX. Volumes of different structures determined by largest diameter of molecule in most stable conformation (longest atom-to-atom distance found).

Molecule	Structure	Volume (Å^3)	Molecule	Structure	Volume (Å^3)
NBD 1		424	QC 1		362
NBD 2		596	QC 2		366
NBD 3		596	QC 3		532

NBD 4		1044	QC 4		1040
NBD 5		1126	QC 5		1108
NBD 6		1210	QC 6		1106
NBD 7		388	QC 7		358

Paper III

Structure Properties Relationship of p-Alkoxy-Azobenzenes as Molecular Solar Thermal Phase Change Material for Energy Storage Systems

Manuscript In Preparation, 2024

Structure Properties Relationship of *p*-Alkoxy-Azobenzenes as Molecular Solar Thermal Phase Change Material for Energy Storage Systems

Conrad Averdunk,[a,b] Monika Shamsabadi,[c] Kasper Moth-Poulsen,[d] Hermann A. Wegner [a,b]

[a] Institute of Organic Chemistry, Justus Liebig University Giessen
Heinrich-Buff-Ring 17, 35392 Gießen (G6ermany)
[b] Center of Materials Research (ZfM/LaMa), Justus Liebig University
Heinrich-Buff-Ring 16, 35391 Giessen (Germany)
[c] Department of Chemistry and Chemical Engineering, Chalmers University of Technology,
41296 Gothenburg, (Sweden)
[d] Institute of Materials Science of Barcelona (ICMAB-CSIC), Polytechnic University of
Catalunya
Campus de la UAB, 08193 Barcelona (Spain)
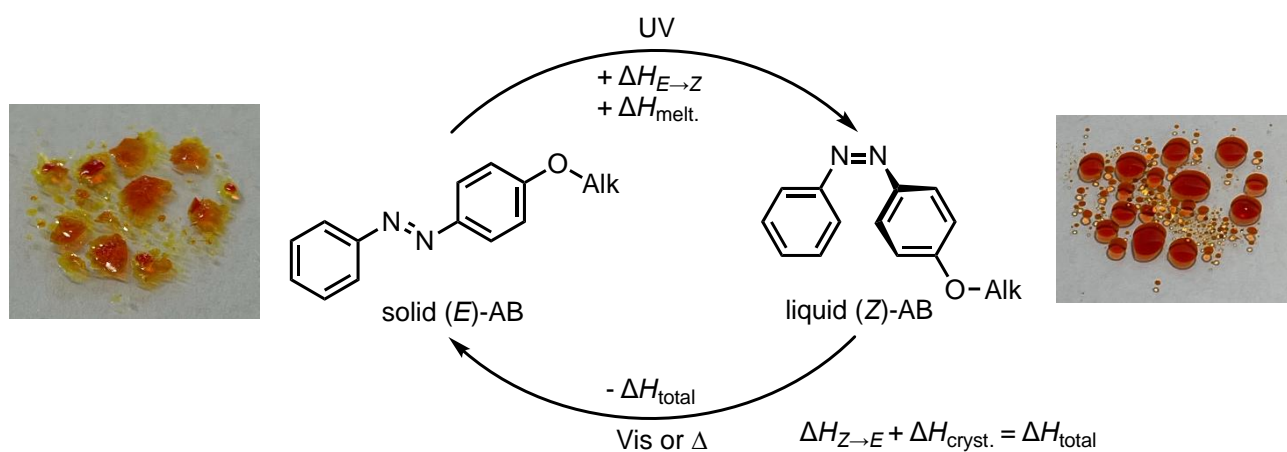
ABSTRACT: In recent years, various molecular photoswitches have been investigated for application as energy storage devices. Azobenzene (AB) is an promising candidate due to its easy accessibility and stability. However, it suffers of a low energy density. In recent years, there have been various approaches to increasing storage density by increasing the energy difference between the respective photoisomers. A new approach is to combine the photoisomerization with a solid ↔ liquid phase transition enabling harvesting solar energy and ambient heat simultaneously. Thus, the photoisomerization of the crystalline (*E*)-isomer can be used to obtain the liquid (*Z*)-isomer. Due an external trigger the *cis*-liquid → *trans*-crystal back reaction releases the stored energy as isomerization enthalpy (ΔH_{isom}) as well crystallization enthalpy (ΔH_{cryst}). In order to optimize such MOST-PCM, a series of *p*-alkoxy-azobenzenes with different chain lengths were prepared to investigate the structure-property relationship of the melting points, kinetics, photoisomerizability and absorption in the solid state and in solution.

Introduction

Due to increasing energy demand and environmental pollution the development of renewable and sustainable energy sources is necessary. The storage of solar energy is one of the most attractive, sustainable and environmentally friendly methods. A possibility for storing solar energy is the conversion of photon energy into chemical energy. One promising approach is molecular solar thermal energy storage (MOST) systems, which store solar energy in chemical energy due photochemical reactions. For such systems molecular photoswitches are used, which are capable of absorbing photon energy to enable photoisomerization resulting in energetically excited meta-stable photoisomers. The energy difference of the respective photoisomers corresponds to the energy that can be stored in this system. The stored energy can be released as thermal energy during the backreaction. Several molecular photoswitches were developed and investigated in recent years, including azobenzenes, falvulenes, norbornadienes and dihydroazulene. Azobenzenes are favorable due to their high accessibility and stability. They can be switched from its thermodynamically stable (*E*)-isomers to its energetically excited metastable (*Z*)-isomer. However, this system suffers from low energy density. In past years there have been several approaches to increase the energy difference between the respective photoisomser to increase the storage capacity.

A new promising approach to increase the energy storage density is the combination of the photoisomerization with a solid ↔ liquid phase transition. This allows to store, not only the photon energy through photoisomerization, but also to store thermal energy from the ambient temperature through the simultaneous melting process. The (*Z*)-isomer needs a lower melting point than the (*E*)-isomer. Therefore, liquid (*Z*)-isomer can be obtained by irradiation of the solid (*E*)-isomer harvesting solar energy and ambient heat simultaneously. A solid-liquid phase transition can only occur if the melting point of the (*Z*)-isomer is sufficiently low and that of the (*E*)-isomer sufficiently high. Thus, the melting points of the (*E*)- and (*Z*)-isomer are limiting the temperature range in which the system can be used. Conceptual a high melting point of the (*E*)-isomer and a low melting point of the (*Z*)-isomer would be desirable. Subsequently, back isomerization can be induced by an external influence, whereby the stored energy will be released in the form of heat.

However, a distinction must be made between two different types of MOST-PCM systems. In the first type, photoisomerization of the azobenzene is possible within the crystal structure. This allows an irradiation induces trans-crystal → cis-liquid transition under isothermal conditions. However, these systems require a sufficiently large free pore volume to allow molecular movement during photoisomerization within the crystal structure.

In the second type photoisomerization within the crystal structure is not possible due to a lack of free pore volume, which prevents any molecular movements within the crystal structure. Therefore, the (*E*)-isomer needs to be thermally liquefied to loosen the crystal structure and increase the mobility for molecular mobility. After photoisomerization of the (*E*)-isomer to the (*Z*)-isomer in the liquid phase the

system must be cooled below the melting point of the (*E*)-isomer to enable recrystallization during the energy release. This type of MOST-PCM is often combined with traditional organic PCM to increase the control over energy release.

Literature known azobenzene based MOST-PCM are usually substituted in the *para* position with alkoxy or carboxy alkyl chain in different length and functionalities. For such systems it has been shown that the position and the length of the alkyl chain or other substituents strongly influence properties of the (*E*)- and (*Z*)-isomer. However, the influence of chain length on properties such as the melting point on the photoisomers, half-lives or energy storage density, for example, does not show a linear behavior and is difficult to comprehend. For better understanding of the structure-property relationship in such MOST-PCM systems, a simple model system was used to investigate the influence of different chain lengths on the physical properties. As model system *p*-alkoxy azobenzenes with different chain lengths were used. Therefore, in this study not only the influence on the melting points of the (*E*)- and (*Z*)-isomers or thermodynamic parameters such as the energy storage density are quantified, but kinetic investigations should also be carried out. One important parameter is the half-life with which the energy can be stored in the system. On the other hand, the speed with the MOST-PCM can be charged is decisive. The maximum temperature change that can be achieved is also crucial for discharging.

Results

Synthesis of *p*-Alkoxy-Azobenzenes. The investigated *p*-alkoxy azobenzenes were prepared *via* two different synthesis routes. For short alkoxy groups, the respective *p*-alkoxy-aniline was oxidized with Oxone to the corresponding nitroso compound and then treated with unsubstituted aniline in a Baeyer Mills reaction under acidic conditions to obtain the respective *p*-alkoxy-Azobenzenes. For the synthesis of *p*-Alkoxy-Azobenzenes with longer chain lengths, unsubstituted aniline was converted into the corresponding diazonium salt under acidic conditions with sodium nitrite in the first step of the synthesis. Subsequently, the diazonium salt reacted with phenol in a classic azo coupling under basic conditions to obtain the *p*-hydroxy-Azobenzene. Afterwards, *p*-hydroxy-azobenzene was treated with the respective bromo alkanes under basic conditions to obtain the *p*-alkoxy azobenzenes in a Williams etherification.

Photochemical properties of *p*-Alkoxy-Azobenzens in solution. In order to investigate the photochemical properties and the influence of different chain lengths UV-Vis absorption spectra in acetonitrile were measured of each compound to determine the absorption maximum. All *p*-alkoxy azobenzenes showed a red shifted absorption maximum of the π-π* band at 347 nm and a absorption maximum of the n-π* band at around 440 nm in the ground state. Different wavelengths were tested to obtain the most effective photoisomerization. The highest amount of (*Z*)-isomer in the photostationary state was obtained by irradiation with a wavelength of 340 nm. For the (Z) → (*E*) isomerization irradiation with 448 nm was the most effective wavelength.

The composition of the respective photoisomers at the photo stationary states at 340 nm and 448 nm was determined *via* HPCL. It can be seen that with increasing chain length the effectiveness of the photoisomerization for the (*E*)→(*Z*) isomerization is slightly decreasing from around 76% to around 73%. This could be caused by the increasing steric hinderance of the alkoxy chains lowering the mobility for the inversion and rotation during the photoisomerization. For the (*Z*)→(*E*) photoisomerization with 448 nm the amount of the (*E*)-isomer is slightly increasing with increasing chain length at the respective photo stationary state. Furthermore, an explanation for the variation of the composition in the photostationary states with increasing chain length could be caused by solubility effects, which could lead to decreasing solubility. The increasing non-polar tail of the *p*-Alkoxy-Azobenzenes could influence the stabilization of the respective isomers in a polar solvent.

In addition, kinetic studies of the *p*-alkoxy azobenzenes in acetonitrile at a temperature of 40°C were carried out. It was found that the half-life is generally increasing with the increasing length of the alkoxy chain. A noticeable phenomenon here is the alternating increase of the half-life's, which could be explained by the odd-even effect due to the different interaction strengths of the alkyl chains. Furthermore, it seems that the increase of the half-life saturates at a certain chain length. The increasing half-life could also be explained by the increasing steric demand or by attractive interactions between the alkoxy chains. Alkoxy chains with an even number of carbons have a longer half-life and those with an odd number have a shorter half-life.
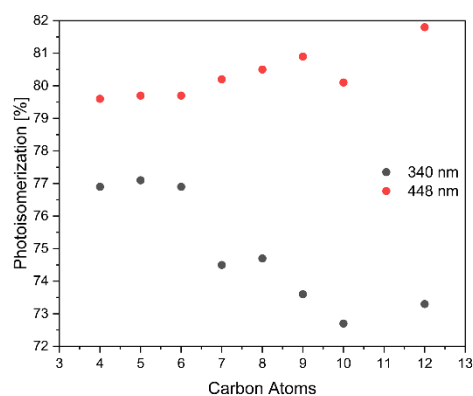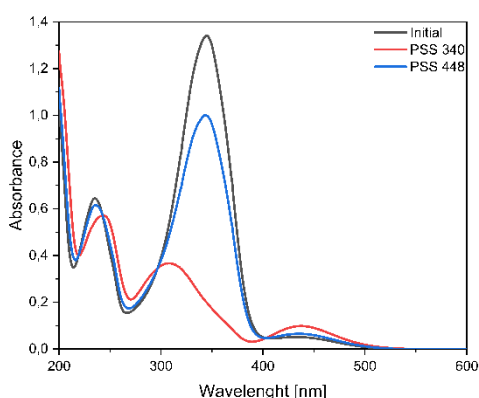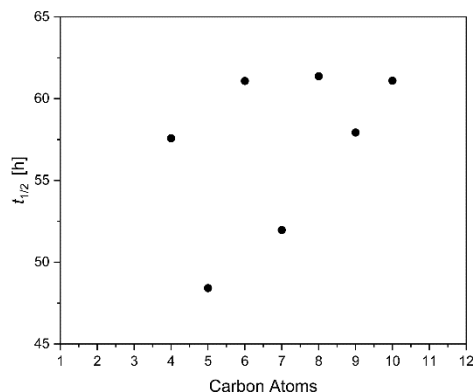
Reversible solid → liquid phase transition. To investigate the properties of the irradiation induced solid → liquid phase transition from the solid (*E*)- to the liquid (*Z*)-isomer of the different *p*-Alkoxy-AB different wavelengths were tested to achieve the most effective photoisomerization of the solid state. However, irradiation of the neat AB with 340 nm, which corresponds to the absorption maximum of the π-π* band at 347 nm in solution leads not to a successful photoisomerization. Instead, irradiation with 365 nm leads to an successful light-induced phase transition from solid to liquid, which was observed for all synthesized *p*-Alkoxy-AB. Due to intramolecular interactions between the azobenzene moieties in the solid state a red shift of the absorption maxima of the π-π* band is reasonable. The energy release and liquid to solid phase transition from the (*Z*)- to the (*E*)-isomer was induced by irradiation with a wavelength of 448 nm.

For better understanding of the photophysical properties UV-Vis spectroscopy was performed with thin films of the corresponding azobenzenes. In the solid-state UV-Vis absorption spectrum of the (*E*)-isomer, an absorption maximum can be seen at approx. 320 nm with a small shoulder at approx. 370 nm. Furthermore, a low absorption maximum can be recognized at approx. 440 nm. Irradiation of the solid azobenzene with 365 nm leads to a strong increase in the intensity of the absorption maximum at 440 nm. Additionally, the intensity of the shoulder increased at approx. 370 nm and the intensity also increased at approx. 260 nm. The absence of an isosbestic point is conspicuous. After an irradiation time of about 300 s the intensity of the absorption maximum at 440 nm remains almost unchanged. Interestingly, no further increase in the intensity of the shoulder is observed with further irradiation; instead, there is a decrease in intensity. Furthermore, an isosbestic point is observed from an irradiation duration of 300 s. After an irradiation time of 420 s with 365 nm, the photostationary state was reached. A comparison of the spectra between the initial state and the photostationary state at 365 nm shows that the intensity of the shoulder at 370 nm is approximately the same. Thus, the two different behaviors of the change of the absorption spectrum can be divided into two different processes. When the initial state is irradiated, there is an unusually strong increase in the n-π* band. This phenomenon can be attributed to anisotropic properties of the solid azobenzene. With increasing irradiation, the azobenzene becomes

increasingly randomly oriented, causing the anisotropy to decrease. Quantum mechanical calculations have shown that the transition dipole moment of the n-π* band is located in the plane of the azobenzene. Assuming that the orientation of the azobenzene is parallel to that of the substrate surface, the absorption is measured perpendicular to the transition dipole moment of the n-π* band. This means that the absorption is low at the beginning of the measurement. The absorption increases with increasing irradiation and thus decreasing anisotropy. This effect is observed as long as a certain amount of anisotropy is present in the solid or the mixed phase. This also explains the absence of an isosbestic point. As soon as the azobenzene has completely converted to the liquid phase, there should no longer be any anisotropic properties, which is confirmed by the presence of an isosbestic point. The change in the n-π* band is only slight. In addition, a decrease in the intensity of the shoulder at 370 nm can be observed, which corresponds to a typical change in the absorption band of azobenzenes in solution.

During irradiation with 365 nm at room temperature of each compound, it was observed that not all p-Alkoxy-ABs were converted into the liquid (Z)-isomer with the same efficiency, even if the ambient temperature is above the melting point of the respective (Z)-isomer. This observation can be explained on the one hand by the increasing melting points of the (Z)-isomers with increasing chain length and the associated increase in steric hindrance of the alkoxy chains. Therefore, the ambient temperature required for an effective phase transition increases with melting points and chain lengths. If the melting point of the respective (E)-isomer is high, a higher mole fraction of the respective (Z)-isomer must be obtained in order to compensate the larger temperature difference of the ambient temperature and melting point. Furthermore, as a liquid phase is obtained later, the mobility of the molecule is hindered for an extended time by the crystal structure. A explanation for this phenomenon is that the mobility of the individual azobenzenes is hindered or even completely prevented by the tightly packed crystal structure. A reduced mobility of the azobenzenes due to the crystal structure therefore also has a considerable influence on the photoisomerization. This process is not only dependent on the ambient temperature or the intensity of the irradiation, but also on the degree of mobility of the azobenzenes within the crystal structure. Therefore, when choosing a chain length, a balance must be considered between the resulting increase in melting point and steric hindrance and the change in free pore volume.

Subsequently, ^{1}H-NMR analysis was used to investigate the composition of the photoliquefied azobenzene after it had been irradiated with 365 nm at room temperature for a certain period of time. It was shown that the composition of the photoliquefied azobenzenes is approximately constant for moderate chain lengths and that the content of the (Z)-isomer decreases with increasing chain length. The azobenzenes with a chain length of C_9 and C_{11} stand out. These had not yet entered the liquid phase at the time of analysis after the irradiation time. This shows that the analyzed sample contained approx. 33% and 38% of the (Z)-isomer. When comparing the melting points of the azobenzenes with a chain length of C_9 and C_{11}, it became apparent that these have the highest melting points compared to the other chain lengths.

This gives rise to a further parameter which is decisive for the efficiency and applicability of a MOST-PCM azobenzene, which is the lowest ambient temperature which allows an efficient photoliquefication. Assuming that the photoliquefaction is independent of the mobility of the respective azobenzenes in the crystal structure, the lowest ambient temperature required to reach a liquid phase is dependent on the melting points of the (*E*)- and (*Z*)-isomers and the respective mole fraction. Therefore, as the melting point of the (*E*)-isomer increases, the requirement for a higher molar fraction or a lower melting point of the (*Z*)-isomer also increases.

For this purpose, the respective azobenzenes were irradiated with 365 nm at different ambient temperatures. It was found that the azobenzenes with a higher melting point of the (*E*)-isomer required a higher ambient temperature in order to be completely photoliquefied within a certain period of time. At a higher ambient temperature, the movement of molecules is improved, and the necessary mole fraction of (*Z*)-isomers is reduced. However, this also favors thermal back reaction, which might result in the required mole fraction not being achieved in order to liquefy the azobenzene.
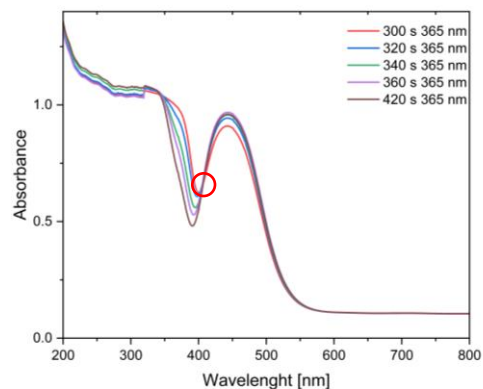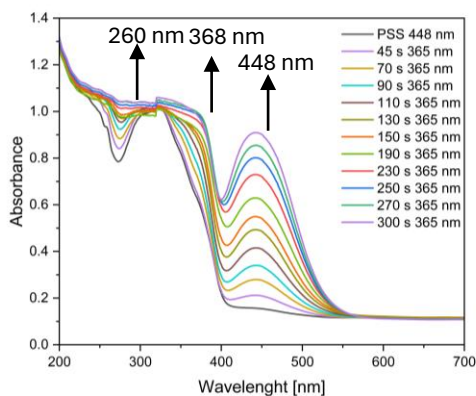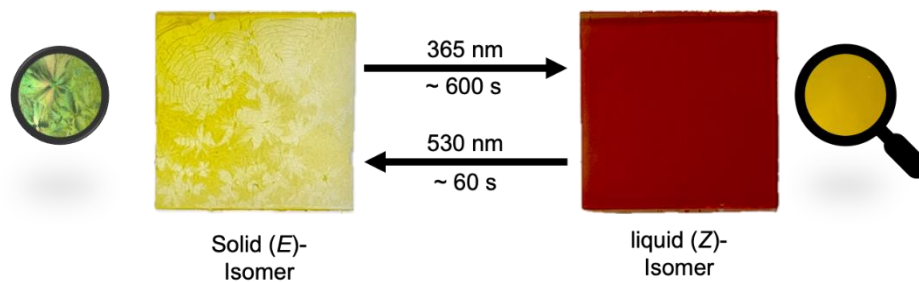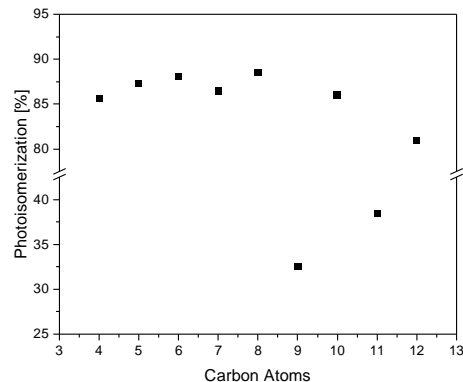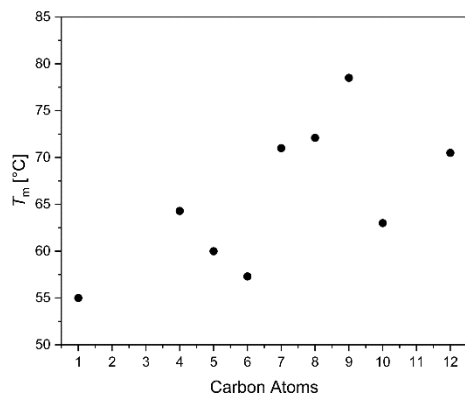
Kinetic investigation of the irradiation induced solid → liquid phase transition. Thus, for the quantification of the effectiveness of such a system not only thermodynamic properties, but also the kinetic aspect is important. As just shown, the charging process can be divided into two processes. The first process, which involves the phase transition from solid to liquid, should be the rate determining process. Therefore, time-resolved measurements were carried out with a powder XRD to measure the speed of photoliquefaction. In order to minimize the influence of the different penetration depths of X-rays and UV radiation, it is useful to measure a reflex with a small angle. The measurements were carried out at a constant temperature. It was observed that the intensity of the reflexes decreased with increasing irradiation time of the crystalline (*E*)-isomer, indicating an increasing degree of photoliquefaction.
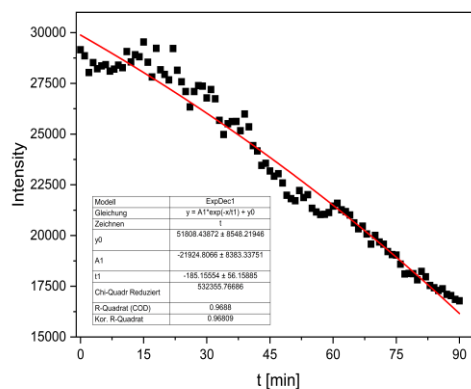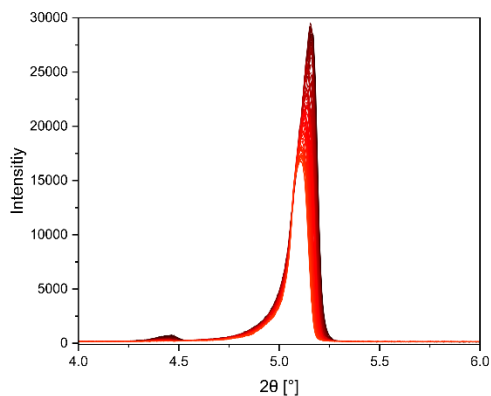
Kinetic investigation of the thermal half-life of the liquid → solid phase transition. Since the measurement of the kinetics for the thermal stability of the respective azobenzenes in solution is difficult to compare with the kinetics of the neat state, various methods were used to determine the half-life. The

investigation should consider how the chain length affects the half-life in the neat state and whether there are comparisons with the half-lives in solution.

In the investigation of the kinetics for MOST-PCM, not only the kinetics for the back isomerization of the liquid azobenzene is considered, but also crystallization processes from its mixed phase and thus poses a high challenge for a clear analysis of these processes.

Secondary effects such as autocatalysis must also be taken into account. When analyzing the thermal half-life for MOST-PCMs, again two different processes must be considered. The first process relates to the kinetics for the fully liquefied and charged azobenzene. At the beginning of the thermal back isomerization, there should only be a change in the ratio of the (*E*)- and (*Z*)-isomers in a completely liquid phase.

One aspect to be investigated for the first process is the influence of thermal energy released during back isomerization, which could accelerate thermal back isomerization. In conventional measurements of the thermal half-life, the respective azobenzenes are measured in high dilution, so that the thermal energy released by the back isomerization has only a marginal influence on the medium.

However, investigating the kinetics of the second process is much more complex, as other factors must also be taken into account. From a certain mole fraction, crystallization processes occur, which on the one hand release additional thermal energy, which accelerates the reverse reaction, and on the other hand this process can also be inhibited by the crystallization rate.
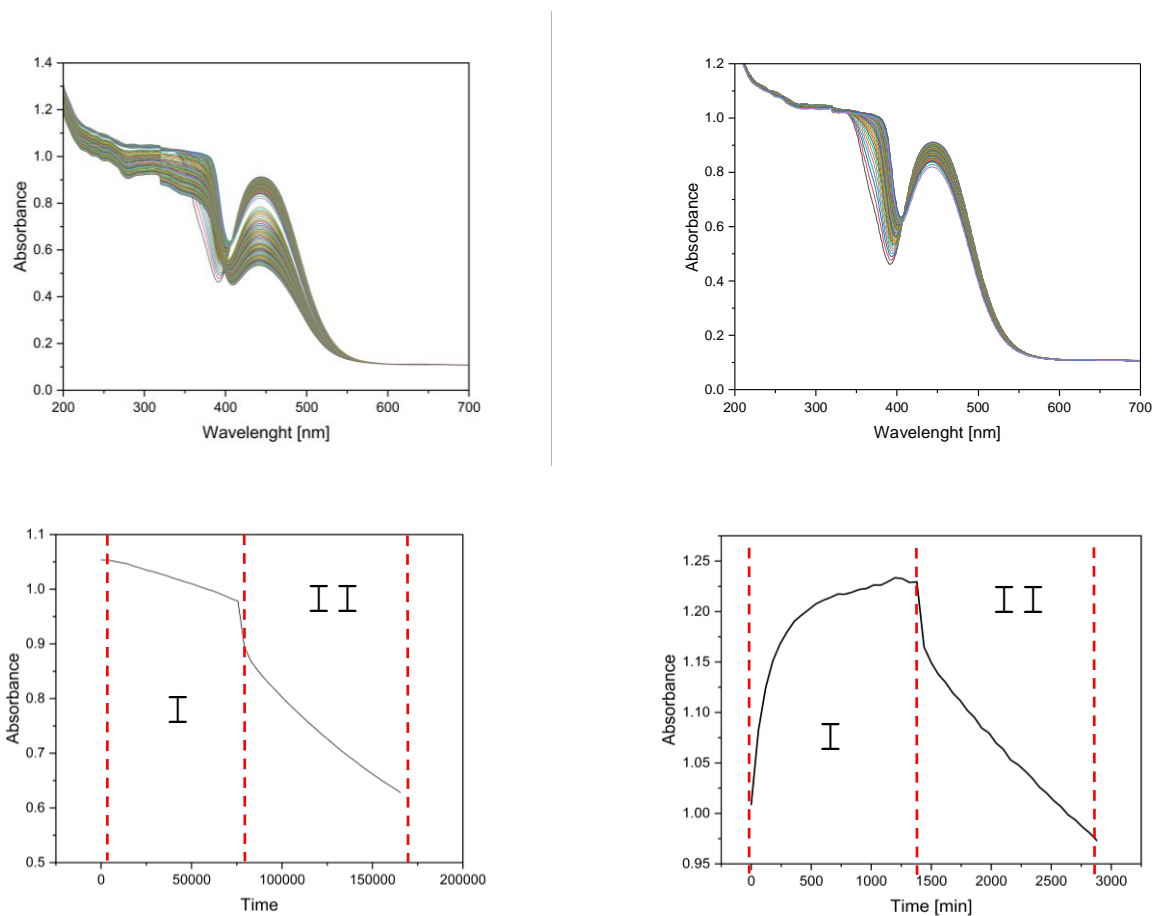
**Thermal and crystallization properties.** Differential Scanning Calorimetry (DSC) was utilised to investigate the thermal characteristics of *p*-Alkoxy-azobenzenes, providing insights into the temperature ranges and exothermic processes involved in the photoisomerizing phase-change phenomenon. Analysis revealed that the trans-Azo compounds display rapid crystallization and melting processes, with an increase in carbon chains resulting in a general increase in transition temperature (T_c) and melting temperature (T_m). While the corresponding cis-azo compounds exhibit a slow melting process, likely influenced by the variation in molecular structure once photoisomerized. The *n*-alkoxy chains within the trans-azo can rotate freely in the solid state while in the cis-azo compounds, they remain amorphous due to the weak van der Waals forces, leading to inefficient solid-state packing. This is evident by the sharp peaks present in the *trans*-azos and the broad peaks demonstrating the slower crystallization process in the *cis*-azos and by running the DSCs from -80°C these broad peaks can sometimes be observed, and a glass transition temperature (T_g) can be approximated for some of them. The DSCs confirm that these materials behave as phase-changing photoswitching systems as they have melting temperatures above room temperature (RT) as solids thus forming crystals while after being irradiated by light inducing the isomerization also form amorphous liquids due to the ambient heat due since they exhibit melting temperatures below RT.
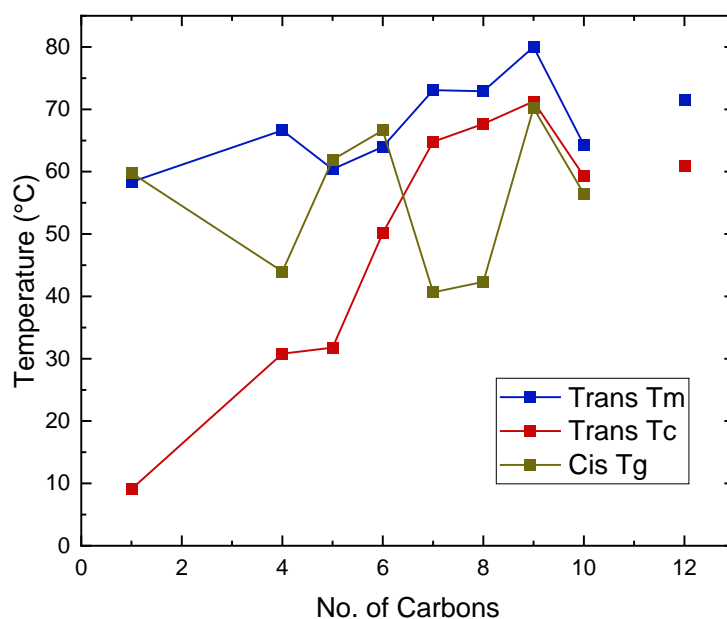
The compounds follow the general trend of the difference between the T_m and the T_c of the parent molecule decreasing as the carbon length chain increases. For the MOST-PCM purpose, the linear alkyl chain was varied to find a system where the parent molecule ideally has a T_c below room temperature for rapid crystallization once the photoisomer is back converted and a T_m that has a large difference between the melting temperature of the photoisomer in which the melting temperature is below RT. In this series, the material that fits this the best is the seven-carbon substituent as there is a large difference

between the T_m and T_g and the T_c is above RT. In some cases, the T_g of the photoisomer may surpass room temperature, yet due to the amorphous nature of these materials, these broad peaks usually initiate below room temperature. Additionally, if the sample is not maintained at -80°C for an extended period, crystallization may not occur. For the sample where crystallization does occur, it is essential to recognize that the energy of isomerization may also contribute to the melting of the frozen samples.

Energy density of *p*-Alkoxy-azobenzenes. The two exothermic peaks, the isomerization enthalpy ΔH_{Iso} and the crystallization enthalpy ΔH_{cryst} can be evaluated to determine the amount of energy ΔH_{Tot} that can be stored in a MOST-PCM material. The sharp exothermic peaks observed in the cooling curves of the trans-azos were attributed to the rapid crystallization, revealed ΔH_{cryst} values ranging from 22.06 to 49.31 kJmol^{-1}. The ΔH_{cryst} of these organic phase-change materials falls within the range of thermal energy typically harvested from the ambient environment. This implies that they effectively capture a significant amount of ambient heat while maintaining their capacity to store photon energy. The ΔH_{Iso} can be calculated by integrating the broad exothermic peaks which revealed ΔH_{Iso} of about 3.3 to 20.80 kJmol^{-1}. When irradiated or subjugated to thermal back conversion, the stored energy can be released which is a combination of the two pathways of thermal energy (ΔH_{Iso} and ΔH_{cryst}) thus, a larger density is released, 3.42 to 21.05 kJmol^{-1}. This data highlights the azobenzene with six carbons in the alkoxy chain to be the most suited for MOST-PCM applications has the highest energy storage density, achieving the target suggested for solar thermal storage systems.
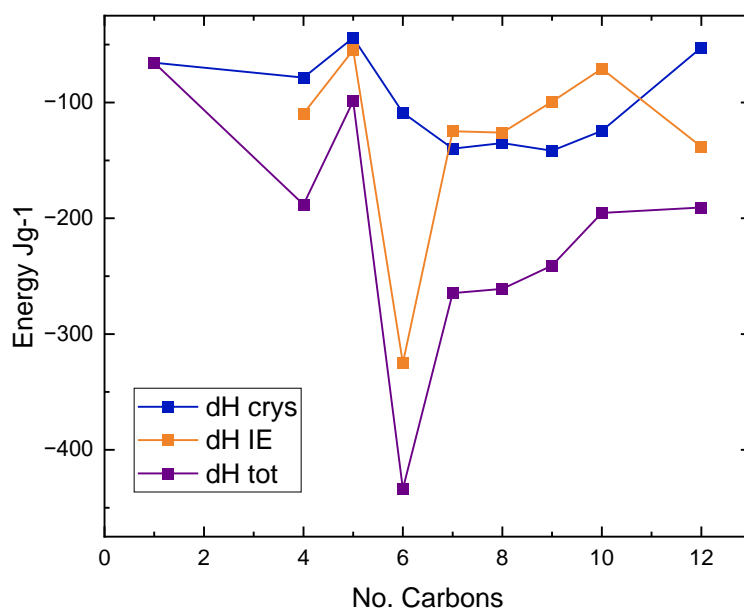
Supporting Information

Structure Properties Relationship of p-Alkoxy-Azobenzenes as Molecular Solar Thermal Phase Change Material for Energy Storage Systems

Conrad Averdunk,[a,b] Monika Shamsabadi,[c] Kasper Moth-Poulsen,[d] Hermann A. Wegner [a,b]

List of Contents

1. **General Information**

2. **Synthesis of Compounds**

3. **NMR Spectra**

4. **Compound characterization data**

5. **Irradiation Experiments**

6. **Kinetic Measurements**

7. **Determination of PSS composition by HPLC**

8. **DSC Data**

1. General Information

<u>Chemicals</u> were used as purchased from Sigma-Aldrich, Acros Organics, Alfa Aesar, TCIm Europe or BLD Pharm. Anhydrous solvents were purchased from Acros Organics. Technical grade solvents for workup and purification were distilled prior to use. Air and/or water-sensitive reactions were carried out under Schlenk-conditions or in a nitrogen-filled glovebox. Solids were dried under high vacuum (oil pump, ca 10-3 mbar) at room temperature (rt), 50°C or 60°C if necessary.

<u>Flash column chromatography</u> and column chromatography was carried out with Silica 60 M (0.04 – 0.063 mm) from Macherey Nagel GmbH & Co. KG. Thin layer chromatography was performed on Polygram® SIL G/UV254 from Macherey Nagel GmbH & Co. KG.

<u>NMR spectra</u> were measured on a Bruker Avance II 200 MHz, Avance II 400 MHz or Avance III 400 MHz HD spectrometer at rt, if not stated otherwise. Chemical shifts are reported in parts per million (ppm) relative to the solvent peak, coupling constants (J) are reported in Hertz (Hz). Deuterated solvents were obtained from Deutero GmbH (Kastellaun, Germany) or Euriso-Top GmbH.

<u>Melting points</u> were determined on a M5000 melting point meter from A.KRÜSS Optronic GmbH Germany. A heating rate of 1°C min-1, a resolution of 0.1°C and a measurement accuracy of $\pm$ 0.3°C (25–200°C) or $\pm$ 0,5°C (200–400°C) apply for this device.

For all azobenzenes, the thermodynamically more stable (*E*)-isomer is reported if not stated otherwise.

<u>ESI-MS</u> spectra were recorded on a Bruker Daltonics Micro TOF.

2. General Synthesis

Synthesis of 4-Hydroxy-Azobenzene

Aniline (30.0 mmol, 2.74 mL, 1.00 eq.) was added to an aqueous solution (60 mL) containing 15 ml of 37% $HCl_{(aq)}$. and to prepare an Aniline solution, which was added dropwisely into another aqueous solution (5mL) containing 12.8 mmol NaNO2 under ice water bath (0oC) with strong stirring for about 6 minutes. After mixing, the resulting solution was stirred for 40 minutes at 0°C to form a diazo salt solution. Then a separated aqueous phenol solution (20 mL) containing 10 mmol of phenol and 4 g of NaOH was prepared, and the diazo salt solution was added to the phenol solution slowly under ice water bath. The color of the solution would become dark during this process. After stirring at 0oC for 1 hour, the resulting solution was acidified by adding 20% HCl(aq) solution. Afterwards, the resulting solution was filtered by suction filtration to collect the dark solid which was washed by water, dissolved in acetone and reprecipitated by adding water slowly. Filtered the solution by suction filtration, and the brown powders were obtained as product with about 90% yield.

Synthesis of 4-Alkoxy-Azobenzenes

A mixture of 0.200 g of Bp-Azo-Ph (0.620 mmol), 50 cm^3 of acetone, and 0.857g (6.20 mmol) of K_2CO_3 were dissolved into 200mL three-necked flask with stirring. To this solution, acetone (50 cm^3) containing 1-bromohexane (1.023 g, 6.20 mmol) was slowly added (rate: about 3 seconds per one drop) and stirred for 9 h. The color of solution was changed to yellow. After cooling the solution to room temperature, K_2CO3 was filtered off, and the solvents were removed under vacuo to obtain yellowish crude product. The product was purified by column chromatography (silica gel/dichloromethane : n-hexane = 9 : 1). The product yield was 84.0% (yellow powder, 0.213 g).
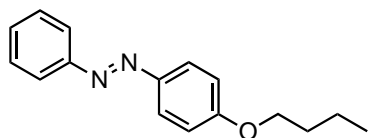
^{1}H NMR (400 MHz, CDCl3) δ 7.99 – 7.92 (m, 2H), 7.93 – 7.84 (m, 2H), 7.54 – 7.47 (m, 2H), 7.47 – 7.40 (m, 1H), 7.04 – 6.98 (m, 2H), 4.06 (t, J = 6.5 Hz, 2H), 1.87 – 1.76 (m, 2H), 1.59 – 1.46 (m, 2H), 1.00 (t, J = 7.4 Hz, 3H).
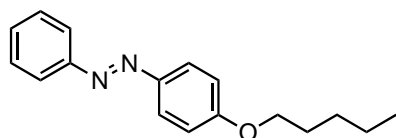
^{1}H NMR (400 MHz, CDCl3) δ 7.97 – 7.91 (m, 2H), 7.89 (dd, J = 7.4, 1.8 Hz, 2H), 7.50 (dd, J = 8.4, 6.6 Hz, 2H), 7.46 – 7.41 (m, 1H), 7.05 – 6.98 (m, 2H), 4.05 (t, J = 6.6 Hz, 2H), 1.89 – 1.78 (m, 2H), 1.52 – 1.36 (m, 4H), 0.95 (t, J = 7.0 Hz, 3H).
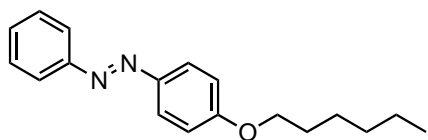
¹H NMR (400 MHz, CDCl3) δ 7.98 – 7.92 (m, 2H), 7.92 – 7.87 (m, 2H), 7.50 (dd, J = 8.4, 6.5 Hz, 2H), 7.47 – 7.40 (m, 1H), 7.07 – 6.97 (m, 2H), 4.05 (t, J = 6.6 Hz, 2H), 1.82 (dt, J = 14.7, 6.7 Hz, 2H), 1.49 (dtd, J = 14.9, 7.2, 4.5 Hz, 2H), 1.36 (h, J = 3.7 Hz, 4H), 0.98 – 0.88 (m, 3H).
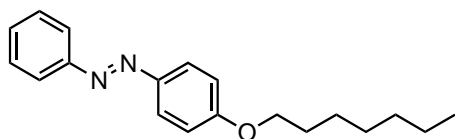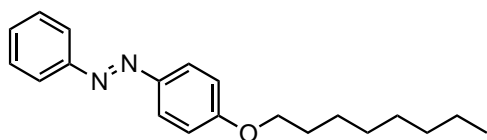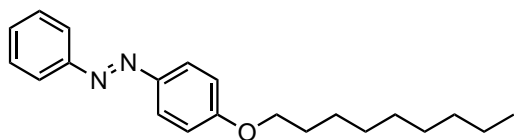

¹H NMR (400 MHz, CDCl3) δ 7.96 – 7.90 (m, 2H), 7.90 – 7.84 (m, 2H), 7.56 – 7.47 (m, 2H), 7.47 – 7.38 (m, 1H), 7.05 – 6.96 (m, 2H), 4.04 (t, J = 6.6 Hz, 2H), 1.88 – 1.75 (m, 2H), 1.54 – 1.43 (m, 2H), 1.43 – 1.27 (m, 6H), 0.96 – 0.87 (m, 3H).

¹H NMR (400 MHz, CDCl3) δ 7.99 – 7.91 (m, 2H), 7.91 – 7.85 (m, 2H), 7.56 – 7.47 (m, 2H), 7.46 – 7.41 (m, 1H), 7.04 – 6.97 (m, 2H), 4.04 (t, J = 6.6 Hz, 2H), 1.88 – 1.77 (m, 3H), 1.54 – 1.43 (m, 2H), 1.43 – 1.22 (m, 8H), 0.94 – 0.85 (m, 3H).

¹H NMR (400 MHz, CDCl3) δ 7.98 – 7.92 (m, 2H), 7.92 – 7.86 (m, 2H), 7.55 – 7.47 (m, 2H), 7.47 – 7.40 (m, 1H), 7.05 – 6.97 (m, 2H), 4.05 (t, J = 6.6 Hz, 2H), 1.82 (dt, J = 14.6, 6.7 Hz, 2H), 1.54 – 1.43 (m, 2H), 1.41 – 1.23 (m, 10H), 0.93 – 0.84 (m, 3H).

¹H NMR (400 MHz, CDCl3) δ 7.98 – 7.90 (m, 2H), 7.91 – 7.84 (m, 2H), 7.54 – 7.47 (m, 2H), 7.47 – 7.40 (m, 1H), 7.05 – 6.96 (m, 2H), 4.04 (t, J = 6.6 Hz, 2H), 1.82 (dt, J = 14.6, 6.7 Hz, 2H), 1.55 – 1.43 (m, 2H), 1.43 – 1.20 (m, 13H), 0.93 – 0.84 (m, 3H).

¹H NMR (400 MHz, CDCl3) δ 7.95 – 7.84 (m, 4H), 7.50 (dd, J = 8.2, 6.4 Hz, 2H), 7.47 – 7.39 (m, 1H), 7.00 (d, J = 8.5 Hz, 2H), 4.04 (t, J = 6.6 Hz, 2H), 1.92 – 1.76 (m, 2H), 1.54 – 1.42 (m, 2H), 1.42 – 1.22 (m, 15H), 0.93 – 0.85 (m, 3H).
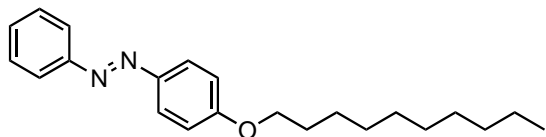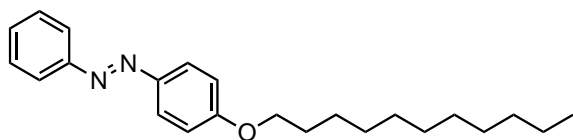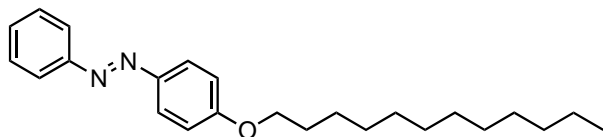

¹H NMR (400 MHz, CDCl3) δ 7.97 – 7.91 (m, 2H), 7.91 – 7.86 (m, 2H), 7.56 – 7.47 (m, 2H), 7.46 – 7.40 (m, 1H), 7.05 – 6.97 (m, 2H), 4.04 (t, J = 6.6 Hz, 2H), 1.82 (dt, J = 14.7, 6.7 Hz, 2H), 1.54 – 1.42 (m, 2H), 1.38 – 1.20 (m, 17H), 0.94 – 0.84 (m, 3H).

3. NMR-Spectra

Oct18-2022_CAV.330.fid
Averdunk CAV 150
254 g/mol / kA

H (m) 7.50
F (m) 7.94
E (m) 7.90
I (m) 7.01
G (m) 7.44
A (t) 4.06
C (m) 1.53
D (m) 1.81
B (t) 1.00

f1 (ppm)

Oct18-2022_CAV.290.fid
Averdunk CAV 149
268 g/mol / kA

D (m) 7.44
B (m) 7.93
A (dd) 7.89
E (m) 7.01
C (dd) 7.50
I (t) 4.05
H (m) 1.44
F (m) 1.83
G (t) 0.95

f1 (ppm)

Oct18-2022_CAV.300.fid
Averdunk CAV 147
282 g/mol / 3A

H (m) 7.94
G (m) 7.90
J (dd) 7.50
I (m) 7.45
F (m) 7.01
A (t) 4.05
C (dtd) 1.49
B (dt) 1.82
E (m) 0.93
D (h) 1.36

CAVNov07-2022.30.fid
Averdunk CAV-148_2
296.41 g/mol / 3A

11,13 (m) 7.92
1 (m) 7.44
10,14 (m) 7.88
3,5 (m) 7.01
2,6 (m) 7.50
16 (t) 4.04
18 (m) 1.48
17 (m) 1.82
22 (m) 0.91
19,20,21 (m) 1.35

CAVNov07-2022.480.fid
Averdunk CAV-152_2

E (m) 7.93
B (m) 7.50
D (m) 7.89
A (m) 7.01
C (m) 7.44
F (t) 4.04
H (m) 1.48
G (m) 1.82
J (m) 0.90
I (m) 1.32

f1 (ppm)

CAVNov07-2022.490.fid
Averdunk CAV-156

11,13 (m) 7.90
2,6 (m) 7.50
3,5 (m) 7.01
1 (m) 7.44
10,14 (m) 7.94
16 (t) 4.05
19,20,21,22,23 (m) 1.32
17 (dt) 1.82
24 (m) 0.89
18 (m) 1.47

f1 (ppm)

Nov15-2022_CAV.110.fid
Averdunk CAV-157
338.49 g/mol,

10,14 (m) 7.88
1 (m) 7.44
3,5 (m) 7.01
2,6 (m) 7.50
11,13 (m) 7.92
16 (t) 4.04
25 (m) 0.89
18 (m) 1.47
17 (dt) 1.82
19,20,21,22,23,24 (m) 1.30

Feb13-2023_CAV.60.fid
Averdunk CAV-183
352,52 g/mol,

10,11,13,14 (m) 7.89
1 (m) 7.44
3,5 (d) 7.00
2,6 (dd) 7.50
16 (t) 4.04
26 (m) 0.89
18 (m) 1.47
17 (m) 1.81
19,20,21,22,23,24,25 (m) 1.30

CAVNov07-2022.470.fid
Averdunk CAV-151_2
366,55 g/mol, k.A. mg

E (m) 7.45
C (m) 7.89
B (m) 7.93
A (m) 7.01
D (m) 7.50
16 (t) 4.04
J (m) 1.28
17 (dt) 1.82
27 (m) 0.88
18 (m) 1.47

Mar21-2023_CAV.130.fid
Averdunk CAV-194
408.63 g/mol, k.A. mg

B (m) 7.50
C (m) 7.01
E (m) 7.91
A (m) 7.44
D (m) 7.88
F (t) 4.04
H (s) 1.59
K (t) 0.88
G (m) 1.81
J (m) 1.27
I (td) 1.47

4. Compound characterization data

Melting Points

Compound	Tm,1	Tm,2	Tm,3	Tm,∅
p-OMe-AB	55.0	54.9	55.0	55.0
p-OBu-AB	64.4	64.3	64.3	64.3
p-OPen-AB	59.9	60.0	60.1	60.0
p-OHex-AB	57.3	57.3	57.2	57.3
p-OOct-AB	71.1	70.8	71.1	71.0
p-ONon-AB	78.4	78.6	78.4	78.5
p-ODec-AB	63.0	63.1	63.0	63.0
p-OUndec-AB	75.1	75.2	75.4	75.2
p-Dodec-AB	70.6	79.4	70.4	70.5

Table SX. T_m, T_c and T_g of **4-Hydroxy-Azobenzenes**

Azo	Trans T_m	Trans T_c	Cis T_g
		degrees Celcius	
4-Methoxy	58,34	9,08	59,79
4-Butoxy	66,63	30,8	43,98
4-Pentoxy	60,39	31,77	61,91
4-Hexoxy	63,99	50,14	66,63
4-Heptoxy	73,08	64,8	40,66
4-Octoxy	72,91	67,65	42,32
4-Nonoxy	80,00	71,27	70,19
4-Decoxy	64,3	59,27	56,46
4-Undecoxy	-	-	-
4-Dodecoxy	71,43	60,99	

5. Irradiation Experiments

Irradiation of the NMR or UV/Vis samples was conducted in an in-house built box using high power LEDs by Thorlabs. After the given irradiation times, the samples were immediately placed and measured in the corresponding spectrometer.

λ_{max} / nm	$\Delta\lambda$FWHM / nm	Luminous Flux / mW		Product name
265	11	3036		M265L5
300	20	2275		M300L4
325	12	3120		M325L5
365	9	3850		M365L3
385	11	3700		M385L3
405	12.5	3400		M405L4
530	35	3600		M530L4
660	20	3120		M660L4

Driver:
T-Cube™ LED Driver with Trigger Mode, 1200 mA Max


UV/Vis Spectroscopy

UV/Vis Spectroscopy were conducted with a SPECORD® 200 PLUS UV/Vis spectrophotometer equipped with two automatic eightfold cell changers and a Peltier thermostat system for temperature control manufactured by Analytik Jena. The spectrophotometer system was operated by the software ASpect UV from Analytik Jena.

In Solution

The samples were measured in QS High Precision Cells made of Quartz Suprasil® by Hellma Analytics with a light path of 10 mm. The sample volume was 3 mL and the sample concentration 6 x 10-5 M. Irradiation at 340 nm was conducted with a 3UV-38 handheld lamp (8 W) by UVP.


Neat

The samples were measured in between two rectangular window made of Quartz Glass High Performance with a cell holder for cell type 106 by Hellma. The samples were thermically melted between two rectangular window and placed in the cell holder.
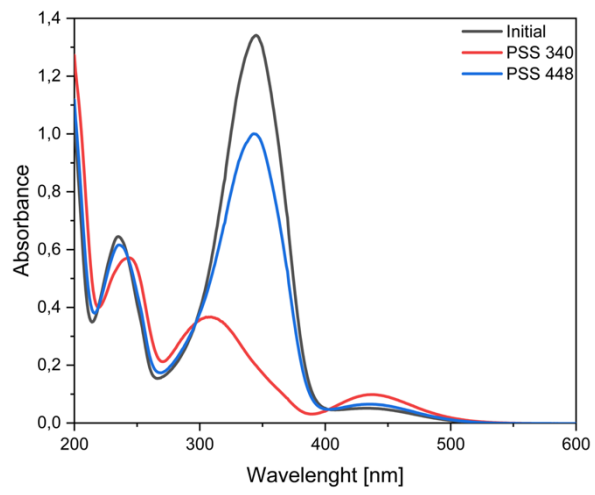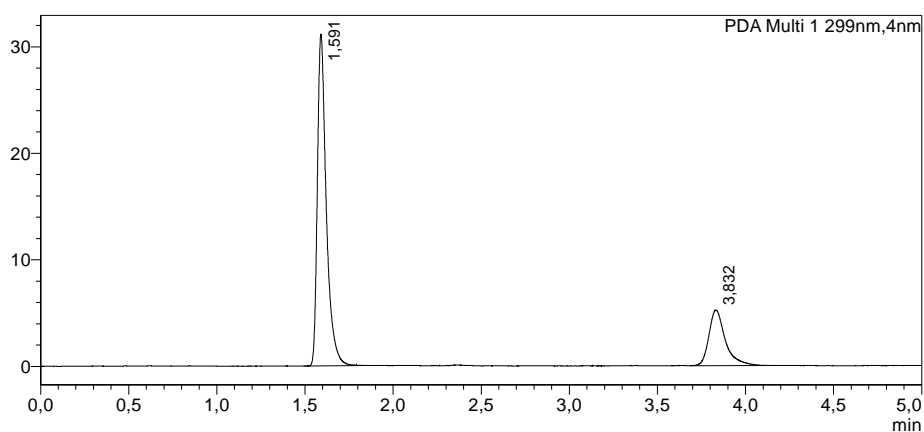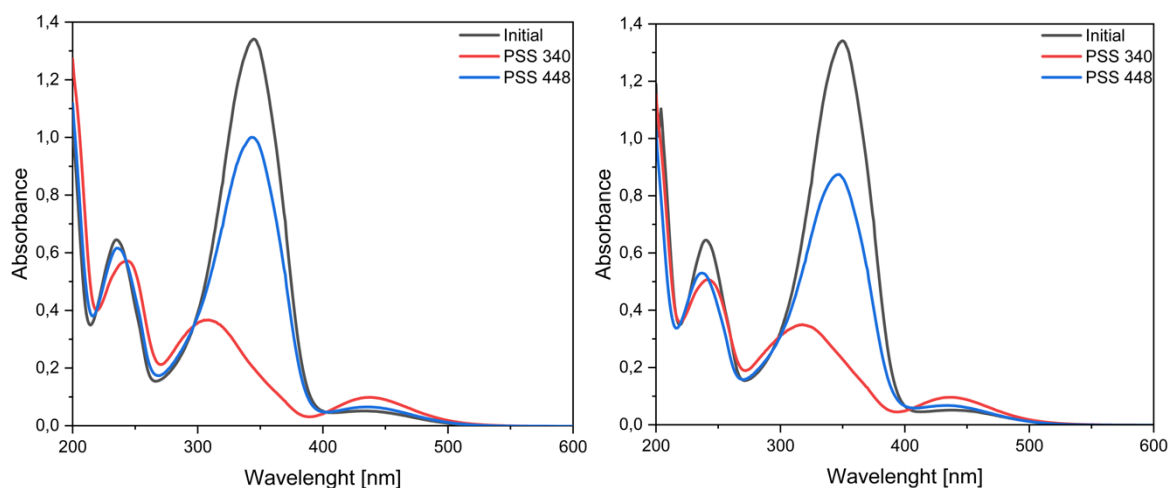
6. Kinetic Measurements

All samples were irradiated at the corresponding wavelengths for 5 min prior to the kinetic measurements. Spectra were recorded from 200 – 600 nm with a scan speed of 20 nm/s. The thermal isomerization was monitored in 15 min intervals (10°C and 15°C) for 24 h and in 10 min intervals (20°C and 25°C) for 18 h. All compounds were measured three-fold at each temperature at concentrations of $5 \cdot 10^{-5}$ mol/L (4g: $7 \cdot 10^{-5}$ mol/L) in acetonitrile. For data analysis, Origin Pro 2016G by Origin Lab Corporation was used. The absorbances A at the maximum wavelengths were plotted against the time t elapsed after the start of the measurements. Rate constants k and half-lives t1/2 were determined after fitting the data with an Exponential Decay Function (ExpDec1, Origin) according to the literature.
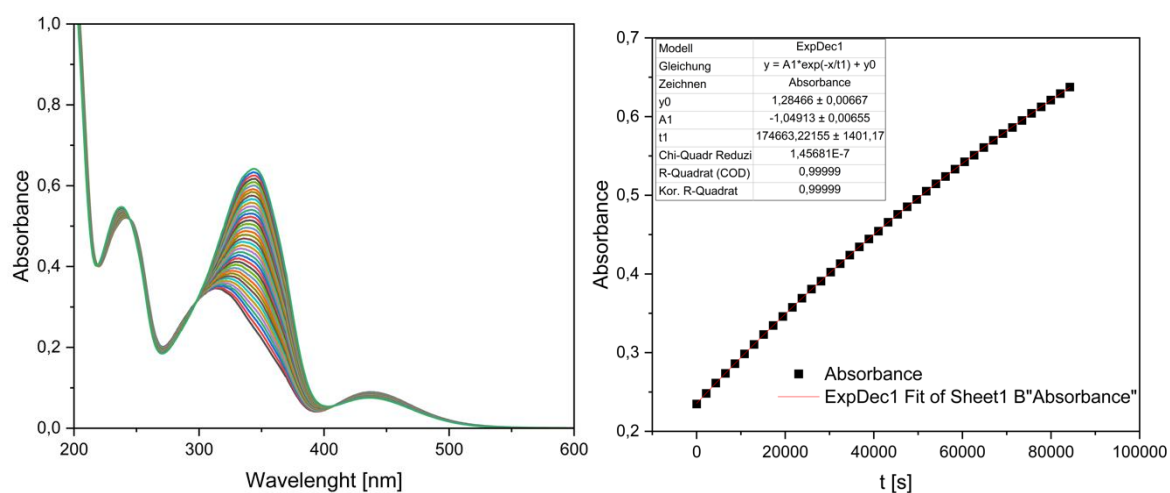
7. Determination of PSS composition by HPLC

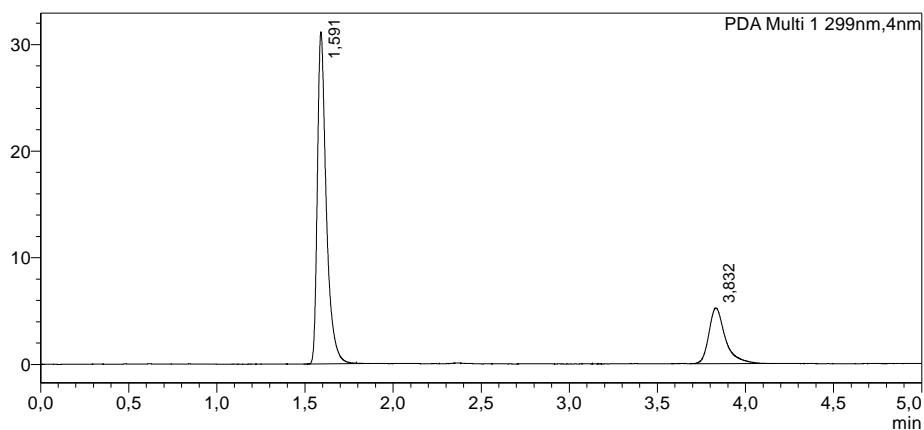**Determination of PSS composition in solution by HPLC**

The PSS isomer concentrations were determined with a Shimadzu LCMS-2020 system using a 150 x 4 mm Eurospher 100-5 C18 column with acetonitrile/water (90:10) as isocratic eluent (1.5 mL/min). Detection was carried out using a Shimadzu SPD-M20A diode array detector at the previously determined isosbestic wavelengths (see Figure S2, Figure S3). The change from pure acetonitrile to acetonitrile/water (90:10) in the separation had only negligible effect on the isosbestic wavelengths, as show in Figure S7. Irradiation of the samples was carried out in 2 mL glass vials for 3 min (1 min at 305 nm) at the corresponding wavelength in 100% acetonitrile, from which aliquots of 10 μL ($5 \cdot 10^{-4}$ mol/L) or 50 μL ($5 \cdot 10^{-5}$ mol/L) were injected for analysis. For all determined isomer ratios, an error of ±1% is assumed.


Peak Table

PDA Ch1 299nm

Peak#	Ret. Time	Area	Height	Conc.
1	1,591	109622	30596	76,364
2	3,832	33931	5211	23,636
Total		143553	35807	

Peak Table

Peak#	Ret. Time	Area	Height	Conc.
1	1,591	109622	30596	76,364
2	3,832	33931	5211	23,636
Total		143553	35807	

	PSS 340 nm		PSS 448 nm	
	(*E*) - Isomer	(*Z*) – Isomer	(*E*) – Isomer	(*Z*) – Isomer
4	23.1	76.9	79.6	20.4
5	22.9	77.1	79.7	20.3
6	23.1	76.9	79.7	20.3
7	25.5	74.5	80.2	19.8
8	25.3	74.7	80.5	19.5
9	26.4	73.6	80.9	19.1
10	27.3	72.7	80.1	19.9
11	26.7	73.3	81.8	18.2
12	23.1	76.9	79.6	20.4
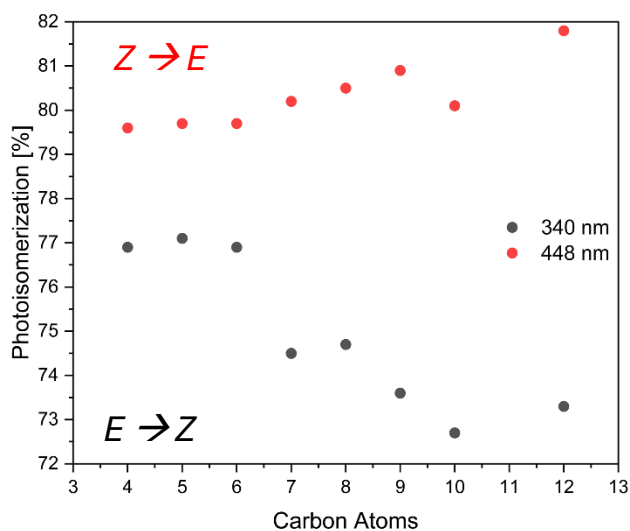
Determination of PSS composition of neat sample by ^{1}H-NMR Analysis

	PSS 365 nm	
	(*E*) - Isomer	(*Z*) – Isomer
4	14.4	85.6
5	12.7	87.3
6	11.9	88.1
7	13.5	86.5
8	11.5	88.5
9	67.5	32.5
10	14.0	86.0
11	61.6	38.4
12	19.0	81.0

8. DSC Data